Doctoral Dissertation

博士論文

Hydrogen in the core

（地球中心核の水素）

A Dissertation Submitted for the Degree of Doctor of Philosophy
December　2019

令和元年１２月 博士（理学）申請

Department of Earth and Planetary Science, Graduate School of Science,
The University of Tokyo

東京大学大学院 理学系研究科 地球惑星科学専攻

Shoh Tagawa

田川 翔

Abstract

Birch (1952) pointed out that the Earth's core is lighter than pure iron. The density difference between the pure iron at the Earth's core conditions and the Earth's observations is around 5–10% at the outer core and 3–5% at the inner core. It suggests that a certain amount of light elements should be contained in the Earth's core. However, even though the significant effort has been spent to decide the kinds and amounts of the light elements, it is still an open question. From the high-pressure mineral physics and cosmochemical/geochemical studies, H, C, O, Si, and S have been proposed for the candidates (e.g., Hirose et al., 2013; Li & Fei, 2014). If hydrogen is the sole light element in the core, its amount is up to ~1 wt.%, corresponding to ~120 times hydrogen that exists in oceans.

Hydrogen receives heightened attention, but the Fe-H alloy is the least investigated of the other alloys due to its experimental challenges, especially in synthesizing starting material, determining the hydrogen contents in a sample, and using high-pressure apparatuses. It is mainly because hydrogen escapes from iron in ambient conditions. Also, hydrogen quickly intrudes into diamond anvils during heating and then shatters them. I overcame the difficulties by improving experimental procedures and then performed the present study, in order to ascertain whether or not hydrogen is a major light element in the core. This work consists of the following three viewpoints: partitioning experiment of hydrogen between liquid metal and liquid silicate under the core formation conditions (Chapter 2); phase relations of the Fe-FeH system (Chapter 3); and the compressibility of *hcp* Fe-H-Si alloys (Chapter 4).

In Chapter 2, I examined the partitioning experiments of hydrogen between molten iron and silicate melt under the Earth's core formation conditions. High-pressure and -temperature experiments using a laser-heated diamond anvil cell (LH-DAC) was performed at 30–60 gigapascals (GPa) and 3100–4600 kelvin (K), corresponding to the conditions of single-core formation models. *In situ* X-ray diffraction (XRD) measurement and secondary ion mass spectrometry (SIMS) analysis demonstrate the high siderophile (iron-loving) nature of hydrogen even under such high pressures and temperatures. If core-forming metals were in equilibrium with the magma ocean, containing about 700 ppm H_2O before degassing water that later formed oceans, the core might include 2900–5300 ppm H; this explains ~30–50% of the density deficit and the velocity excess of the outer core relative to pure iron. It also suggests that 25–66 times the ocean's mass of water was delivered to the Earth by the time of core formation.

In Chapter 3, I will report the phase relations of the Fe-FeH binary system up to 173 GPa and 4020 K using an LH-DAC. Despite its importance, the phase diagram of Fe-FeH over at 20 GPa is still an open question. The concentration of hydrogen in the Fe-FeH binary was typically denoted as a molar ratio of H/Fe, which is the definition of "*x*." I combined three cell assemblies:

a sub-stoichiometric (x<1) experiment, a stoichiometric experiment (x=1), and an experiment in which hydrogen diffused in a Fe-H sample. I performed high-pressure and -temperature experiments for 11 runs. Then, I determined the melting temperatures of stoichiometric FeH and sub-stoichiometric FeHx, and the stability field of each crystal structure. The Fe-FeH system had a eutectic-type phase diagram, and the eutectic temperature would be sufficiently low to explain the low core-mantle boundary temperature inferred from the solidus temperature of pyrolite, although end-member *fcc* FeH had a high melting temperature. The miscibility gap of hydrogen contents between the subsolidus phases exists at $0.44 < x < 0.69$ in my dataset, and it implies that *hcp* FeHx is feasible as the inner core crystal structure if hydrogen is the dominant light element. Features of the phase diagram of the Fe-FeH system does not rule out the hydrogen bearing Earth's core up to $x \sim 0.6$ (1.07 wt.% H), the middle of the miscibility gap.

In Chapter 4, I examined the compression behavior of hexagonal-close-packed (*hcp*) $(Fe_{0.88}Si_{0.12})_1H_{0.71}$ and $(Fe_{0.88}Si_{0.12})_1H_{0.97}$ (in the atomic ratio) alloys up to 130 GPa in a diamond-anvil cell (DAC). While contradicting experimental results were previously reported on the compression curve of *double-hcp* (*dhcp*) FeH$x\approx1$, this study showed that the compressibility of *hcp* $Fe_{0.88}Si_{0.12}Hx$ alloys is very similar to those of *hcp* Fe and $Fe_{0.88}Si_{0.12}$, indicating that the incorporation of hydrogen into iron does not change its compression behavior remarkably. This data is also applicable to estimate the compressibility of *hcp* FeHx, which is one of the candidates of the inner core material. The present experiments suggest that the inner core may contain up to 0.66 wt.% hydrogen ($FeH_{0.37}$) if temperature at the inner core boundary (ICB) is 5000 K. The calculated density profile of $Fe_{0.88}Si_{0.12}H_{0.26}$ alloy containing 0.50 wt.% hydrogen in addition to geochemically-required 6.5 wt.% silicon matches the seismological observations of the outer core, supporting that hydrogen is an important core light element.

In the final chapter, I discuss the possible amount of hydrogen in the Earth's core. According to studies on other light element systems and this work, the core is likely to contain around 0.4 wt.% H, which explains ~40% of the outer core's density deficit. It is also consistent with geochemically-constrained core formation models. The hydrogen amount is comparable to 50 times the amount of seawater, and some recent planetary formation theories show that this is plausible. Although further investigation is needed, I concluded that hydrogen is the feasible light element in the Earth's core.

Acknowledgments

I am deeply grateful to my advisor, Prof. K. Hirose, for his wonderous guidance and wisdom. His comments and suggestions were valuable throughout my study. Every time I had a discussion with him, I learned the fundamental concepts of deep Earth science, ways to build logic, and having the right attitude towards science. I am so fortunate that I had the opportunity to be involved in his laboratory during my master's and doctoral courses. It was a challenging experience at times, but fun all the same. I also thank Assoc. Prof. Kenji Ohta, who developed pioneering work for high-pressure studies dealing with hydrogen in a DAC. I learned about important procedures for FeH experiments from him. When he started the research on hot-dense hydrogen, the experiment was state of the art. So, it is easy to imagine the many challenging tasks in building the experimental method. I thus respect him for his efforts. I discussed my work with him many times, and I found a way to overcome the technical difficulties in my experiments.

I am also grateful to Prof. H. Yurimoto, and Asst. Prof. N. Sakamoto for their support for the development of a SIMS analysis on a DAC sample. The collaboration with them would be brought to a break-thorough for "high-pressure geochemistry." I also would like to thank Dr. S. Tateno for teaching me the high-pressure experimental procedures and chemical analysis. I am thankful to Dr. Y. Ohishi, Dr. N. Hirao, and Dr. S. Kawaguchi for helping me perform experiments at SPring-8. I appreciate the lecture for an EPMA analysis by Dr. H. Yoshida, Dr. K. Ichimura, and Ms. K. Yonemits. I thank Dr. Y. Kuwayama, Dr. H. Gomi, Mr. K. Ozawa, Mr. Y. Yokoo, Dr. C. Kato, Mr. T. Wakamatsu, Mr. K. Oka, and Dr. H. Kurokawa, whose comments contributed to my work. Dr. Y. Nakajima profoundly contributed to the Appendix. Dr. K. Umemoto provided his calculation result to evaluate ρ and V_P of the outer core composition that I proposed. Ms. I. Bonati, Mr. K. Hikosaka, Mr. Y. Okuda, Ms. L. Kwok, and *Grammerly Inc.* supported proofreading. My gratitude also extends to Assoc. Prof. B. Militzer, who discussed a lot about the nature of iron hydride at high pressure and temperature when I stayed in his laboratory several times.

I wish to thank all members of Hirose-lab., Ohta-lab. (Tokyo Tech), and ELSI staff and students. The discussion with them is delightful. I would like to thank Grant-in-Aid for JSPS fellow (DC1). This study was also supported by the Grant-in-Aid for specially promoted research (PI: Prof. K. Hirose) and funding for the contributors.

I would like to gratefully acknowledge Prof. H. Kagi, Prof. H. Iwamori, Assoc. Prof. K. Kawai and Assoc. Prof. T. Iizuka for reviewing my Ph. D. dissertation. Their comments and suggestions further improved the manuscript.

Finally, I would like to thank my family for being so supportive and encouraging me. I can never thank you enough.

Contents

Abstract i
Acknowledgments iii
Contents iv
Figure and Table captions vi

Chapter 1. General introduction 1
1.1 Hydrogen, as a light element candidate in the core 2
1.2 Review of high-pressure studies on hydrogen in the core 5
(1) Comparison of density, V_P, V_S, and their pressure dependences with a reference model 5
(2) Determination of phase diagrams of Fe-X alloys in high pressures 8
(3) Metal-silicate partitioning experiments of light elements 9
(4) Mutual interactions between light elements 12
1.3 Research objective 12
Figures and tables 13

Chapter 2. Partitioning of hydrogen between Earth's core and mantle 20
Abstract 20
2.1 Introduction 21
2.2 Methods 23
(1) Starting materials 23
(2) High-pressure and -temperature experiments and *in situ* XRD measurement 23
(3) SIMS analysis for the hydrogen content in silicate melt 25
(4) Chemical analysis with EPMA 27
2.3 Results 28
(1) General appearance, SEM-EDS mapping, EPMA analysis 28
(2) The hydrogen contents in metal 28
(3) The hydrogen contents in silicate 30
(4) Partitioning coefficient of hydrogen 30
2.4 Discussion 31
(1) Parameterizing hydrogen metal–silicate partitioning 31
(2) Hydrogen content in the Earth's core 33
Figures and tables 35

Chapter 3. Phase relations of FeH*x* at high pressures 50
Abstract 50
3.1 Introduction 51

3.2 Experimental Method 55
3.3 Results 60
(1) Design of experiments 60
(2) Construction of the method to calculate the hydrogen content (Experiment A) 61
(3) The miscibility gap of Fe-FeH binary system (Experiments B and C) 63
(4) The stability field of *dhcp* FeH*x* (Experiment E) 65
(5) Melting experiment for stoichiometric FeH*x* (Experiment F) 65
(6) Melting experiment for stoichiometric FeH*x* (Experiment F) 66
3.4 Discussion: The phase diagram of the Fe-FeH binary system 67
3.5 Conclusion 69
Figures and tables 70

Chapter 4. Compression of *hcp* Fe–Si–H alloys 91
Abstract 91
4.1 Introduction 92
4.2 Experimental Method 93
4.3 Results 95
(1) Hydrogenation and crystal structure of Fe–Si–H 95
(2) The hydrogen concentration in *hcp* Fe–Si–H 96
(3) Compression behavior 97
4.4 Discussion: Fe–Si–H alloy in the core? 98
Figures and tables 101

Chapter 5. General discussion 109
5.1 Consistency with core formation models 109
5.2 Composition model of the Earth's core 114
5.3 Future perspectives 117
(1) Can hydrogen explain the lower V_S and anisotropy of V_P in the inner core? 117
(2) Direct observation of hydrogen in FeH alloys 117
(3) Timing and origin of the water 118
(4) Low D/H ratio of the deep mantle 119
(5) Direct observation of hydrogen in the core -Neutrino oscillations- 120
Figures 121

Concluding Remarks 126
References 127
Appendix. Nuclear resonant X-ray scattering of Fe-Si-H at high pressures 142

Figure and Table captions

Figure 1.1 Comparison of density between pure iron and PREM in the core pressure range..... 13
Figure 1.2 Comparison of the compression behavior of FeH reported in previous studies 14
Figure 1.3 Comparison of one-dimensional reference models of the interior of the Earth..... 15
Figure 1.4 Expected phase diagram of the Fe-H system at ~135 GPa proposed by Fukai (1992) 16
Figure 1.5 Example of core partitioning equilibration conditions for a scenario from Badro et al. (2015) and Rubie et al. (2015) 17

Figure 2.1 Sample configuration..... 35
Figure 2.2 Calibration curve for the SIMS analysis of $^{1}H/^{28}Si$ based on standard glasses..... 36
Figure 2.3 Sample cross-section for run #1..... 37
Figure 2.4 Analyses of hydrogen in metal..... 38
Figure 2.5 Hydrogen content in metal..... 39
Figure 2.6 Analyses of hydrogen in silicate 40
Figure 2.7 Hydrogen content in quenched silicate melt..... 41
Figure 2.8 Parameterizing hydrogen metal–silicate partitioning coefficient 42
Figure 2.9 K_D^O with and without considering the presence of hydrogen for activity estimates ... 43
Figure 2.10 Metal-silicate partitioning coefficient of hydrogen 44
Figure 2.11 Partition coefficient D of hydrogen (molar basis) as a function of oxygen fugacity relative to the IW buffer..... 45
Figure 2.12 Estimate of hydrogen concentration in the core..... 46
Figure 2.13 D_H values on the core formation conditions 47

Figure 3.1 Crystal structure of FeHx ($x \leq 1$) 70
Figure 3.2 Schematic of sample configurations and photographs of the samples..... 71
Figure 3.3 Design of this experiment. 72
Figure 3.4 Compression behavior of *dhcp* and *fcc* FeH 73
Figure 3.5 Pressure dependence of ΔV_H 74
Figure 3.6 Hydrogen contents of FeHx 75
Figure 3.7 A room–temperature experiment in which hydrogen diffused in a sample..... 76
Figure 3.8 A sequence of X-ray diffraction patterns during melting experiments in run U1 78
Figure 3.9 Sequence of X-ray diffraction patterns during compression in run U1 79
Figure 3.10 A sequence of X-ray diffraction patterns during melting experiments in run S1..... 80
Figure 3.11 A sequence of X-ray diffraction patterns during melting experiments in run M1 ... 81
Figure 3.12 FIB scanning ion microscope (SIM) image from run U1 82

Figure 3.13 SIM image and its temperature distribution from run U4 83
Figure 3.14 Melting temperature of FeH*x* 84
Figure 3.15 Phase diagram of the Fe-FeH binary system 85

Figure 4.1 Integrated XRD patterns collected at room temperature during run # 1 101
Figure 4.2 Two-dimensional XRD pattern of *hcp* $Fe_{0.88}Si_{0.12}H_{0.71}$ at 130 GPa. 102
Figure 4.3 Changes in lattice parameters of *hcp* $Fe_{0.88}Si_{0.12}H_{0.71}$ observed in run #1 103
Figure 4.4 Compression curves of *hcp* $Fe_{0.88}Si_{0.12}H$*x* 104
Figure 4.5 Comparison of the density of $Fe_{0.88}Si_{0.12}H_{0.26}$ alloy along the isentropic temperature profile (T_{ICB} = 5000 K) with the PREM density 105
Figure 4.6 Comparison of the density of Fe–Si–H alloys along isentropic temperature profile (T_{ICB} = 5500 K) with the PREM density. 106
Figure 4.7 Comparison of the density of Fe–Si–H alloys isentropic temperature profile (T_{ICB} = 6000 K) with the PREM density. 106

Figure 5.1 Schematic diagram of the continuous core formation scenario 121
Figure 5.2 Evolution of hydrogen and water contents in the core and silicate mantle 122
Figure 5.3 Possible outer core composition in Fe-H-X ternary systems 123
Figure 5.4 ρ and V_P of hydrogen bearing the Earth's core composition models 124
Figure 5. 5 Estimation of the contribution of hydrogen from nebula gasses 125

Table 1.1 Geochemical and cosmochemical reasons which support each light element candidate in the core 18
Table 1.2 Proposed light element contents (wt.%) in the core 19

Table 2.1 Summary of the metal-silicate partitioning experiments 48
Table 2.2 Chemical compositions (wt.%) of stating material and silicate melt 49
Table 2.3 Chemical compositions (wt.%) of quenched liquid metals 49

Table 3.1 Summary of experimental conditions 86
Table 3.2 Experimental results of compression of stoichiometric *dhcp* and *fcc* FeH 87
Table 3.3 Experimental result of FeH*x* phase relations 88
Table 3.4 Experimental results for melting experiments 90

Table 4.1 Experimental results of compression of *hcp* Fe–Si–H alloys 107
Table 4.2 EoS parameters for $Fe_{0.88}Si_{0.12}H$*x* and related alloys 108

Chapter 1. General introduction

Hydrogen is one of the likely candidates of light elements in the core. Since the seminal work by Birch (1952) pointed out the density deficit of the Earth's core (Figure 1.1), numerous papers have tried to figure out their kinds and amounts, but it is still an open question. The density deficit, which is the density difference between pure iron and the Earth's observation, is around 5–10% (in weight) in the outer core (depth, 5150 to 2891 km; pressure,136–329 GPa) and 3–5% in the inner core (depth, 5150 to 6371 km; pressure, 329–364 GPa) (Anderson and Isaak, 2002; Dewaele et al., 2006; Dorogokupets et al., 2017; Ichikawa et al., 2014), although the density deficit is a trade-off with temperature uncertainties. H, C, O, Si, and S have been proposed from high-pressure mineral physics and cosmochemical/geochemical studies (e.g., Hirose et al., 2013; Li & Fei, 2014). Hydrogen has recently gained more attention, but Fe-H alloy has been studied the least among possible core alloys (see Figure 1 in Hirose et al., 2013) due to the experimental difficulties. Because of the scarcity of experimental data, hydrogen is the least understood light element. This thesis was performed in order to ascertain whether or not hydrogen is a major light element in the core from three viewpoints: partitioning experiment of hydrogen between liquid metal and liquid silicate under the core formation conditions (Chapter 2); phase relations of Fe-H system (Chapter 3); and compressibility of *hcp* Fe-H-Si system (Chapter 4).

1.1 Hydrogen, as a light element candidate in the core

The kinds of light elements in the core remain controversial. In the past ~65 years, physical and thermodynamic properties of iron and its alloys with H, C, O, Si, and S were examined by high pressure and high-temperature experiments (*e.g.* Hirose et al., 2013; Poirier, 1994). Each candidate is supported by specific geochemical/cosmochemical reasons (Table 1.1). Recently, hydrogen has gained more attention, mainly because planet formation theory suggests that a large amount of water may have been brought to the Earth during its formation.

The amount of water contained in the Earth's building blocks could be huge. For example, due to the gravitational scattering of H_2O-bearing planetesimals by gas-giant planets (Raymond et al., 2007), planets with similar size and orbit of Earth would contain 20–60 ocean masses of water. More sophisticated models such as scattering by gas-giant planets with higher eccentric orbitals (Raymond et al., 2009) or the "Grand Tack" scenario (O'Brien et al., 2014; Walsh et al., 2011) also concluded that ~5 to 15 ocean masses of water were likely delivered to Earth (reviewed by Jacobson and Walsh, 2015), assuming that outer solar planetesimals contain 5 and 10 wt.% water. However, these parameters were set in order to match the "reasonable" water concentration of the present Earth (e.g., ~2.5 ocean masses in O'Brien et al., 2014). The maximum contents of the water in C-type asteroids could be higher during the early stages of accretion (*e.g.* Alexander, 2019; Marrocchi et al., 2018). Moreover, the snow line could be migrated to an inward

protoplanetary disk (Oka et al., 2011) and another mechanism such as “pebble accretion” could bring ice from outer disk regions (Sato et al., 2016). Therefore, it would be unrealistic to build an Earth analogue with low water concentrations and challenging to constrain the bulk water contents of Earth from planetary formation theories.

Other mechanisms to bring water to the proto-Earth are also provided. First, hydrogen ingassing from the nebular atmosphere would dissolve into the magma ocean (Ikoma and Genda, 2006). This model was integrated with the dynamics model in the magma ocean, and it was concluded that a large amount of water in the Earth’s interior could be formed in this way (from 0.9% to more present ocean masses, which depend on the scenario). One possible scenario shows that ingassing from the nebula continued until the proto-Earth became >60% mass of the present Earth, and 15 ocean masses of water were accreted (Olson and Sharp, 2019). The isotope ratio of noble gases degassing from the mantle (*e.g.* Williams and Mukhopadhyay, 2019) also supported the ingassing from nebular gas. Water adsorption on silicate grains in the protosolar nebula could be another mechanism that could supply up to several ocean masses (Muralidharan et al., 2008). Although the contribution of these mechanisms are likely assumed to be minor because they lower the Earth’s deuterium/hydrogen ratios (D/H) (Wu et al., 2018), hydrogen contents in the core could change this consequence. Note that the water mass brought after the core formation is still under debate (*e.g.* Fischer-Gödde and Kleine, 2017; Schiller et al., 2018).

So, where did the rest of the water brought to Earth during its main stages of the growth go? Abe et al. (2000) reviewed the water distribution in early Earth. If Earth was formed with volatile-bearing materials or in-gassing from the proto nebula, then proto-Earth would have a steam atmosphere, which would contain ~ 1 ocean mass of water vapor (P_{water} ~ 10^7 Pa). Because the steam in such a high-pressure atmosphere dissolved into the molten silicate well, the concentration of water in the magma ocean could reach ~1 wt.%. The water would react with iron during core segregation and then form iron hydride. So, the core is a potential "hidden water reservoir" (Fukai and Suzuki, 1986; Okuchi, 1997; Stevenson, 1977). However, because of the lack of experimental constraints, the amount of hydrogen in the core is still an open question.

The hydrogen content in the core is key for understanding the building blocks of Earth and its volatile content. The maximum amount of hydrogen in the core to explain the density deficit is estimated to be 0.8–1.3 wt.% if hydrogen was the sole light element in the core (Thompson et al., 2018), which is equivalent to the amount of hydrogen included in 100–160 times the amount of seawater. The geochemical constraint of the ocean amount on Earth is debated because the D/H ratio of the Earth was changed by mass fractionation during atmospheric hydrogen loss (Genda and Ikoma, 2008) and in the core formation reaction. Therefore, experimental petrology is necessary for a comprehensive understanding of water and hydrogen amounts in the composition of Earth.

1.2 Review of high-pressure studies on hydrogen in the core

The following four viewpoints are the commonly adapted ways to determine the light elements in the core in high-pressure studies. In this section, I will review the recent experimental results related to the study for all light element candidates and show the understanding of the hydrogen bearing systems so far.

(1) Comparison of density, V_P, V_S, and their pressure dependences with a reference model

This is the most classic method of constraining the kind and amount of light elements. The seismological study determines the density (ρ), V_P, and V_S inside of the Earth quite well. Comparisons of these properties, especially from the preliminary reference Earth model (PREM; Dziewonski & Anderson, 1981) and that of Fe-X alloys, were repeatedly provided. In addition to computational studies by *ab initio* calculations, a high-pressure experiment using a DAC is one of the windows to the Earth's core.

Density and its pressure dependence are often used as criteria to discuss the maximum amount of each light element (Table 1.2). The P-V equation of state (EoS) of a solid Fe-X system was well established by *in situ* XRD measurements up to core pressures except for the Fe-H system—for instance, Fe-S up to 294 GPa (Tateno et al., 2019), Fe-Si up to 304 GPa (Tateno et al., 2015), Fe-C up to 193 GPa, and Fe-O up to 265 GPa (Sata et al., 2010). P-V-T EoSs were also published (Fischer et al., 2014, 2011; Nakajima et al., 2011; Seagle et al., 2006; Takahashi et al.,

2019). On the other hand, five previous studies about the compressibility of FeH were reported up to 136 GPa (Badding et al., 1991; Hirao et al., 2004; Kato et al., 2020; Narygina et al., 2011; Pépin et al., 2014). However, the compressibilities were inconsistent with each other (Figure 1.2). Moreover, there is yet no compression experiment of sub-stoichiometric FeH*x*.

Measurements of V_P and V_S are more challenging but essential because information of density profiles is inadequate to determine the core composition uniquely. Nuclear resonant inelastic X-ray scattering (NRIXS), inelastic X-ray scattering (IXS) (Bass & Zhang, 2015), and pump-probe acoustic measurement (Wakamatsu et al., 2018) are the methods potentially able to perform experiments in the core pressure range. A comparison of V_P and V_S with PREM can constrain the maximum amount of light elements more strictly (Table 1.2). For the Fe-H system, several works were published (Mao et al., 2004; Shibazaki et al., 2012; Thompson et al., 2018), and all of the studies confirmed that hydrogen could be a significant light element in the core.

Computational studies are able to calculate ρ, V_P, and V_S at core conditions. For FeH*x* system, Caracas (2015) constructed EoSs with Vp and Vs of *hcp* FeH*x* for *x*=0, 0.0625, 0.125, 0.1667, 0.25, 0.25, 0.5, and 1 up to 400 GPa. One of the results of the work is an almost linear relation between the hydrogen content and the density change. This work also insisted that solid FeH*x* will not reconcile the V_S in the inner core, talking no account of hydrogen diffusion. On the other hand, molecular dynamics (MD) calculations would provide more reasonable results than a

static calculation because hydrogen can diffuse among sites of Fe lattice even in the solid FeH*x* at high temperatures (Fukai and Sugimoto, 1985). Umemoto & Hirose (2015) performed an MD calculation on the liquid Fe-H system, and they confirmed that Fe alloy containing ~1 wt.% hydrogen is consistent with the PREM velocity and density profile for the outer core. Note that there is no previous work calculating solid FeH*x* in the inner core conditions by MD.

Computational studies are also a powerful tool to examine a multi-component system. Badro et al. (2014) carried out calculations for ρ and V_P of Fe-O, -Si, -S, -C systems at the inner core boundary (ICB) and the core-mantle boundary (CMB) conditions, and then concluded that oxygen is necessary to explain observations related to Earth's core. On the other hand, a more recent work suggested hydrogen is the more important light element if the core temperature is low (Umemoto and Hirose, 2020).

Note that the density deficit of the outer core decreases slightly (<1.3%) using a newer reference model, EPOC (Irving et al., 2018). However, its difference among the reference models is not so significant as compared with the uncertainties in the experiments (Figure 1.3). I will use PREM as a reference model in this study following to other high-pressure studies. When EPOC was used as a reference model, the contents of each light element of the composition models could decrease by 10%. Even if hydrogen contents decrease, V_P would almost remain the same, as the dependence of V_P on hydrogen contents is small (Umemoto and Hirose, 2015).

(2) Determination of phase diagrams of Fe-X alloys in high pressures

A phase diagram enables us to discuss crystallization processes at the ICB. Which crystal structure can be solidified at the inner core and whether the Fe-X system can explain the density jump at the ICB or not, are critical to determining the amount of each light element. Furthermore, the chemical composition at a eutectic point can limit the maximum content of an impurity element in the outer core, because the outer core composition must be on the iron-rich side of eutectic in a binary system to form a denser inner core.

Except for the Fe-H system, phase diagrams of Fe-X binary systems are well-determined to core pressures (reviewed by Li & Fei, 2014). Furthermore, the recent improvement of a sample processing method using a focused ion beam (FIB) has enabled constraint on the eutectic composition up to multi-megabar pressures: Fe-S, up to 254 GPa (Mori et al., 2017); Fe-Si, up to 127 GPa (Ozawa et al., 2016); Fe-C, up to 255 GPa (Mashino et al., 2019); and Fe-O, up to 204Pa (Oka et al., 2019). The expected eutectic compositions at the ICB are gathered in Table 1.2.

For the Fe−FeH system, there is no previous work determining its phase diagram. The expected composition−temperature phase diagram of the Fe–FeH system was provided by Fukai (1992) and Shibazaki et al. (2014). Both works assumed solid solutions over the full range of concentrations (Figure 1.4). However, a stable crystal structure of FeH*x* would be more complicated. Three phases, hexagonal closed-packed (*hcp*), face center cubic (*fcc*), and double

hexagonal closed-packed (*dhcp*) have been reported for Fe-FeH binary system so far (Machida et al., 2019; Yamakata et al., 1992) up to 7 GPa. Because the maximum contents of hydrogen in the core is lower than ~1 wt.%, the stable structure of iron rich-side has attracted great attention.

(3) Metal-silicate partitioning experiments of light elements

The core formation is the main process in determining to set the composition of the Earth's core. It is widely accepted that metallic cores of accreted planetesimals were re-equilibrated with the Earth's magma ocean during its growth (*e.g.,* Wood et al., 2006). Light elements were also differentiated during this sequence. Therefore, determining the partitioning coefficients between silicate and metal could be a piece of strong evidence to determine the initial composition of the core. Recently, high pressure and higher temperature core formation scenario were proposed because it explains well the remnant concentration of moderately siderophile (iron-loving) elements in the mantle, such as Ni, Co, V, Cr. The condition was at around ~50 GPa and 3500 K assuming a single-core formation model (Fischer et al., 2015; Siebert et al., 2013; Wade and Wood, 2005). Such a condition would reflect an "average" condition of core formation. More sophisticated models of core formations also suggested that a large amount of core material was separated from the magma ocean under higher pressures (Figure 1.5) (Badro et al., 2015; Rubie et al., 2015)**.**

According to experimental results under such core formation conditions, both Si and O

were proposed as a dominant light element in the core. Fischer et al. (2015) concluded that the core would contain ~2 wt.% O and ~8 wt.% Si. On the other hand, Siebert et al. (2013) insisted that a more oxygen-rich composition, 5 wt.% O and 2 wt.% Si is likely. This disparity was ascribed to the difference in oxygen fugacities when modeling the core composition. Both models explain all of the density deficit of the present core, but they put a constraint only on the "initial" composition of the core. Because crystallization of SiO_2 and exsolution of it from the core to the mantle took place during its cooling through Earth's history (Hirose et al., 2017), a substantial amount of other light elements should exist in the present core.

Partitioning studies also revealed that sulfur would be a minor element. Suer et al. (2017) found that sulfur became less siderophile over 40 GPa because the solubility of sulfide in silicate melt increased. The work concluded that the sulfur content in the core is lower than 2 wt.%. This result is one order magnitude smaller than the previous studies carried out below 20 GPa. Additional work would be necessary to explain the difference, but this consequence can explain the estimation of sulfur content of the bulk Earth from the abundance of elements that have comparable volatilities (McDonough, 2014).

The partitioning behavior of carbon is controversial. In lower pressures, carbon seems to be the most siderophile element among the candidates (e.g., Grewal et al., 2019) but it became lithophile with pressure increase (Malavergne et al., 2019). Most recently, two groups first

reported the partitioning of carbon above 35 GPa and 3500 K and both concluded that carbon concentration in the core is minor; at most, 0.41 wt.% (Blanchard et al., 2018; Fischer et al., 2019). The amount is marginally consistent with Wood et al. (2013), which deduced the amount of carbon in the core from its effect on the metal-silicate partitioning of Mo and W.

The behavior of hydrogen during the core formation is still an open question. Pioneering experimental work has concluded that hydrogen is firmly siderophile because of the existent of voids formed by degassing molecular H_2 in quenched molten iron (Okuchi, 1997; Okuchi and Takahashi, 1997). Hydrogen content in metal was determined by the ratio between the area of the voids and iron, and that in silicate was obtained by mass balance calculation. Although its quantitative analysis would have considerable uncertainty, it is the only work to observe the nature of hydrogen partitioning between molten iron and molten silicate. The siderophile nature of hydrogen is also confirmed in the reaction between solid iron and hydrous minerals in high temperatures and ~4 GPa (Iizuka-Oku et al., 2017). Note that it was challenged by the most recent works (Clesi et al., 2018; Malavergne et al., 2019), but they likely found hydrogen atoms that had escaped from the iron lattice. They performed hydrogen measurements in metals at ambient conditions. However, hydrogen solubility decreases from 1.8 wt.% at 3.5 GPa (Badding et al., 1991) to <0.0001 wt.% at 1 bar (Okamoto, 2004). Therefore, a study should address the partition coefficient of hydrogen under the high P−T core formation conditions (Chapter 2).

(4) Mutual interactions between light elements

When studying three-or-more-component systems, mutual exclusivity or crystallization from metals could occur. It is a common phenomenon in lower temperature conditions below ~3000 K. For example, a combination of silicon and oxygen (Tsuno et al., 2013) or of silicon and sulfur (Chabot et al., 2014) is unlikely to be the core compositions of small planetesimals. Although a many-components liquid tends to show the ideal mixing at higher temperatures, mutual interactions are observed even during core-mantle equilibrium in the Earth-size planets. One of the remarkable results is the crystallization of SiO_2 in the core (Hirose et al., 2017), which is a constraint on the maximum solubility of a combination of silicon and oxygen in the present Earth's core. For the hydrogen bearing system, mutual exclusivity between carbon and hydrogen was reported, and carbon precipitated in the form of a diamond from hydrogen-bearing molten iron (Hirose et al., 2019), but other combinations with hydrogen are a still open question.

1.3 Research objective

The aim of this study is to ascertain that hydrogen could be the major light element by combining three out of the four criteria reviewed in the previous section: the metal silicate partition of hydrogen (Chapter 2), determination of the phase diagram of Fe-H (Chapter 3) and comparison of ρ, V_P, and V_S with PREM (Chapter 4). In the final chapter, I discuss the possible hydrogen contents in the present Earth's core and its validity to each core formation model.

Figures and tables

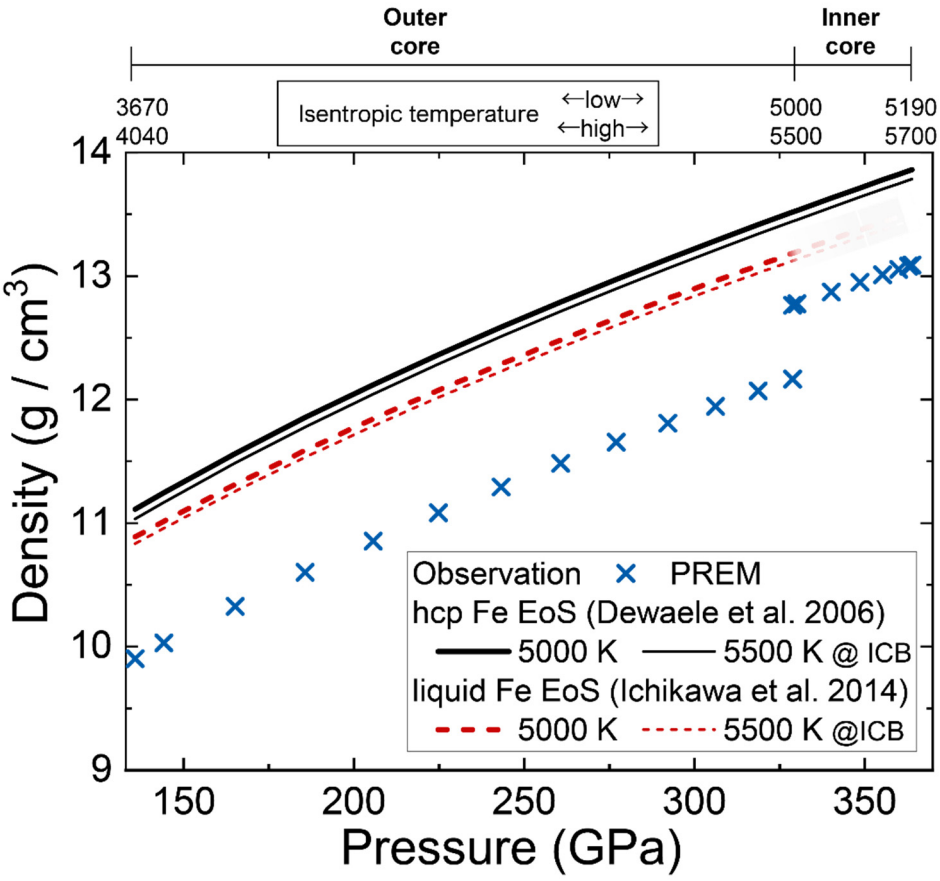

Figure 1.1 Comparison of density between pure iron and PREM in the core pressure range
Pressure vs. density plot. The blue crosses are the density of the Earth's core from PREM. Iron densities were calculated from *hcp* Fe EoS (black lines, Dewaele et al., 2006) and liquid Fe EoS (red dot curves, Ichikawa et al., 2014) on the isentropic temperature profile when the inner core temperature is 5000 K (thick lines) and 5500 K (thin lines). In this calculation, thermodynamic stability was not considered, although pure liquid iron would crystalize on the P-T paths. The density deficit is around 5–10% at the outer core and 3–5% at the inner core. Note that the EoS of solid is practically adaptable to comparison with the density in the outer core because the volume difference of solid and liquid iron is small (~2%) under outer core pressures (Ichikawa et al., 2014).

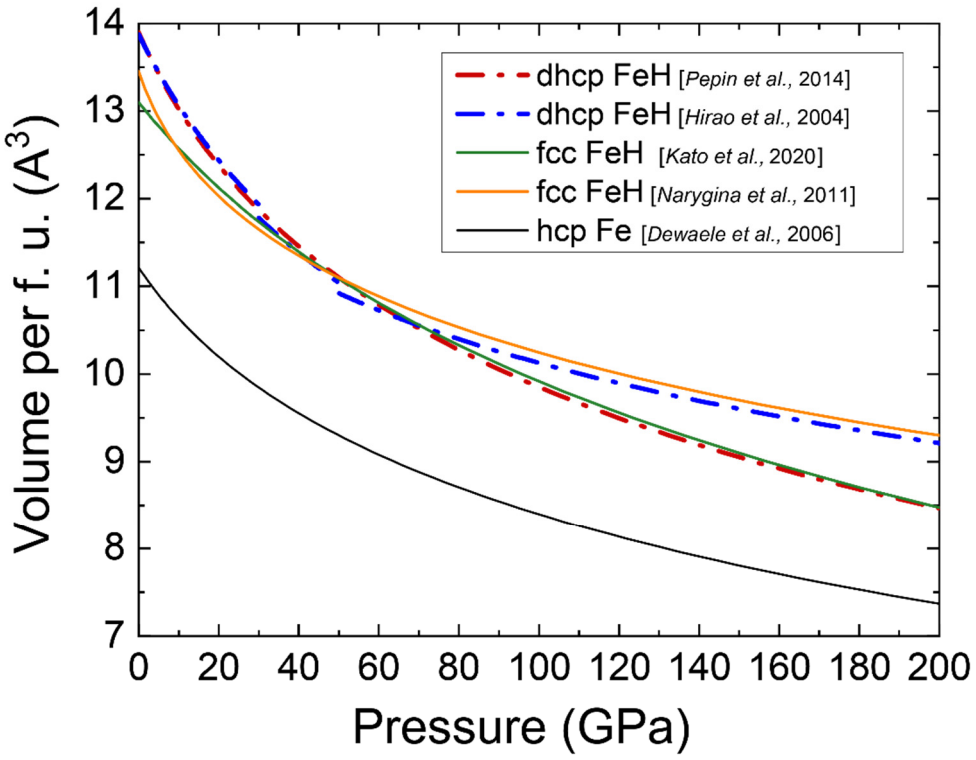

Figure 1.2 Comparison of the compression behavior of FeH reported in previous studies
Four previous studies were reported for *dhcp* FeH (red dot-dash line, Pépin et al., 2014; blue dot-dash line, Hirao et al. 2004) and *fcc* FeH (green line, Kato et al., 2020; orange line, Narygina et al., 2011). At over 135 GPa, the density difference calculated from each EoS was larger than 6%. As a reference, the compression curve of *hcp* Fe was also shown (black dashed line, Dewaele et al., 2006).

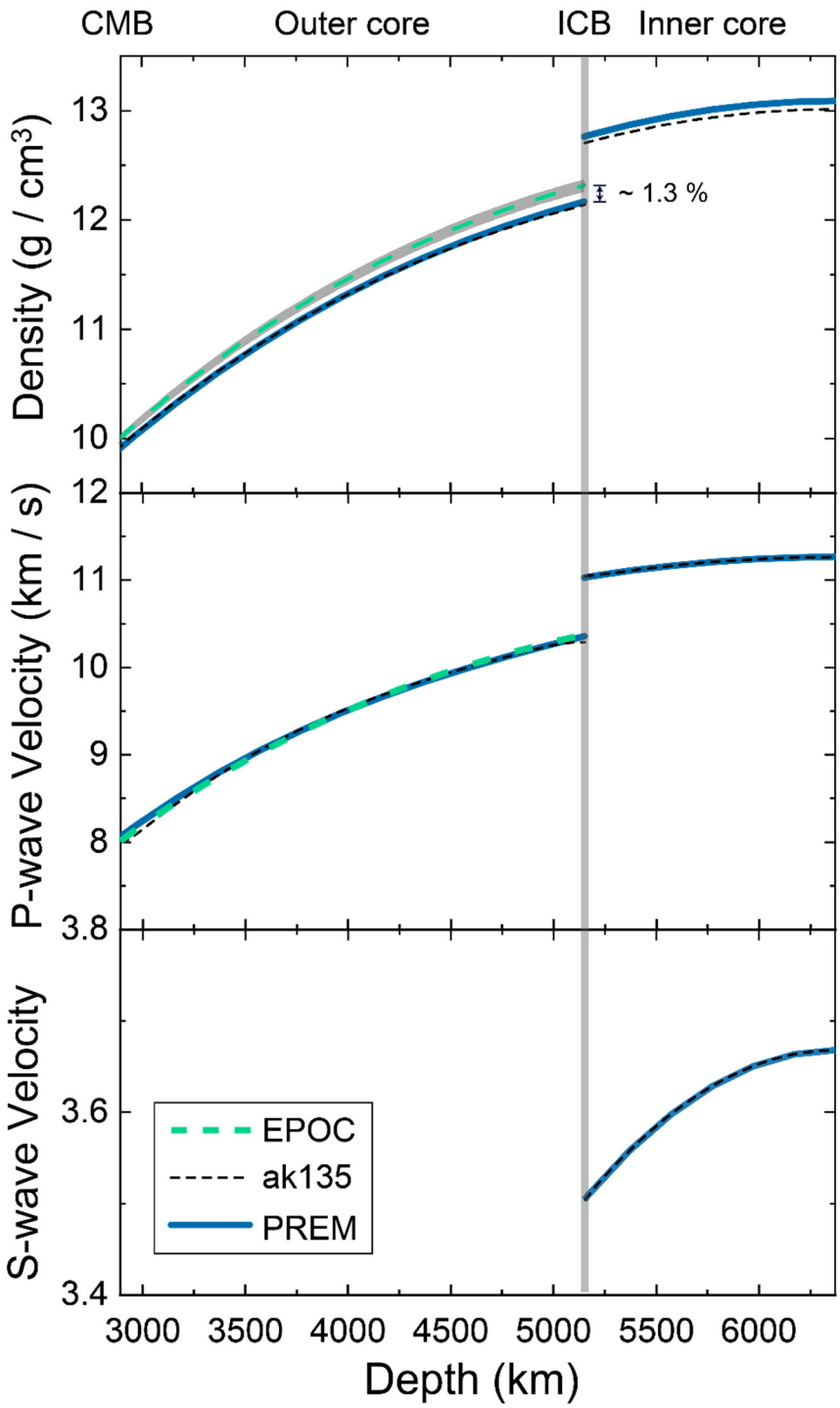

Figure 1.3 Comparison of one-dimensional reference models of the interior of the Earth
Depth (km) vs. ρ (g/cm^3) (upper panel), Vp (km/s) (middle panel), and Vs (km/s) (lower panel) plots. Green dot curves, black dot curves, and blue curves show the value from EPOC (Irving et al., 2018), ak135 (Kennett et al., 1995), and PREM (Dziewonski and Anderson, 1981), respectively.

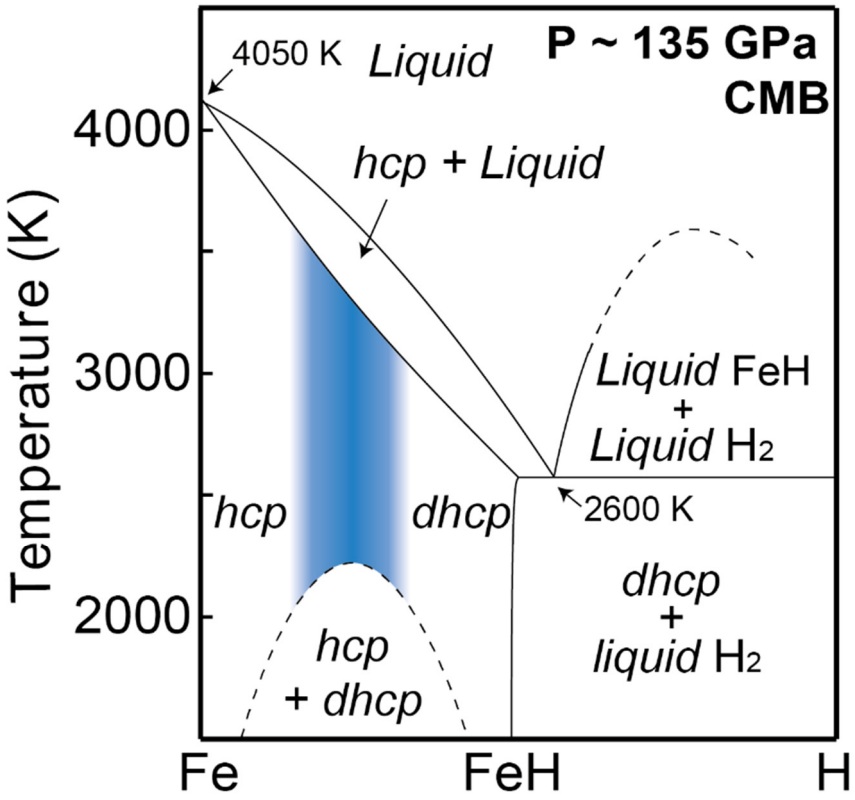

Figure 1.4 Expected phase diagram of the Fe-H system at ~135 GPa proposed by Fukai (1992)

It is widely accepted that the Fe-FeH system has a solid solution in the full region between Fe and FeH. The melting temperature of the FeH is low (Sakamaki et al., 2009), and *dhcp* is regarded as a stable crystal structure in this area. Fukai (1992) proposed the continuous phase changing between *hcp* (Fe) and *dhcp* (FeH) because of random stacking fault formation at high temperatures (blue region).

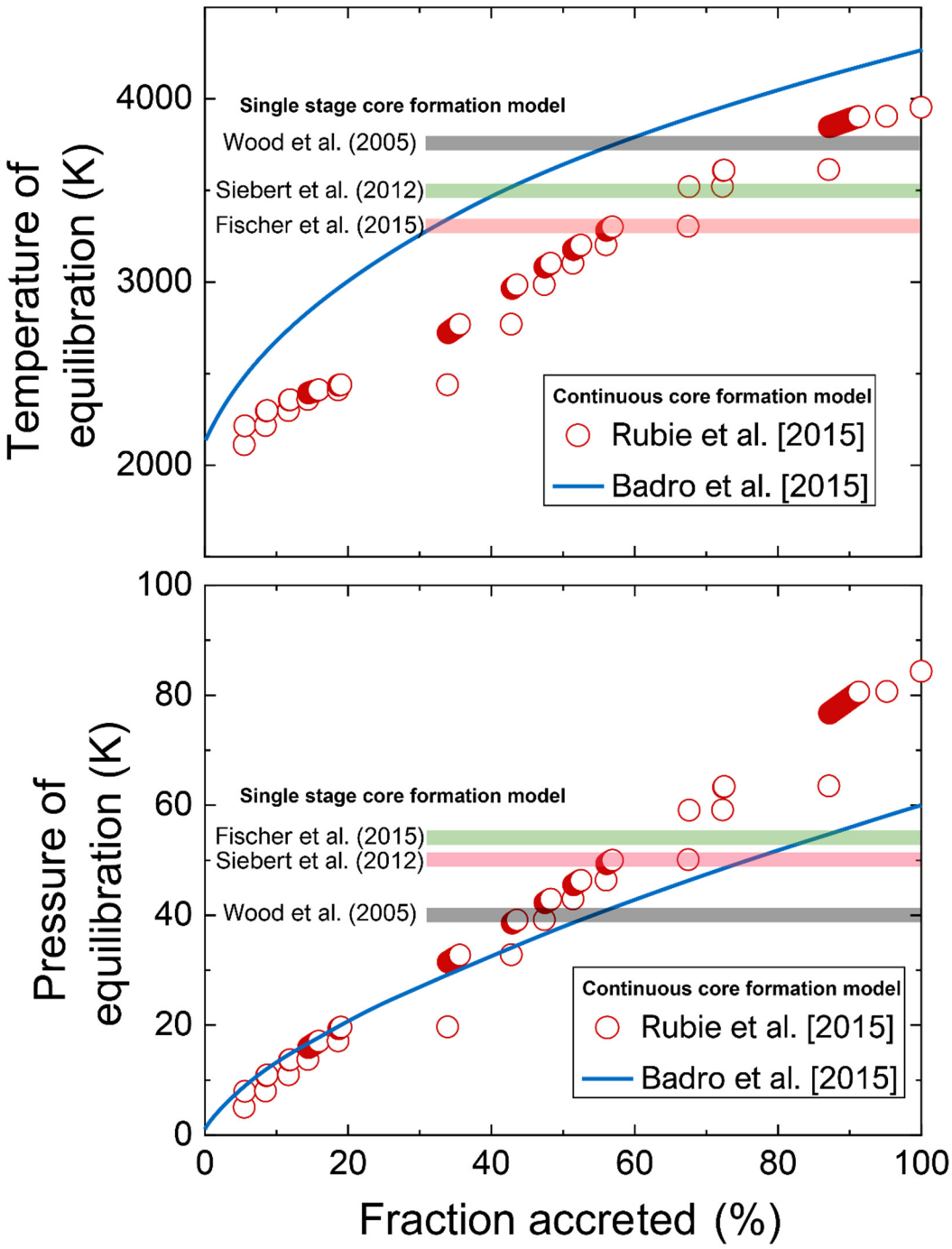

Figure 1.5 Example of core partitioning equilibration conditions for a scenario from Badro et al. (2015) and Rubie et al. (2015)

The blue line and red circles correspond to model outputs from Badro et al. (2015) and one of a case by Rubie et al. (2015), respectively. These models assume the continuous or multi-stage core formation model, which develops the equilibration conditions of core and mantle as a function of the fraction accreted. Note that the outputs explain the present mantle contents of Ni, Co, V, and Cr. The conditions calculated from the single-core formation models are also plotted.

Table 1.1 Geochemical and cosmochemical reasons which support each light element candidate in the core

Elements	Reasons	Key references
Hydrogen	A) Iron and water reaction during the core formation.	(Iizuka-Oku et al., 2017; Okuchi and Takahashi, 1997)
	B) The significant water content of C-chondrites, one of the main building components of the Earth.	(Alexander, 2019)
	C) Hydrogen ingassing from the nebular gas.	(Ikoma and Genda, 2006)
Silicon	A) Superchondritic Mg/Si ratio of the bulk Earth (Missing silicon problem).	(Allègre et al., 1995)
	B) The difference in Si isotopic composition between the mantle and chondrites.	(Georg et al., 2007)
	C) The high solubility to Fe in reductive core formation conditions and formation of solid solution with iron even in low pressures.	(*e.g.* Fischer et al., 2015)
Oxygen	A) Strong partitioning between liquid and solid iron, which could explain the density jump across the ICB.	(Alfé et al., 2002)
	B) The high solubility of oxygen into iron in oxidative core formation conditions.	(Siebert et al., 2013)
Sulfur	A) Depletion in the crust and mantle relative to other volatile elements, such as halogens and rare gases.	(Rama Murthy and Hall, 1970)
	B) Incorporation of a large amount of sulfur in iron meteorites due to its siderophile behavior.	
	C) Significant melting point depressions near the eutectic compositions.	(Mori et al., 2017)
Carbon	A) Siderophile behavior in low pressures.	(Dasgupta et al., 2013)
	B) Low V_S of Fe_7C_3, which most closely matches the observed V_S of the inner core.	(Chen et al., 2007)
	C) Superchondritic H/C of the bulk Earth.	(Hirschmann, 2016)

Table 1.2 Proposed light element contents (wt.%) in the core

Grounds for estimate	Hydrogen	Silicon	Oxygen	Sulfur	Carbon	References
Studies assuming a single light element (or a maximum abundance of each element)						
Density (Experiments)	1	12	8	12	7	Li and Fei (2014)
	–	12.5	7.7	12.1	7.7	Sata et al. (2010)
	0.5-1.5	–	–	–	–	Narygina et al. (2011), Pépin et al. (2014)[a]
V_P (IXS for liquids)	–	–	–	7.5	1.2	Nakajima et al. (2015), Kawaguchi et al. (2017)
V_P and density	–	4.5	5.4	2.4	4	Badro et al. (2014)
Ab initio calculation	1	9.8	8.9	14.4	2.6	Umemoto and Hirose (2015, 2020)[b]
Eutectic composition	Unknown	<1.5	–[c]	6	3	Mashino et al. (2019), Mori et al. (2017), Oka et al. (2019), Ozawa et al. (2016)
Density Jump at the ICB	–	6	3	7	–	Alfé et al. (2002)
Metal-silicate partitioning	1.2	–	–	2	0.41	Okuchi (1997), Suer et al. (2017), Fischer et al. (2019)
Core composition models considering multiple light elements						
Geochemical constraint	–	7	5	1.21	–	Allègre et al. (2001)
	600 ppm	6	0	1.9	0.2	McDonough (2014)
Core formation modeling	10 – 60 ppm	8–9	2–4	–	–	Rubie et al. (2015)

[a] Thermal expansivity was assumed to be the same as that of pure iron (Dewaele et al., 2006).

[b] T_{CMB} is 5400 K.

[c] Sufficiently larger than the maximum content of oxygen in the core.

Chapter 2. Partitioning of hydrogen between Earth's core and mantle

This chapter has been prepared and submitted as a manuscript named in *"Core-mantle partitioning of hydrogen"* by ***Shoh Tagawa***, *Naoya Sakamoto, Kei Hirose, Hisayoshi Yurimoto, and Yasuo Ohishi.*

Abstract

In Chapter 2, I will report the partitioning experiments of hydrogen between molten iron and silicate melt under the Earth's core formation conditions. High-pressure and -temperature experiments using a laser-heated diamond anvil cell (LH-DAC) was performed at 30–60 gigapascals and 3100–4600 kelvin, corresponding to the conditions of single-core formation models. *In situ* XRD measurement and SIMS analysis demonstrate the high siderophile (iron-loving) nature of hydrogen even under such high pressures and temperatures. If core-forming metals were in equilibrium with the silicate Earth, containing about 700 ppm H_2O before degassing water that later formed oceans, the core might include 2900–5300 ppm H; this explains ~30–50% of the density deficit and the velocity excess of the outer core relative to pure iron. It also suggests that 25–66 times the ocean's mass of water was delivered to the Earth by the time of core formation.

2.1 Introduction

The amount of hydrogen in the core is essential to understanding light element abundances of the bulk Earth. As reviewed in Chapter 1, the metallic core is known to include substantial amounts of light elements and could be the most significant "reservoir" of hydrogen on Earth. The incorporation of hydrogen from water in a magma ocean into core-forming metals produces FeO from metallic Fe, which likely determines the FeO content of the mantle (Righter et al., 2014). The mantle abundances of moderately siderophile elements indicate that core-forming metals segregated from molten silicate (a magma ocean) at 40–60 GPa and 3000–4000 K (Fischer et al., 2015; Siebert et al., 2012; Wade and Wood, 2005, Figure 1.5). Therefore, the metal-silicate partitioning behavior of hydrogen under such high-pressure and -temperature (P-T) conditions would tell us the hydrogen concentration in the core, if the average H_2O content in the silicate Earth is assumed. The hydrogen content in the core also suggests how much water is brought to our planet in its growing stage (Chapter 1.1).

However, previous experimental studies on the metal-silicate partitioning of hydrogen performed below 20 GPa have been highly controversial because determination of the hydrogen (or water) contents in coexisting metallic iron and silicate are technically difficult. While the highly siderophile nature of hydrogen was reported under high pressure (Iizuka-Oku et al., 2017; Okuchi, 1997; Shibazaki et al., 2009), it was challenged by the most recent experiments (Clesi et

al., 2018; Malavergne et al., 2019). In these studies, the hydrogen concentration in metal was obtained ex-situ elastic recoil detection analysis (ERDA) after samples were recovered at ambient conditions. However, FeH*x* decomposes into bcc Fe and molecular H_2 below ~ 3 GPa (Iizuka-Oku et al., 2017); the equilibrium hydrogen solubility in bcc Fe at an H_2 pressure of 1 bar is limited to x (= H/Fe) < 10^{-5} (Fukai and Suzuki, 1986). Therefore, it is most likely that they found hydrogen atoms that had escaped from the iron lattice (Iizuka-Oku et al., 2017) and had been mechanically trapped in grains (Okuchi, 1997). Therefore, in order to quantify the hydrogen amount in metal parts, *in situ* (under high pressure) measurements are preferable. Besides, the measurement of hydrogen contents in silicate parts is also challenging because of its small size.

In this work, I determined the partition coefficients of hydrogen, between liquid iron and silicate melt at 30–60 GPa and 3100–4600 K (Table 2.1), using a laser-heated diamond-anvil cell (LH-DAC), which covers conditions previously proposed for Earth's core formation (Figure 1.5). The challenge of precisely quantifying the hydrogen content in DAC samples is addressed by combining i*n situ* XRD measurements and SIMS, a procedure established for this study. The partitioning coefficient of hydrogen was parameterized as a function of pressure, temperature, and oxygen fugacity. Then, I applied the partitioning function to single-core formation models, in order to estimate the minimum content of hydrogen in the Earth's core.

2.2 Methods

(1) Starting materials

Pure iron foil (5N, Mairon-UHP, *Toho Zinc*) and hydrous MORB glass were used as starting materials. The MORB glasses containing about 0.2 and 1.0 wt.% H_2O were synthesized by using a piston-cylinder apparatus. Their major element composition is similar to the one employed in previous experimental studies (Hirose et al., 1999; Tateno et al., 2018) (Table 2.2). The water contents in these glasses were confirmed with SIMS analyses (see below).

(2) High-pressure and -temperature experiments and *in situ* XRD measurement

High *P*-*T* experiments were performed in a laser-heated diamond-anvil cell (DAC) with flat 300 μm culet diamond anvils. An iron foil (5–7 μm thick) was sandwiched between hydrous MORB glass powder, and they were loaded into a hole at the center of a pre-indented Re gasket (Figure 2.1). Except for run #1, MORB glass with ~1.0 wt.% H_2O is used. In run #1, a mixture of MORB glasses with ~0.2 and ~1.0 wt.% H_2O was employed. After loading the sample, a whole DAC was dried in a vacuum oven at 400 K for 3 to 8 hrs. As soon as the DAC was taken out from the oven, then immediately compression was started.

The sample was heated at high pressure, with collecting *in situ* XRD data at BL10XU of SPring-8. Heating was made from both sides with a couple of 100 W single-mode Yb fiber lasers (*SPI photonics*). A laser beam was converted to the one with a flat-top distribution by beam

shaping optics (*New focus*). The laser spot size was around 40 μm. The heating duration was limited to 3 sec to avoid temperature fluctuation that possibly causes complex melting textures. It is indeed long enough for each element to diffuse in liquid metal (Helffrich, 2014) and silicate (de Koker et al., 2008). Time-series experiments on element partitioning in a DAC also show that partition coefficients did not change after heating for 1–2 sec (Tateno et al., 2018). The temperature was measured by a spectroradiometric method, and a one-dimensional radial temperature profile was obtained across a laser-heated spot with 1 μm resolution. In this study, the boundary of metal and silicate liquid would be along with isotherm. Its boundary is closest to the sample surface at the center of the heating spot. Therefore, the experimental temperature was represented by an average in 6 μm of the center of the heating spot, corresponding to the size of an x-ray beam. Sample pressure was determined from the Raman shift of a diamond anvil (Akahama and Kawamura, 2004) at the center of the heating spot in ambient temperature after heating. I added a contribution of thermal pressure that has been estimated to be +2.5 GPa/1000 K (Andrault et al., 2011; Tateno et al., 2018). Temperature and pressure uncertainty may be ±5% and ±10%, respectively (Mori et al., 2017).

XRD patterns were collected before/during/after heating in each run (Ohishi et al., 2008). A monochromatic x-ray beam with an energy of ~30 keV was focused on a 6 μm area (full-width of half maximum) on a sample position. The XRD data were collected every 0.22 sec during

heating on a flat panel detector (*Perkin Elmer*). Two dimensional XRD image was integrated into a one-dimensional pattern and analyzed using a software suite (Seto et al., 2010).

(3) SIMS analysis for the hydrogen content in silicate melt

After recovering a sample from DAC at ambient condition, its cross-section at the center of a laser-heated portion was prepared parallel to the compression/laser-heating axis by using a dual-beam focused ion beam (FIB, Versa 3D^{TM}, *FEI*). Textural observation and preliminary compositional characterization were made with a field-emission-type scanning electron microscope (FE-SEM) and an energy-dispersive x-ray spectrometry (EDS) with a silicon drift detector (*Bruker*) in the dual-beam FIB system.

Subsequently, the hydrogen content in a quenched silicate melt was determined with an isotope microscope system installed at the Hokkaido University, which is composed of *CAMECA* ims-1270 SIMS and a two-dimensional ion detector, SCAPS (stacked CMOS-type active pixel sensor) (Yurimoto et al., 2003). This system provides quantitative maps of secondary ions emitted from the sample surface (e.g., Greenwood et al., 2011; Sakamoto et al., 2007), because the CMOS sensor exhibits a good linear relationship between an output voltage and the number of secondary ions (Yamamoto et al., 2010). Therefore, this technique is capable of quantifying the abundance of each isotope from the intensity map.

Two-dimensional images of $^{1}H^{+}$, $^{28}Si^{+}$, and $^{40}Ca^{+}$ with 0.5 to 1.2 μm spatial resolution for $^{1}H^{+}$ were collected using the $^{16}O^{-}$ primary beam (13 KeV, 37 nA) that was focused to 20–30 μm in diameter and rastered across a 100 μm × 100 μm region on the sample surface. The contrast aperture was set to be 100 μm in diameter and the exit slit fully opened. In order to minimize the effect of adsorbed water on the sample surface, the energy slit was ±20 eV to select kinetic energy ranges of secondary ions from 80 eV to 120 eV by loading sample offset voltage of -100 V. This procedure enables us to separate secondary ions of ^{1}H originated in a sample from adsorbed water. The pressure during measurements was at 6.5–8 × 10^{-8} Pa. Secondary ion images of $^{1}H^{+}$, $^{28}Si^{+}$, and ^{40}Ca were obtained sequentially in the following order; $^{28}Si^{+}$, $^{1}H^{+}$, $^{28}Si^{+}$, $^{1}H^{+}$, $^{28}Si^{+}$, and $^{40}Ca^{+}$. Accumulation time was 500 and 100 sec in each image, and two and three images were combined to calculate concentration maps for $^{1}H^{+}$ and $^{28}Si^{+}$, respectively.

The hydrogen concentration in a quenched silicate melt was determined from the $^{1}H/^{28}Si$ intensity ratio using a calibration curve established by three standards of Basalt or Rhyolite silicate glasses with known H_2O concentrations (0.00 to 4.5 wt.%) (Yoshimura, 2015). The analyses of these standards provide a linear relationship between the counts of $^{1}H/^{28}Si$ and the known H_2O contents with a correlation coefficient $R^2 = 0.996$ (Figure 2.2). A detection limit of H_2O would be 15 ppm from its y-intercept. These standards were measured before, during, and after the analysis of each DAC sample. In order to reduce statistical errors for each DAC sample,

regions of interest (ROIs) were selected on the quenched silicate melt portion. The area of ROIs in each sample was shown in Table 2.1. Combining the $^{1}H/^{28}Si$ intensity ratio with the Si content obtained by an FE-EPMA (see below), hydrogen (water) concentration in silicate melt was determined (Table 2.1). The uncertainty of water content in silicate melt was from ±2 to ±7%, mainly due to the distribution of hydrogen content in the ROIs.

(4) Chemical analysis with EPMA

The major element compositions, except hydrogen, of both quenched liquid metal and silicate melt were determined by field-emission-type electron microprobe (FE-EPMA, JEOL JXA-8530F). Analyses were performed with an acceleration voltage of 12 keV and a beam current of 15 nA. For metal, I used an electron beam diameter of 1 μm, Fe, Al_2O_3, Ni_2Si, and Mg as standards, and LIFH (Fe), LDE1H (O), PETJ (Si), and TAP (Al, Mg) as analyzing crystals. For silicate, the standards were SiO_2, TiO_2, Al_2O_3, Fe_2O_3, MgO, $CaSiO_3$, $NaAlSi_3O_8$, and $KAlSi_3O_8$, and the analyzing crystals were TAP (Si, Mg, Na), PETJ(Ti, K), TAPH (Al), LIFH (Fe), and PETH (Ca). I employed the EDS analyses of oxygen and silicon only for run #2 because the metal part was sputtered out during SIMS analyses.

2.3 Results

(1) General appearance, SEM-EDS mapping, EPMA analysis

SEM-EDS maps for a typical cross-section of a sample are shown in Figure 2.3. An Earth-like structure, a central metallic blob, and a surrounding quenched silicate melt are found in every run product. A Ca-Pv layer surrounds them as a liquidus phase. This sample appearance is consistent with previous liquid metal and liquid silicate experiments using an LH-DAC (e.g., Fischer et al., 2015). The chemical compositions except for hydrogen of the coexisting metal and silicate were determined with a FE-EPMA (Tables 2.2 and 2.3).

(2) The hydrogen contents in metal

Since hydrogen escapes from solid iron during decompression when it transforms into bcc Fe (Fukai and Suzuki, 1986; Iizuka-Oku et al., 2017), the hydrogen concentration in quenched liquid metal must be obtained at high pressure. *In situ* XRD measurements show that molten iron crystallized FeH_x and minor FeOOH upon quenching temperature (Figure 2.4). Earlier experiments demonstrated that thermal annealing of such FeH*x* quench crystals changed their unit-cell volume only little; hydrogen content *x* derived from the lattice volume (see below) decreased from 1.21 to 1.14 upon heating to ~1500 K and 65 GPa (Hirose et al., 2019). It indicates that an amorphous part was not present in quenched liquid iron even without thermal annealing and FeH*x* + minor FeOOH well represents the bulk hydrogen concentration in metal in this study.

The hydrogen content in molten iron was therefore determined from 1) the proportions of solid FeH*x* and FeOOH in quenched liquid iron and 2) the *x* value in FeH_x that is calculated from its unit-cell volume at high pressure (Table 2.1).

Hcp $FeH_{x>1}$ and *fcc* $FeH_{x<1}$ were formed in run #4 and all other runs, respectively. Since hydrogen expands the lattice volume (V) of Fe, the hydrogen concentration in FeH*x* can be obtained (Fukai, 1992) as;

$$x = (V_{\mathrm{FeH}_x} - V_{Fe}) / \Delta V_{\mathrm{H}} \quad \text{(eq. 2. 1)}$$

where ΔV_{H} is the volume increase per hydrogen atom by Caracas (2015), which is consistent with recent neutron diffraction data (Ikuta et al., 2019; Machida et al., 2014) and compressibility of FeH (Chapter 3). The volume of pure Fe is from Dewaele et al. (2006) for *hcp* and from Tsujino et al. (2013) for fcc. The *x* value was found to be homogeneous in a metal pool.

The unit-cell volume of ε-FeOOH was similar to that observed in recent high-pressure studies at equivalent pressure (Thompson et al., 2017). Since FeO was not observed, the proportions of FeH*x* and FeOOH are estimated from the Fe and O contents in quenched liquid iron that were obtained by EPMA analyses (see below). The total amount of hydrogen in the molten iron is shown in Table 2.1 and Figure 2.5 for each run. The present experiments found 5300 to 26000 ppm H (in weight) in metal at high pressures (before decompression) and confirmed the iron-loving nature of hydrogen.

(3) The hydrogen contents in silicate

The hydrogen concentration in a quenched silicate melt was determined from the $^{1}H/^{28}Si$ intensity ratio from a high-resolution imaging technique with SIMS (Figure 2.6). This procedure enabled not only imaging the isotopes but also quantitative compositional analysis of a small DAC sample. The imaging maps showed that the spatial distribution of hydrogen in the silicate melt was sufficiently small. The amount was 90 to 470 ppm H (present as water) by measuring recovered samples (Figure 2.7), which is comparable to that of recent studies (Clesi et al., 2018; Malavergne et al., 2019). Note that the temperature gradient generated by laser heating would not affect the measurement because hydrogen distribution in silicate melt parts is almost homogeneous in the SIMS analysis.

(4) Partitioning coefficient of hydrogen

The metal/silicate partition coefficient of hydrogen $D_{\mathrm{H,weight}}^{metal/silicate}$ (weight fraction basis) was defined as;

$$D_{\mathrm{H}}^{metal/silicate} = \mathrm{C}_{\mathrm{H,weight}}^{metal} / \mathrm{C}_{\mathrm{H,weight}}^{silicate} \quad \text{(eq. 2. 2)}$$

where $\mathrm{C}_{\mathrm{H,weight}}^{metal}$ was the weight fraction of hydrogen in metal and $\mathrm{C}_{\mathrm{H,weight}}^{silicate}$ was the weight fraction of hydrogen in silicate. The value was ranged from 29 to 57 (Figure 2.8, Table 2.1), indicating that hydrogen is highly siderophile under high pressure.

2.4 Discussion

(1) Parameterizing hydrogen metal–silicate partitioning

In order to discuss the behavior of hydrogen under the core segregation, considering the reaction reaching chemical equilibrium and parameterizing its equilibrium constant with thermodynamic variables are necessary. The metal-silicate partitioning of hydrogen is governed by the reaction;

$$\mathrm{HO}_{0.5}^{silicate\ melt} + \frac{1}{2}\mathrm{Fe}^{metal} = \mathrm{H}^{metal} + \frac{1}{2}\mathrm{FeO}^{silicate\ melt} \quad \text{(eq. 2. 3)}$$

Its exchange coefficient K_D is defined as functions of P and T with regression constants a, b, c;

$$\log_{10} K_\mathrm{D} = \log_{10} \frac{a_\mathrm{H}^{metal}}{a_{\mathrm{HO}_{0.5}}^{silicate}} \cdot \sqrt{\frac{a_\mathrm{FeO}^{silicate}}{a_\mathrm{Fe}^{metal}}} = \log_{10} \frac{D_\mathrm{H}}{\sqrt{D_\mathrm{Fe}}} = \log_{10} D_\mathrm{H} + \frac{1}{4}\Delta\mathrm{IW} = a + \frac{b}{\mathrm{T}} + c \cdot \frac{\mathrm{P}}{\mathrm{T}} \text{(eq. 2.4)}$$

where a_X represents the activity of component X. Note that D_Fe can be written as the oxygen fugacity relative to the iron-wüstite buffer; $\Delta\mathrm{IW} = 2\log_{10}\left(a_\mathrm{FeO}^{silicate}/a_\mathrm{Fe}^{metal}\right) = 2\log_{10}(1/D_\mathrm{Fe})$.

In metal-silicate partitioning studies performed at over 30 GPa, $a_x^{Silicate}$ was assumed to $x_\mathrm{X}^{silicate}$, the mole fraction of X, due to insufficient data to evaluate the activity coefficients (Fischer et al., 2015; Siebert et al., 2012). This work also uses this assumption. However, because of the high mole fraction of hydrogen in metal, a_X^{metal} cannot assume x_X^{metal} simply. The hydrogen mole fraction in metal is from 0.19 to 0.54 in the present study. This large hydrogen mole fraction significantly decreases the molar fractions of Fe and O in metal. Also, it apparently increases oxygen fugacity $\Delta\mathrm{IW} \approx 2\log_{10}\left(x_\mathrm{FeO}^{silicate}/x_\mathrm{Fe}^{metal}\right)$ and decreases the exchange

coefficient $K_{\mathrm{D}}^{\mathrm{O}} = \frac{x_{\mathrm{Fe}}^{metal} x_{\mathrm{O}}^{metal}}{x_{\mathrm{FeO}}^{silicate}}$ for the reaction $\mathrm{FeO}^{\mathrm{silicate}} = \mathrm{Fe}^{\mathrm{metal}} + \mathrm{O}^{\mathrm{metal}}$.

In order to find a way to approximate a_{X}^{metal}, I obtained the $K_{\mathrm{D}}^{\mathrm{O}}$ values from this study using molar fractions of iron and oxygen in metal, with and without considering the presence of hydrogen. They are compared with the results of Fischer et al. (*2015*) that were determined in the absence of hydrogen (Figure 2.9). The present K_D^{O} values that do not take hydrogen into account are closer to their data, suggesting that hydrogen does not have colligative properties in an iron solvent. It is likely because the incorporation of small H atoms in liquid Fe is interstitial rather than substitutional, unlike other larger atoms (Umemoto and Hirose, 2020). Thus, in this study, the activity of element *i* in metal was approximated as: $x'_i = \frac{N_i}{\sum_{k \neq H} N_k}$. Note that this formulation has been conventionally used for elements except hydrogen in solid metal-hydrogen systems. I apply it also for H in liquid metal because the H-H interaction should be negligible in liquids.

The best fitting to the data to the hydrogen's exchange coefficient K_{D} yields $a = 2.42(18)$, $b = -2892(433)$, and $c = -32.0(87)$ (Figure 2.10). Note that these constants were obtained using only my data because linear regression with data in previous studies does not converge. The slope on a plot $\log_{10}D$ vs. ΔIW obtained with this formulation indicates the valence state, n, of 0.999 for hydrogen in the silicate melt (Figure 2.11), which supports the validity of the present estimate of the activities of elements in metal and silicate. Our experiments also give $\log_{10}K_{\mathrm{D}}^{\mathrm{O}} = d + e/T$, where $d = 0.37(18)$ and $e = -1535(687)$.

(2) Hydrogen content in the Earth's core

It is known that single-stage core formation models (Fischer et al., 2015; Siebert et al., 2012; Wade and Wood, 2005) reconcile the mantle abundances of moderately siderophile elements with core-mantle chemical equilibration around 50 GPa and 3500 K and oxygen fugacity relevant to the FeO content in the mantle. Therefore, the hydrogen concentration in the core can be estimated from the exchange coefficient K_D (Eq. 2.4) under such high *P-T* conditions. Here I assumed that the "bulk silicate Earth (BSE)" is KLB-1 composition (Takahashi, 1986) with water, which was in chemical equilibrium with core-forming metals. The water abundance of the "BSE" may be the sum of those in the present-day mantle (average 291 ppm H_2O) (Hirschmann, 2016) and crust + oceans + atmosphere that holds 1.6×10^{24} g H_2O (equivalent to 396 ppm) (Lécuyer et al., 1998), which corresponds to 2 times the ocean's mass of water (OM) (total 687 ppm in the "BSE"). If this is the case, $D_{\mathrm{H}}^{metal/silicate}$ = 46.2 for 50 GPa/3500 K and ΔIW= -2.3 gives 0.36 wt.% H in the core (Figure 2.12). At a range of *P-T* conditions for core-mantle equilibration (Fischer et al., 2015; Siebert et al., 2012; Wade and Wood, 2005), the core may include 0.29–0.53 wt.% H. Since both the density and velocity of the outer core are explained by those of liquid Fe containing 1.0 wt.% H (Umemoto and Hirose, 2015), the 0.29–0.53 wt.% H accounts for ~30–50% of the density deficit and the velocity excess of the liquid core with respect to pure iron, indicating that hydrogen is an important light element in the core. These estimates depend largely

on the average H_2O content in the present-day mantle; it can be as low as 100 ppm, which is the same as that in the MORB source mantle (Dixon et al., 2002), or much higher than the 291 ppm considered above (Marty, 2012; Palme and O'Neill, 2014; Peslier et al., 2017) (Figure 2.12).

The consequence of the single-core formation scenario would yield near the minimum value of the hydrogen contents in the core if water existed in the magma ocean. Figure 2.13 shows the comparison of D_H with other core formation scenarios (Badro et al., 2015; Rubie et al., 2015). Although the lower pressure part of P–T path of Rubie's model lies in the region where D_H is lower than 40, the lowest D_H in the single-core formation model, 60% of core materials were separated from magma ocean under the condition D_H >40 (wee the supplementary table of Rubie et al. (2015)). Therefore, the difference in core formation models would not affect my conclusion.

The 0.29–0.53 wt.% H in the core is equivalent to the amount of hydrogen included in 35–65 times the amount of seawater (OM) (Figure 2.12). Besides, the "BSE" includes 2 OMs (see above). On the other hand, it is possible that <1 to 12 OMs were formed by oxidizing hydrogen in a nebular gas and incorporated into the magma ocean (Ikoma and Genda, 2006; Olson and Sharp, 2019). Therefore, 25–66 OMs, corresponding to 0.6–1.6% of the Earth-mass, may have been brought to our planet by the time of core formation as a main building block of the Earth. Indeed, the delivery of tens to hundreds of times OMs to the growing Earth has been supported by recent planet formation models (Raymond et al., 2007; Sato et al., 2016; Walsh et al., 2011).

Figures and tables

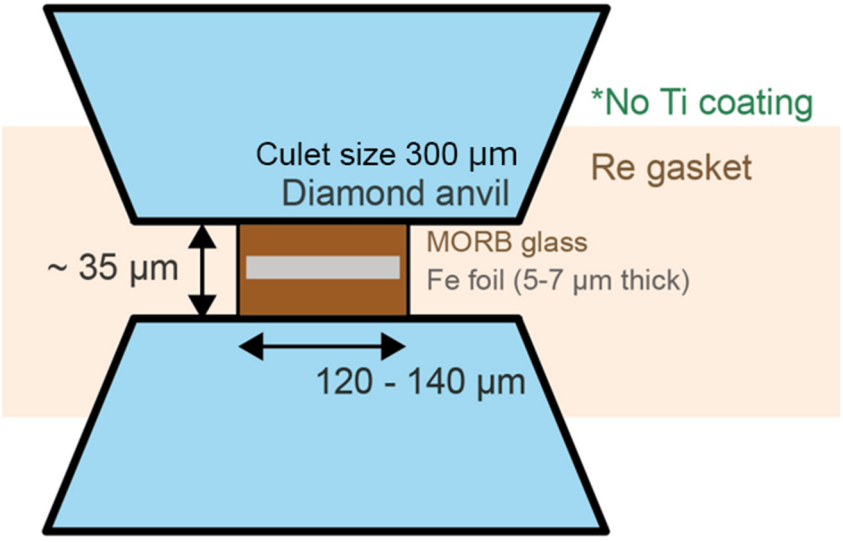

Figure 2.1 Sample configuration

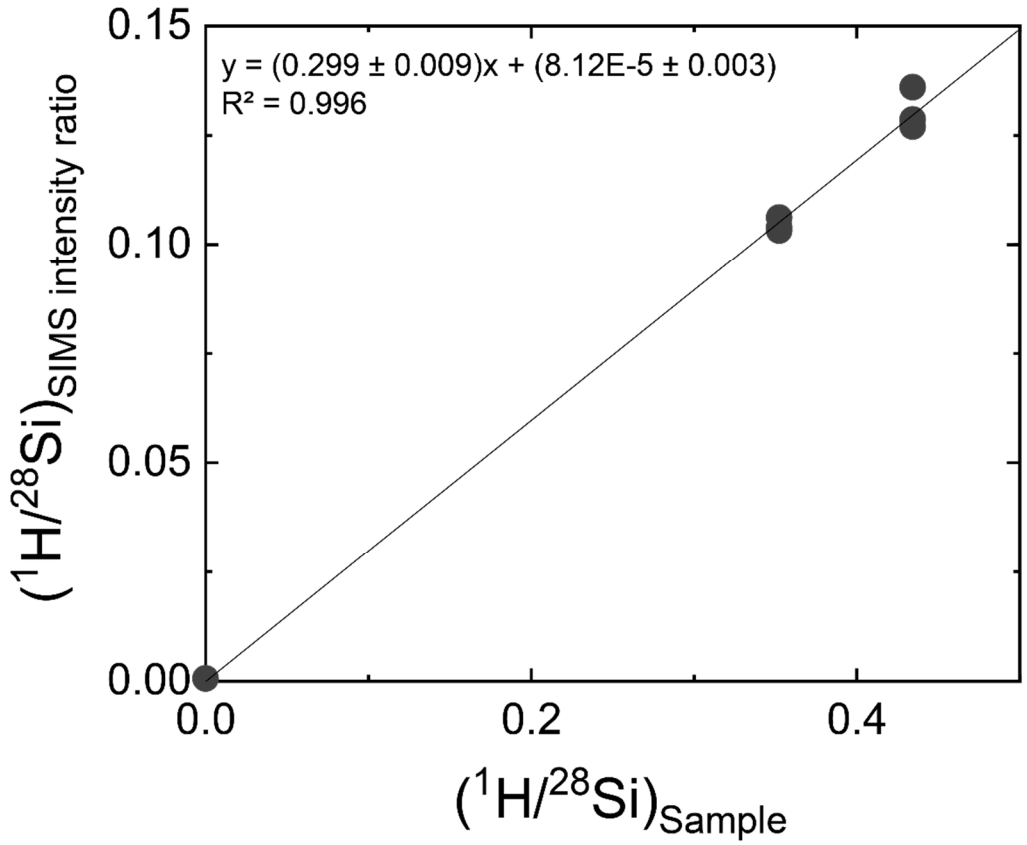

Figure 2.2 Calibration curve for the SIMS analysis of $^{1}H/^{28}Si$ based on standard glasses

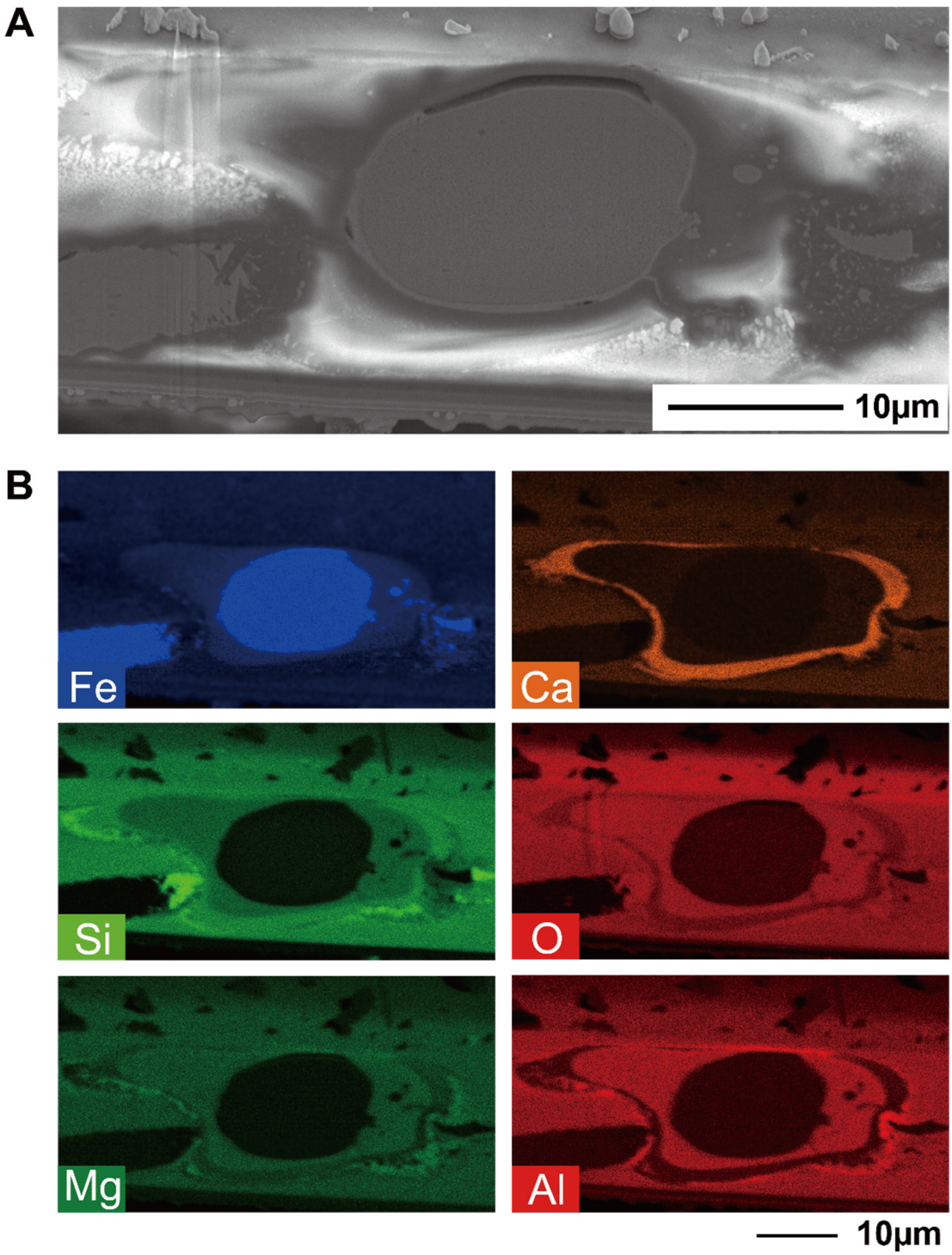

Figure 2.3 Sample cross-section for run #1

(A) Backscattered electron image and (B) x-ray elemental maps for Fe, Ca, Si, O, Mg, and Al.

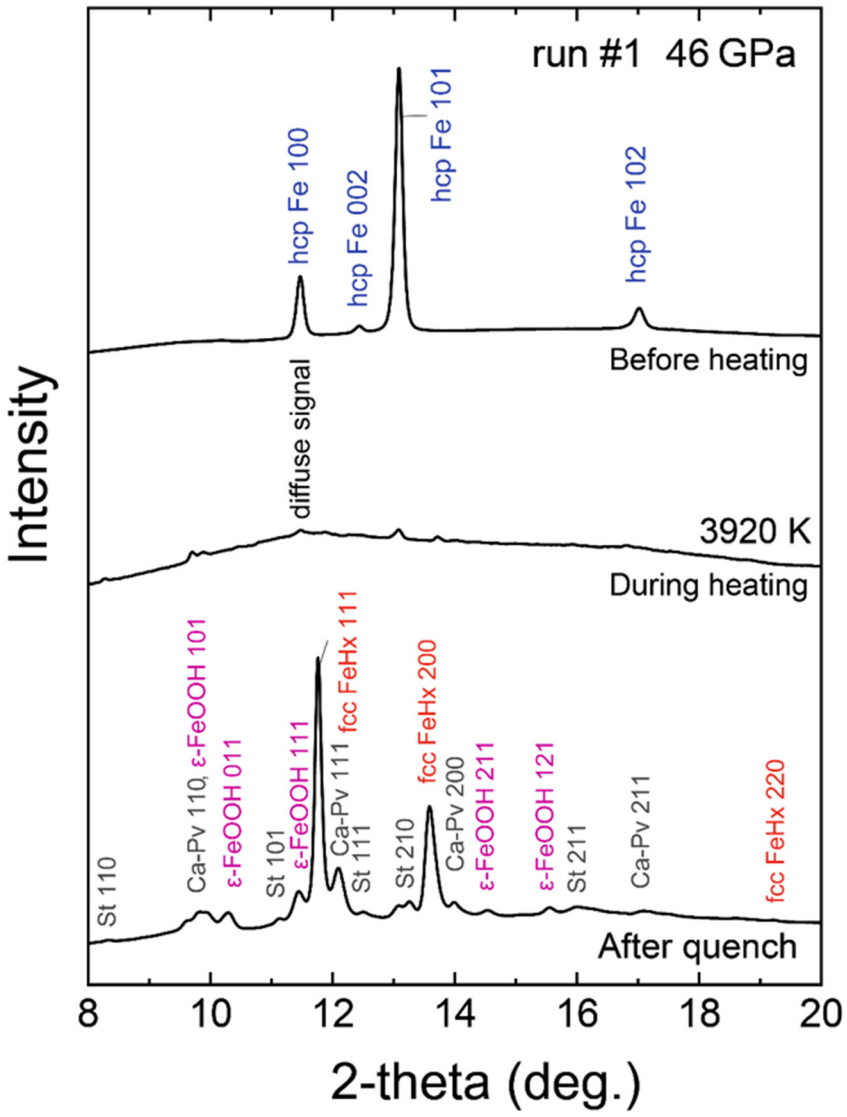

Figure 2.4 Analyses of hydrogen in metal

XRD patterns collected before/during/after heating to 3920 K at 46 GPa in run #1. Both iron and silicate were molten at the center of a laser-heated spot during heating. The hydrogen concentration in liquid metal was obtained from that in fcc FeH*x* based on its lattice volume and the proportions of FeH*x* and ε-FeOOH estimated from microprobe analyses. In this run, the incident X-ray beam was monochromatized to a wavelength of 0.41465 Å (~30 keV).

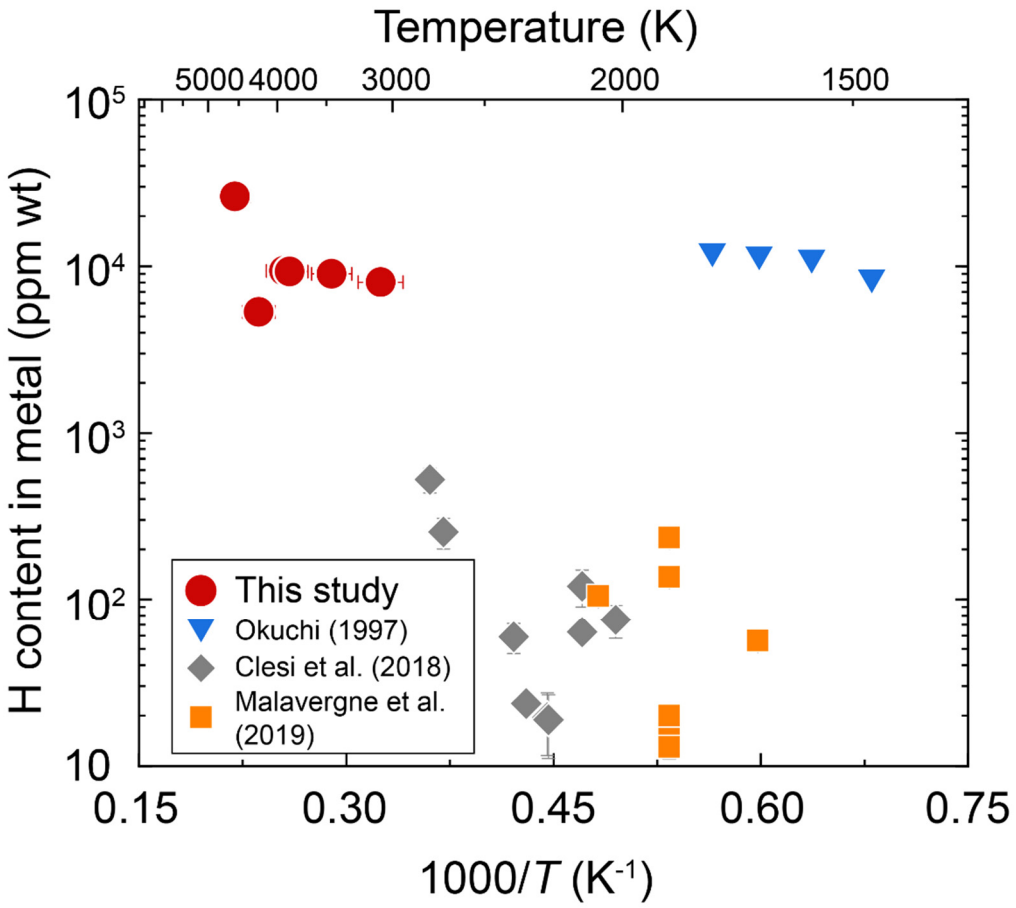

Figure 2.5 Hydrogen content in metal

Red circles, this study; blue triangles, (Okuchi, 1997); grey diamonds, (Clesi et al., 2018); orange squares, (Malavergne et al., 2019). Recent studies (Clesi et al., 2018; Malavergne et al., 2019) reported the hydrogen contents in metallic Fe lower by one to three orders of magnitude than the present results, because hydrogen was lost from metal during decompression in their experiments.

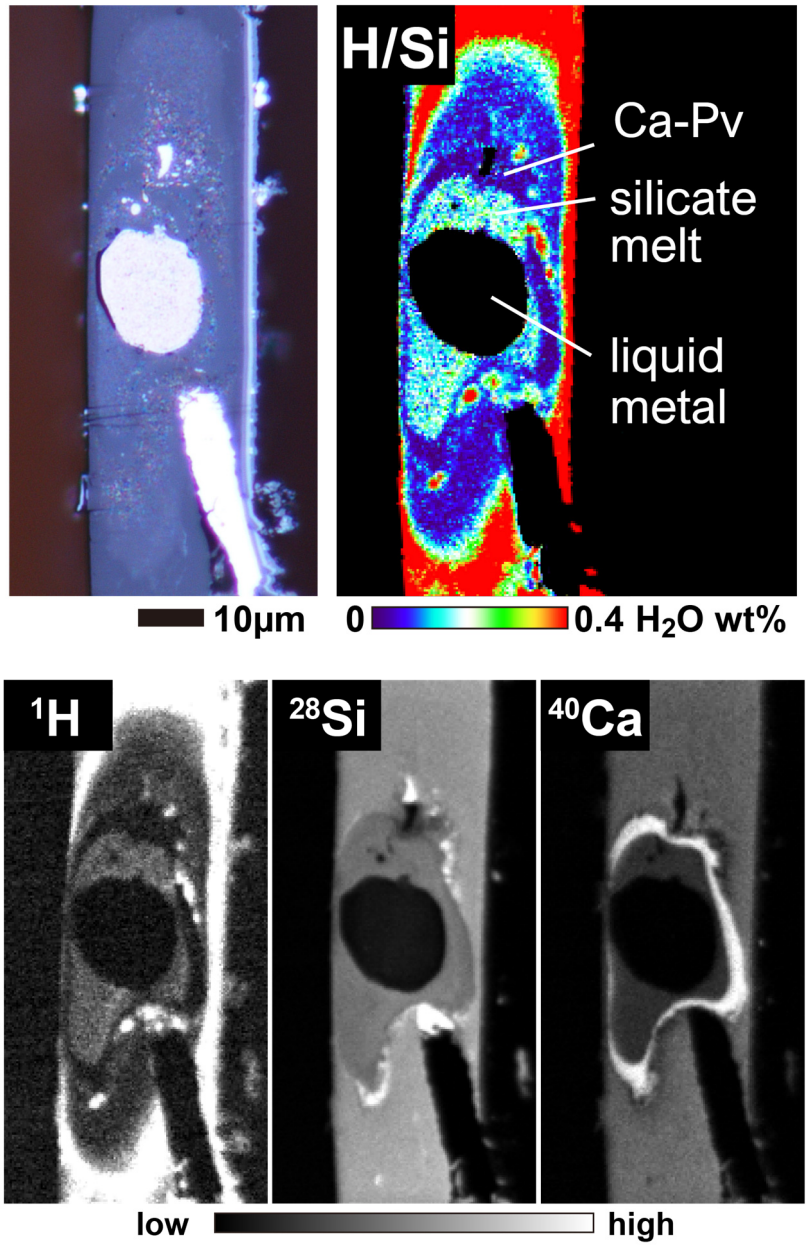

Figure 2.6 Analyses of hydrogen in silicate

Photomicrograph (top-left), secondary ion images for $^{1}H^{+}$, $^{28}Si^{+}$, $^{40}Ca^{+}$ (bottoms), and a distribution map of water (top-right). Note that the absence of hydrogen in metal, because it escapes from iron upon releasing pressure. The hydrogen (water) content in quenched silicate melt is obtained with ±2–7% relative uncertainty.

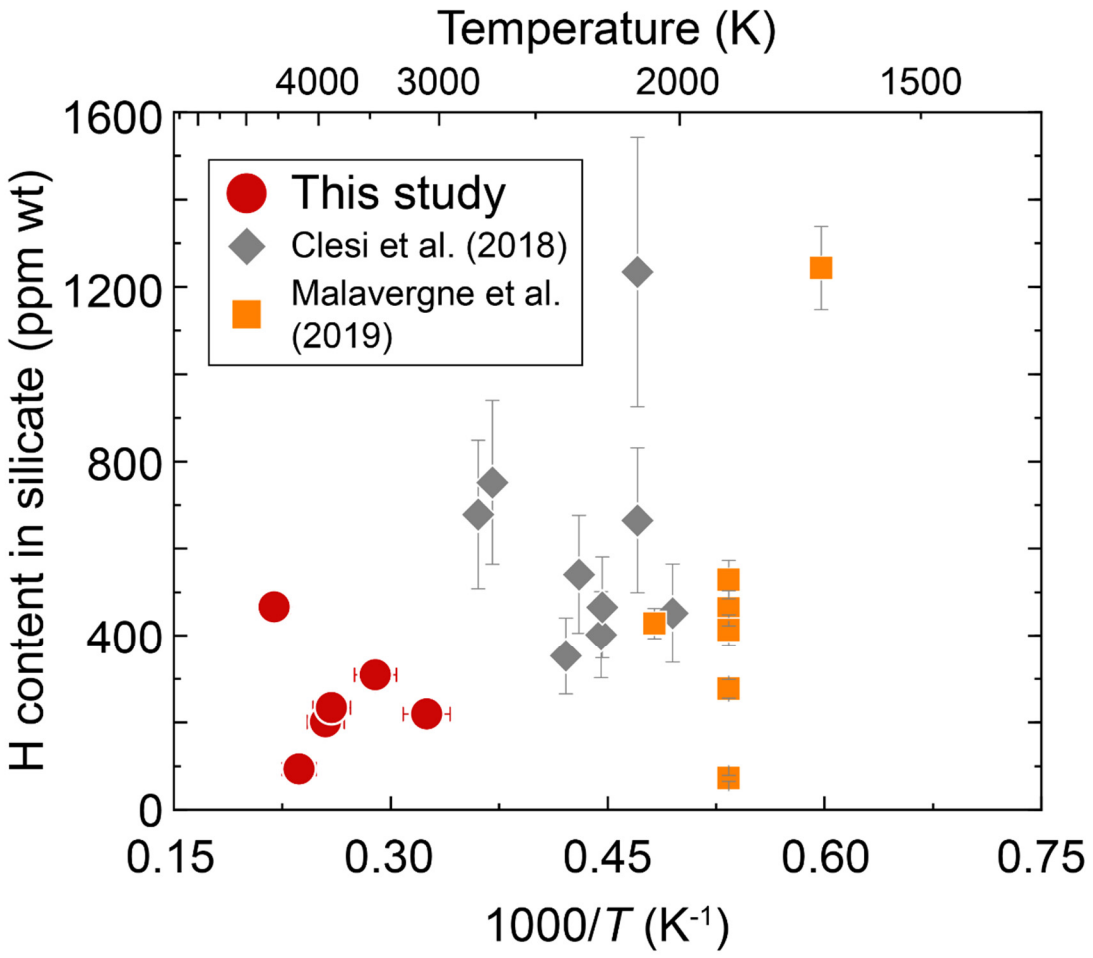

Figure 2.7 Hydrogen content in quenched silicate melt

The hydrogen contents in quenched silicate melts. Data from Okuchi (1997) are not shown because they include >6000 ppm H_2O. Symbols are the same as those in Figure 2.2.

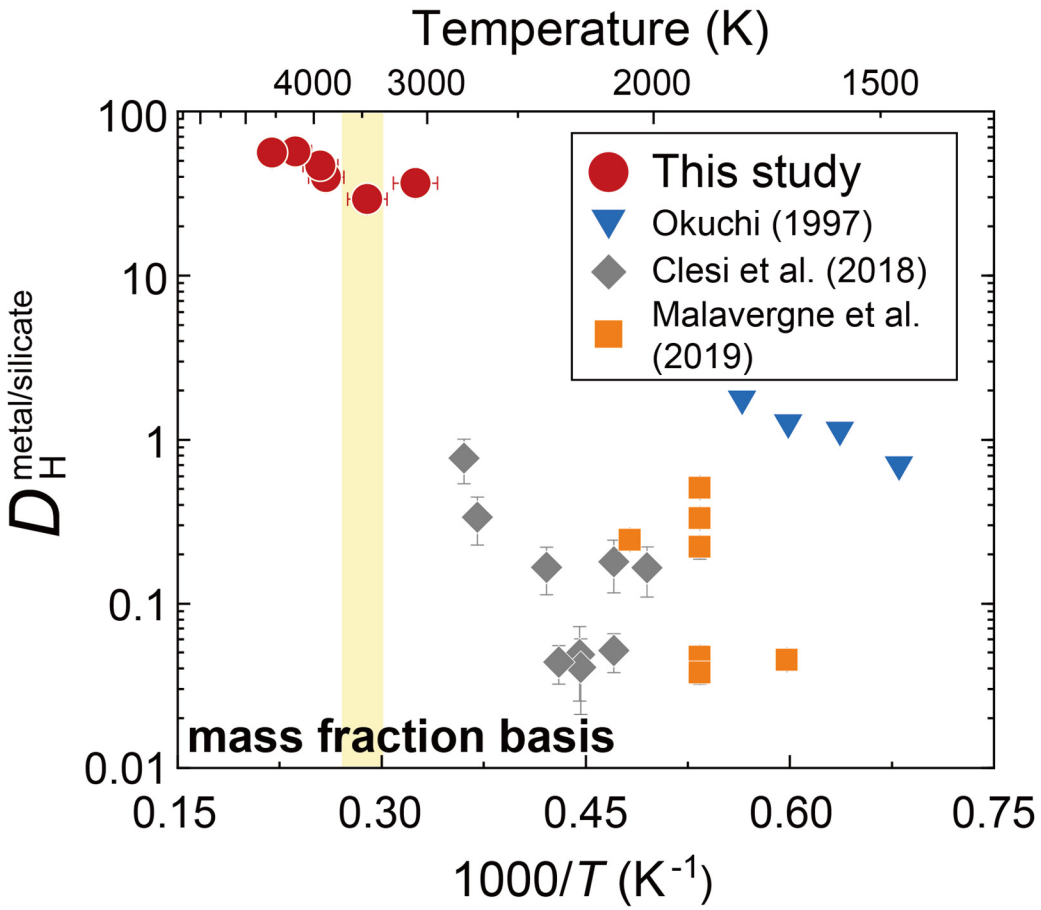

Figure 2.8 Parameterizing hydrogen metal–silicate partitioning coefficient

Partition coefficient *D* for hydrogen as a function of reciprocal temperature. The present work (red circles) shows that hydrogen is highly siderophile under conditions for Earth's core formation. Recent two studies (grey diamonds, Clesi et al. (2018); orange squares, Malavergne et al. (2019)) reported the *D* values lower by one to three orders of magnitude than the present results because hydrogen was lost from metals during decompression in their experiments. Pioneer experimental results (Okuchi, 1997) are also plotted. The yellow band shows the temperature ranges of core formation conditions.

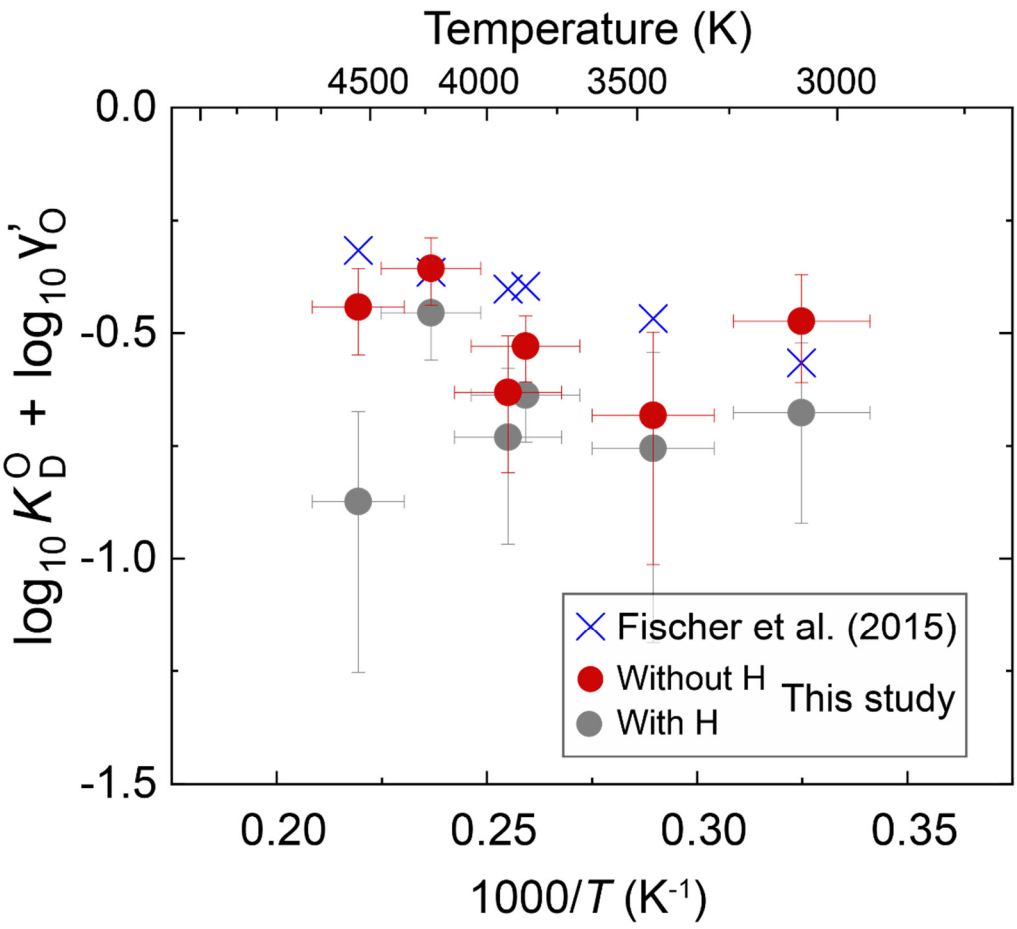

Figure 2.9 K_D^0 with (gray) and without (red) considering the presence of hydrogen for activity estimates

Present data (gray and red circles) are compared with earlier results (blue crosses) obtained in the H-free system (see section 4.2 in Fischer et al. (2015)).

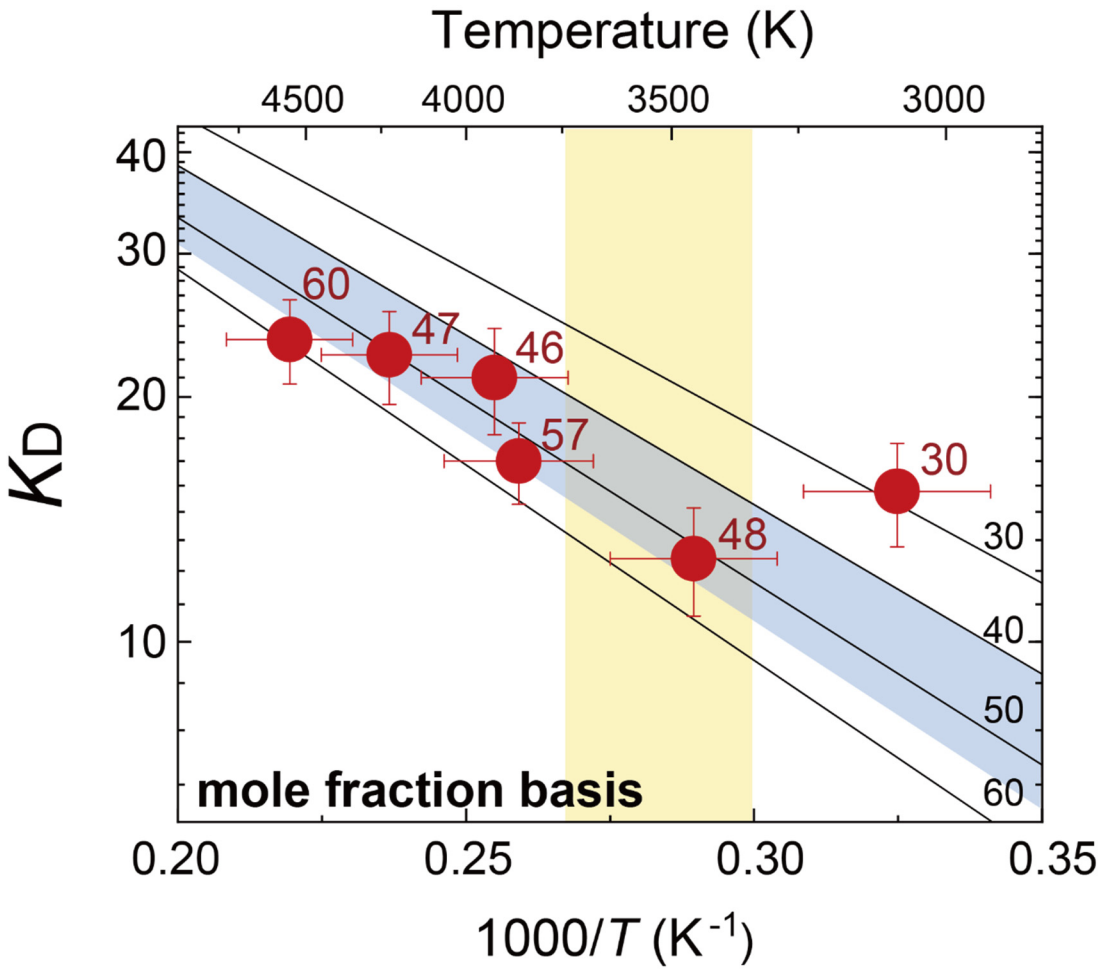

Figure 2.10 Metal-silicate partitioning coefficient of hydrogen

Exchange coefficient K_D for Eq. 2.4. The numbers given to each datum point and regression line indicate pressure conditions. Yellow and blue bands show the temperature and pressure ranges, respectively, for core-mantle chemical equilibration based on single-stage core formation models (Fischer et al., 2015; Siebert et al., 2012; Wade and Wood, 2005, Figure 1.5).

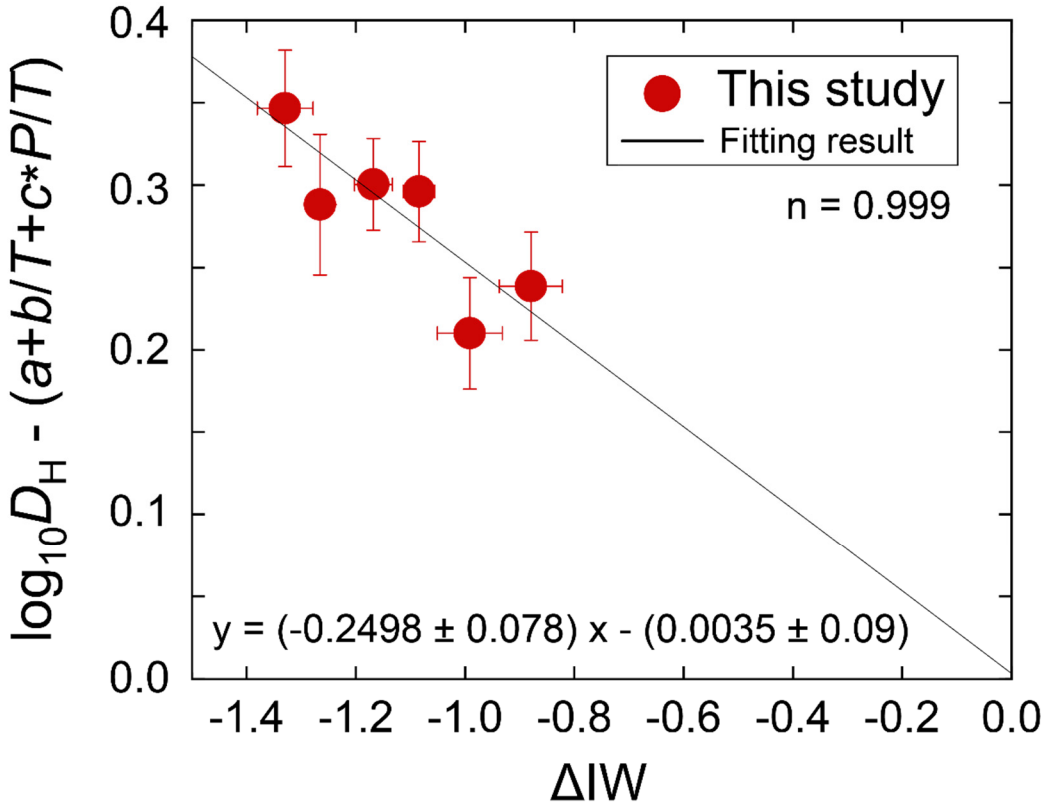

Figure 2.11 Partition coefficient *D* of hydrogen (molar basis) as a function of oxygen fugacity relative to the IW buffer

The difference in the experimental *P* and *T* conditions is corrected by the $a+b/T+c*P/T$ term. The slope of this plot indicates the valence state of hydrogen in silicate melt to be 0.999.

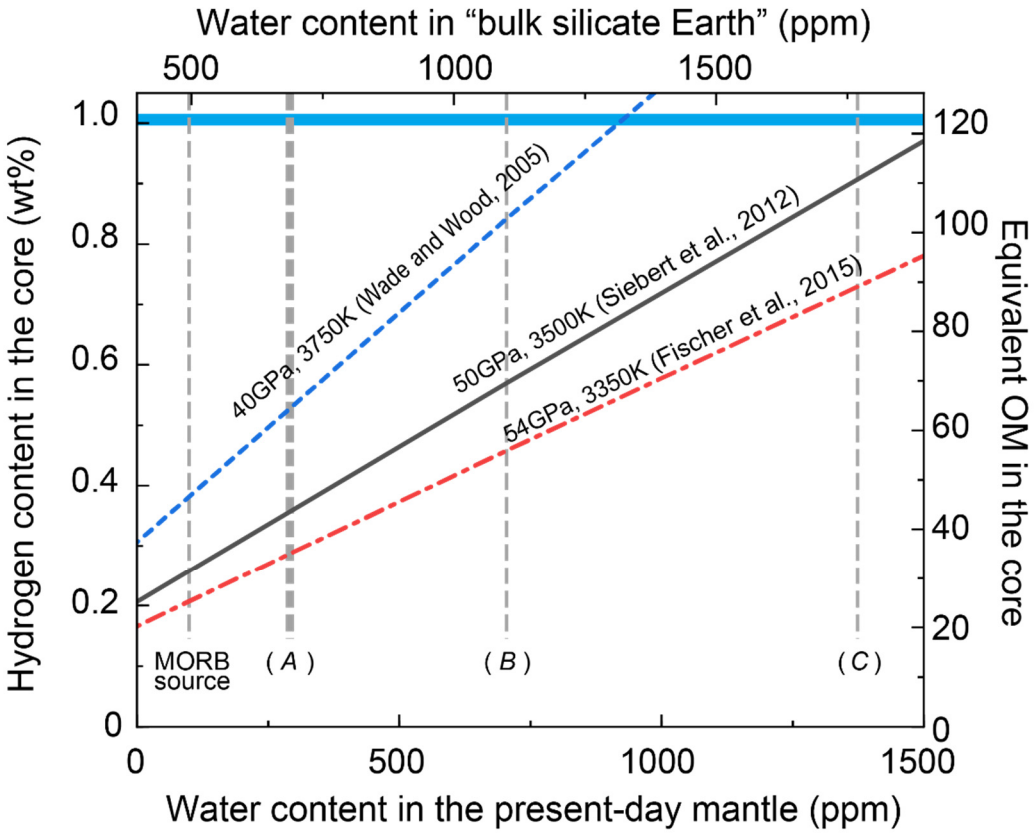

Figure 2.12 Estimate of hydrogen concentration in the core

Three lines show the hydrogen content in the core that is in chemical equilibrium with the “bulk silicate Earth (BSE)” (= present-day mantle + crust + ocean) at high *P*-*T* conditions as labeled (Fischer et al., 2015; Siebert et al., 2012; Wade and Wood, 2005). The BSE water content depends largely on the average mantle abundance (lower horizontal axis) (A, Hirschmann, 2016; B, Palme and O’Neill, 2014; C, Peslier et al., 2017). Even a modest amount of water in the present-day mantle (Hirschmann, 2016) suggests 0.29–0.53 wt.% H in the core, corresponding to 35–65 times hydrogen that exists in oceans (right vertical axis; OM, ocean mass), which accounts for ~30–50% of the density deficit and the velocity excess of the Earth’s outer core relative to pure iron.

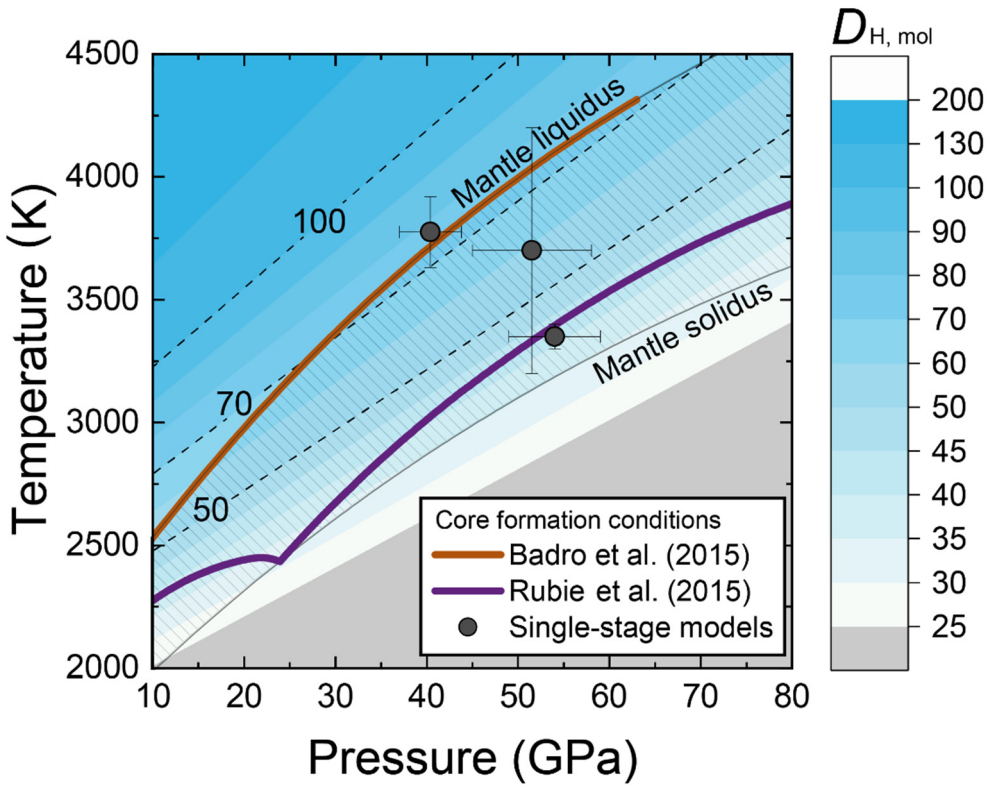

Figure 2.13 D_H values on the core formation conditions

The color (white to blue) indicates the D_H, defined in the molar ratio, $D_{H,mol} = x'_H/x_{H_2O}$, at the pressure and temperature at $\triangle IW = -2.3$. The core formation event is considered to usually occur at the conditions within the mantle liquidus and solidus temperatures (Andrault et al., 2011; Fiquet et al., 2010). The region is indicated by hatching. Pressure and temperature of the single-core formation models (Fischer et al., 2015; Siebert et al., 2012; Wade and Wood, 2005) are shown as black circles. Pressure and temperature pass in continuous- (Badro et al., 2015) and multi-stage (Rubie et al., 2015) core formation models are indicated in brown and purple curves, respectively.

Table 2.1 Summary of the metal-silicate partitioning experiments

Run #	#1	#2	#3	#4	#5	#6
Temperature (K)	3920 (200)	3450 (170)	3860 (190)	4560 (230)	4230 (210)	3080 (150)
Pressure (GPa)	46(5)	48(5)	57(6)	60(6)	47(5)	30(3)
H^{metal} (ppm wt.)	9390 (690)	9030 (690)	9280 (630)	26160 (1600)	5320 (380)	8020 (640)
$H^{silicate}$ (ppm wt.)	201(3)	309(5)	233(5)	466(9)	94(6)	219(4)
D^H (in wt.)	47(4)	29(2)	40(3)	56(4)	57(6)	37(3)
fO_2 (ΔIW)	-0.88	-0.99	-1.08	-1.17	-1.27	-1.33
Structure of FeH*x*	*fcc*	*fcc*	*fcc*	*hcp*	*fcc*	*fcc*
Hydrogen content *x*	0.52	0.52	0.52	1.78	0.23	0.43
ε-FeOOH ratio*	0.19	0.15	0.18	0.06	0.13	0.07
Area of ROI in SIMS analysis (μm^2)	120	160	80	110	60	80
$\log_{10}K_D^H$	1.32(6)	1.10(6)	1.22(5)	1.37(5)	1.35(6)	1.18(6)

Numbers in parentheses indicate one standard deviation in the last digits.

*The molar ratio of ε-FeOOH defined as $\frac{x_{\varepsilon-\mathrm{FeOOH}}}{x_{\varepsilon-\mathrm{FeOOH}}+x_{\mathrm{FeH}_x}}$

Table 2.2 Chemical compositions (wt.%) of stating material and silicate melt

	SM*	run #1	run #2	run #3	run #4	run #5	run #6
N†	28	8	8	8	8	8	8
SiO_2	49.64	36.14 (123)	38.54 (126)	32.67 (65)	37.59 (99)	34.26 (98)	40.17 (57)
TiO_2	1.64	1.73 (14)	1.89 (9)	3.08 (14)	1.73 (7)	1.96 (16)	2.49 (12)
Al_2O_3	14.88	14.78 (81)	13.96 (43)	19.34 (77)	18.71 (48)	18.63 (103)	11.32 (80)
FeO	11.43	29.43 (193)	26.10 (175)	24.47 (79)	22.89 (89)	21.01 (42)	23.27 (136)
MgO	8.51	9.33 (35)	9.31 (16)	11.03 (29)	11.34 (23)	11.82 (81)	8.91 (57)
CaO	10.55	4.15 (46)	4.60 (13)	4.53 (40)	4.06 (22)	5.02 (72)	8.40 (57)
Na_2O	2.90	3.24 (22)	2.82 (19)	3.68 (20)	2.35 (39)	3.66 (40)	3.80 (23)
K_2O	0.12	0.25 (1)	0.25 (4)	0.32 (3)	0.26 (4)	0.43 (6)	0.32 (3)
Total	99.67	99.05 (120)	97.48 (100)	99.11 (96)	99.28 (79)	96.8 (263)	98.67 (74)

Numbers in parentheses are one standard deviation in the last digits.

*About 0.2 and 1.0 wt.% H_2O was added.

†Number of analyses

Table 2.3 Chemical compositions (wt.%) of quenched liquid metals

	run #1	run #2	run #3	run #4	run #5	run #6
N*	8	-	8	8	8	8
Fe	85.00 (83)	85.6 (11)	85.03 (54)	83.55 (84)	85.24 (188)	92.54 (55)
Si	2.27 (20)	3.2 (3)	2.16 (15)	4.73 (64)	1.52 (20)	0.52 (10)
O	12.14 (50)	11.2 (10)	11.33 (42)	8.70 (58)	8.92 (61)	4.48 (40)
Al	0.20 (2)	N.D. -	0.21 (3)	0.31 (1)	0.43 (21)	0.01 (1)
Mg	0.08 (3)	N.D. -	0.09 (1)	0.10 (1)	0.22 (18)	0.01 (1)
Total	99.70 (85)	100	98.82 (86)	97.39 (118)	96.34 (102)	97.56 (53)

Obtained with EDS for run #2 and with EPMA for other runs

Numbers in parentheses are one standard deviation in the last digits.

*Number of analyses

Chapter 3. Phase relations of FeH*x* at high pressures

This chapter has been prepared as a manuscript named in *"Phase relations in non-stoichiometric FeHx at high pressures"* by ***Shoh Tagawa****, Kenji Ohta, Kei Hirose, and Yasuo Ohishi.*

Abstract

In Chapter 3, I will report the phase relations of the Fe-FeH binary system up to 173 GPa and 4020 K using an LH-DAC. Despite its importance, the phase diagram of Fe-FeH at over 20 GPa is still an open question. The concentration of hydrogen was denoted as a molar ratio of H/Fe, which is the definition of "*x*." I combined three cell assemblies: a sub-stoichiometric (x<1) experiment, a stoichiometric experiment (x=1), and an experiment in which hydrogen diffused in a Fe-H sample. I performed high-pressure and -temperature experiments for 11 runs. Then, I determined the melting temperatures of stoichiometric FeH and sub-stoichiometric FeH*x,* and the stability field of each crystal structure. I found that the Fe-FeH system has a eutectic-type phase diagram, and the eutectic temperature would be sufficiently low to explain the low CMB temperature inferred from the solidus of pyrolite, although end-member *fcc* FeH had a high melting temperature. The miscibility gap of hydrogen contents between the subsolidus phases exists at $0.44 < x < 0.69$, and it implies that *hcp* FeH*x* is feasible as the inner core crystal structure if hydrogen is the dominant light element. Features of the phase diagram of the Fe-FeH system do not rule out the Earth's core hydrogen bearing up to $x \sim 0.6$ (1.07 wt.% H).

3.1 Introduction

Since the 1950s, significant effort has been spent to develop the phase diagram of iron and its alloys to understand the composition and physical properties of the Earth's core (e.g., Li & Fei, 2014). Recent technical improvement, especially combining LH-DAC techniques, synchrotron XRD measurements, and FIB milling processing enables us to perform experiments at the conditions of Earth's core. The maximum pressures in experimental studies have thus expanded—for example, 254 GPa for the Fe-S system (Mori et al., 2017); 127 GPa for Fe-Si (Ozawa et al., 2016); 255 GPa for Fe-C (Mashino et al., 2019); and 204 GPa for Fe-O (Oka et al., 2019). The phase diagram is key for constraining not only the crystal structure solidified in the inner core but also the maximum content of each light element due to the eutectic composition.

There are a few previous studies on the Fe-FeH binary system above ~20 GPa and high temperatures. Even the stable crystal structures of FeH*x* are controversial. So far, three FeH*x* structures ($x \leq 1$) have been reported: double hexagonal closed-packed (*dhcp*), face center cubic (*fcc*), and hexagonal closed-packed (*hcp*) (Machida et al., 2019; Yamakata et al., 1992) (Figure 3.1). The most common reported structure, *dhcp*, is formed at room temperature above 3.5 GPa (Badding et al., 1991) and preserved up to at least 136 GPa (Pépin et al., 2014) in compression without laser heating. On the other hand, *fcc* appeared in high-temperature conditions. The temperature of the phase transition from *dhcp* to *fcc* is ~700 K at 4–7 GPa (Saitoh et al., 2017),

and at 1073 K at 20 GPa (Sakamaki et al., 2009). This *fcc* FeH*x* was likely to be reported with synthesis at high temperatures (Hirose et al., 2019; Kato et al., 2020; Narygina et al., 2011; Ohta et al., 2018; Thompson et al., 2018). Note that the effect by paraffin used as a hydrogen source is minor because the carbon content in the *fcc* FeH*x* is substantially small (Hirose et al., 2019).

Hcp FeH*x* could be the essential phase because it is likely to have $x<0.5$ (lower than 0.9 wt.%) within the maximum composition range of hydrogen in the core. However, the stability field of *hcp* FeH*x* is still an open question because the reported conditions of its appearing are a few. Antonov et al. (1998) first determined the structure of non-magnetic *hcp* $FeD_{0.42\pm0.04}$ by using neutron diffraction measurements at 1 bar and 90 K. After then, the formation of *hcp* FeH*x* was directly observed by *in situ* XRD measurement at high pressures and high temperatures. Yamakata et al. (1992) reported the formation of *hcp* FeH*x* ($x < 1$) from body-centered-cubic (*bcc*) Fe around 675 K and 6 GPa, and Machida et al. (2019) observed phase transition from fcc $FeH_{0.6}$ to hcp $FeH_{0.5}$ at around 6 GPa and 800 K. Besides, Gomi et al. (2018) conducted *ab initio* calculations for sub-stoichiometric *hcp* and *dhcp* FeH*x* and found that nonmagnetic *hcp* is stable at over 25 GPa and $x < 0.55$. Note that Isaev et al. (2007) suggested that stoichiometric *hcp* FeH would be stable at lower temperatures (~0 K), where the harmonic vibrational effect is minor, but such stoichiometric *hcp* would be less important because it would be metastable in the temperature region of interest.

Magnetic properties of FeH*x* are one of the reasons why the phase relation of FeH*x* is complicated. With high *x* and/or under lower pressures, where FeH*x* has a larger volume, and at temperatures lower than the Curie temperature, FeH*x* likely has a magnetic moment. Phase transitions of FeH*x* would take place in association with the changing of magnetic properties from ferromagnetic (FM) to nonmagnetic (NM) or paramagnetic (PM). *Ab initio* calculations indicated the effect of magnetic properties on a stable structure of FeH*x*. Isaev et al. (2007) suggested that the phase transition of stoichiometric FeH will occur as a FM *dhcp* → (37 GPa) → *hcp* → (83 GPa) → PM *fcc* sequence of structural transitions. Elsässer et al. (1998), Kato et al. (2020), and Tsumuraya et al. (2012) also concluded that *fcc* and *dhcp* lose their magnetic moment at the volume lower than 10 – 10.5 $Å^3$ per formula unit (~ 60 GPa). However, Mitsui and Hirao (2010), and Narygina et al. (2011) carried out *in situ* Mössbauer measurements to determine the magnetic property of FeH*x* experimentally, and both of them found that the ferromagnetic 6-line pattern rapidly collapsed at around 26–27 GPa. Ying et al., (2020) also confirmed the hyperfine magnetic field of *dhcp* FeH drops drastically above 26 GPa at 300 K. This discrepancy makes it more challenging to discuss the stable phase of stoichiometric FeH.

The melting temperature of FeH*x* has also collected interest mainly because of the lower melting temperature of the lowermost mantle. Nomura et al. (2014) determined the solidus temperature of the pyrolytic lowermost mantle as 3570±200 K. This implies that the material of

the outer core should have a considerably lower melting temperature. Sakamaki et al., (2009) constructed the melting phase relation of FeH*x* up to 20 GPa and 1585 K using a multi-anvil apparatus. This research predicted that the melting temperature of FeH is ~2600 K at the core-mantle boundary (CMB) and hydrogen would significantly lower the melting curve. Recently, Hirose et al. (2019) reported the melting temperature of FeH$x\geq1$, which is comparably low to the melting curve by Sakamaki et al. (2009), although the hydrogen content was superstoichiometric.

Why are there so few experiments on the FeH*x* system by using an LH-DAC? Firstly, hydrogen quickly intrudes into diamond anvils during heating and cracks them. Secondly, hydrogen tends to move from the sample chamber to the rhenium gasket at over 25 GPa. Therefore, installing a hydrogen sealant into the sample chamber or contriving a hydrogenation P-T path is necessary. Thirdly, hydrogen escapes from iron after the sample is recovered in ambient conditions; therefore, no chemical analysis using an electron microprobe is possible.

Here, I performed high pressure and high-temperature experiments using an LH-DAC with newly devised experimental techniques and then investigated the melting temperatures of FeH*x* and the stability field of each crystal structure up to 173 GPa. Based on these results, I will discuss the phase diagram of the Fe-FeH system and the feasible structure of FeH*x* in a solid core condition. The result shows that the phase diagram of the Fe-FeH system is not contradictory to the hydrogen bearing core hypothesis within the pressure range I examined.

3.2 Experimental Method

High-pressure and -temperature conditions were generated in an LH-DAC with 120, 150, 200, and 300 μm culet size. The anvils were single-beveled even for 300 μm culet size anvils in order to avoid the anvil failure. Note that flat anvils easily broke at over 50 GPa if the sample contains hydrogen molecules. Sample configurations are shown in Figure 3.2. The starting material is 10 μm thick pure iron foil (5N, Mairon-UHP, *Toho Zinc*). I set up the cell in three types of sample assemblies: (a) non-stoichiometric FeH experiments, (b) stoichiometric FeH experiments, and (c) an experiment in which hydrogen was diffused in a Fe-H sample. The difference between these was the existence of an inner gasket and the kind of pressure mediums. Setting (a) had no sealing material for hydrogen; a 10–15 μm thick disk of corundum (Al_2O_3) single crystals was loaded on both sides of the iron foil. Rhenium gaskets were pre-indented to about 45 μm thickness before making a sample chamber with 1/3–4/9 diameters using the anvils' culet size. Single crystal corundum served not only as an internal pressure standard but also as the thermal insulator from diamond anvils. I placed a small block of NaCl / ruby ball, on the edge of the sample chamber in order to adjust the laser-heating position precisely.

Setting b) had an NaCl inner gasket along the entire edge of the sample room. The wall thickness of the inner gasket is typically 10 μm and was formed using a focused ion beam with the FE-SEM system (FIB, Versa 3D, FEI, USA). NaCl is considered to be a suitable hydrogen

sealant (*e.g.* Sakamaki et al., 2009; Ohta et al., 2015). Rhenium gaskets were pre-indented to about 20–30 μm thickness. Thin NaCl pellets were loaded as a pressure medium, and ruby balls were added in run S1. Setting (c) was the same as (a), but with an NaCl inner gasket.

After the sample was loaded, the DAC was dried in a vacuum oven at 400 K (~8×10^3 Pa) for at least one hour just before loading the hydrogen. Then, it was dried again at 350 K for 30 mins in the hydrogen loading system with a vacuum (10 ~ 1Pa, lower than the limit of the gauge) in order to avoid contamination by water. The DAC was not exposed to the atmosphere until the hydrogen loading has completed.

Hydrogen was loaded into the sample chamber using a "liquid hydrogen loading system" installed in TokyoTech (Chi et al., 2011). I used G1-grade H_2 gas with a small amount of G2-grade He. He gas was used as a heat transfer at the temperatures lower than the melting point of hydrogen (20 K). The sample was compressed at ~ 15 K after the sample room was filled with liquid hydrogen and then restored to room temperature. Note that the surface of the diamond anvils was coated with a thin layer of Ti by sputtering (Ohta et al., 2015) in order to avoid the anvil failure. After FeH*x* was synthesized, the excess molecular hydrogen in the sample chamber was released. For setting (a), after the sample was compressed to over 23 GPa, molecular hydrogen escaped to the Re gasket because of ReH*x* formation (Scheler et al., 2011). For setting (b), I released the pressure on the DAC sample to 1 bar at 95 K. Because $FeH_{0.42<x<1}$ does not

decompose at the condition and hydrogen in the iron lattice were preserved for several hours (Antonov et al., 1998), only the excess hydrogen molecules can be released from the sample chamber. The sample was pressurized again to over 5 GPa at 95 K and finally restored to the room temperature. Photographs of the sample chamber are shown in Figure 3.2.

Angle-dispersive XRD patterns were collected at BL10XU, SPring-8 (Ohishi et al., 2008). The incident X-ray beam was monochromatized to ~30 keV and collimated to ~6 μm (FWHM). Flat-panel CMOS detector (*PerkinElmer*) was used for real-time phase determination and data collection. Each diffraction pattern was analyzed by a software suite (Seto et al., 2010). Heating was done from both sides with two 100 W single-mode Yb fiber lasers (*SPI photonics*). The lasers were focused on a spot 35–45 μm across. A one-dimensional radial temperature profile was collected by a spectro-radiometric method (Ohishi et al., 2008). The experimental temperature was represented by the maximum of the one-dimensional profile and its uncertainty is ±5% (Mori et al., 2017). For run U4, the melting temperature was constrained by combining the cross section image of heating spots and its 1-D temperature profile. Its melting temperature was represented by the temperature of the boundary of solid FeH*x* and the molten region in the high temperatures.

The pressure at room temperature was obtained based on the equation of state (EoS) of Al_2O_3 (Dewaele and Torrent, 2013) or B1-/B2-NaCl (Dorogokupets and Dewaele, 2007), which EoSs is consistent with that of pure Fe (Dewaele et al., 2006; Dorogokupets et al., 2017). The

data obtained at lower than 10 GPa and room temperature compression in run U6 were determined based on the Raman shift of a diamond (Akahama and Kawamura, 2004). Samples were annealed before each XRD data was collected to reduce the stress (except for the cold compression in run U6 and the diffusion experiment in run D). The EoS of post-perovskite Al_2O_3 (Caracas and Cohen, 2005) was used for the data over 135 GPa in run M1 because corundum changed to this phase. The contribution of thermal pressure was corrected by adding a 5% pressure increase per 1000 K (Fiquet et al., 2010), and its uncertainty should be within ±10% (Mori et al., 2017).

For phase determination at high temperatures in runs U1–U4 and D, the samples were kept laser-heated typically for 30 seconds to 40 minutes. In melting experiments for runs M1–M3 and S1–S3, the heating duration was typically 3–20 seconds. The samples were then quenched immediately from the highest temperature to ambient temperature. In this work, "annealing" means laser-heating of samples below 1300 K, in order to release the stress of the sample for pressure measurement and adjusting hydrogen concentration. This process typically lasts several minutes.

Note that the kinetics of the phase transition could affect the observed phase in XRD. For example, in run S1, I observed *hcp* $FeHx_{\sim 1}$ just after the sample was synthesized, but I never observed that stoichiometric *dhcp* or *fcc* FeH exhibits a phase transition to stoichiometric *hcp* FeH in this work. At lower temperature conditions, hydrogen is likely to dissolve into *hcp* iron

for a substantial amount; however, it would not mean such *hc*p FeH*x* is thermodynamically stable at the temperature, pressure and hydrogen content. Therefore, in this study, I defined the phase that appears after phase transitions, after laser heating to >2000 K, or after keeping samples for several days at room temperature, as a "stable" phase at each condition.

As a melting criterion, the formation of a quenched crystal during the fast thermally quenching (Mashino et al., 2019) or reduction of the intensity of XRD peaks to 1/4 at the highest temperature (Kusakabe et al., 2019) was adopted. In the runs in which I thermally quenched the sample rapidly, the first criteria are valid, but this criterion only yields the upper bound of the melting temperature. On the other hand, in run U1, I can apply the second criterion, probably because the sample became thinner in high pressures. If neither of these criteria is confirmed, it gives a lower bound of melting temperature. Note that the quench crystals have a different hydrogen content to the subsolidus phase, and it should be the same as that of the liquid pool in high temperatures (Hirose et al., 2019).

In runs U1 and U4, textural characterization was performed to confirm the melting. A cross section of the heating spot of the recovered sample was obtained by milling with FIB. The cross section was analyzed by a Ga-ion beam secondary electron mode image (SIM), which is reflected in a trend toward a bulk crystallographic orientation (Phaneuf, 1999). The SIM image was obtained with an accelerating voltage of 30 kV and a 10–30 pA ion current.

3.3 Results

(1) Design of experiments

In this work, a total of 11 separate runs (U1–U4, D, M1–M3, and S1–S3) were carried out. The cell configuration, the maximum pressure, and the maximum temperature are available in Table 3.1. The following six types of experiments were performed, and all of the results were combined to build the Fe-FeH phase diagram. The correspondence between the experiments and the points on the phase diagram is shown in Figure 3.3. Table 3.2–3.4 depicts the experimental conditions and run numbers.

Experiment A) Compression/decompression experiments of stoichiometric FeH. This experiment determines ΔV_H, the volume increase per hydrogen atom, and will enable us to estimate hydrogen content.

Experiment B) Laser heating experiments to confirm the miscibility gap between the *hcp* and *fcc* phase. I plotted the stable phase obtained at each condition.

Experiment C) A room-temperature experiment in which hydrogen diffused in a sample. This part aimed to check the existence of the miscibility gap at room temperature.

Experiment D) Compression/heating experiment to confirm the narrow stability field of *dhcp*.

Experiment E) Melting experiments on stoichiometric FeH.

Experiment F) Melting experiments on sub-stoichiometric FeH*x*.

(2) Construction of the method to calculate the hydrogen content (Experiment A)

In run S1 and S2, I performed the compression and decompression experiments for stoichiometric FeH up to 138 GPa. Note that both runs show almost the same volume as that of the stoichiometric FeH reported in previous studies at 60 GPa. Before the compression started, stoichiometric *hcp* FeH was found in both runs. The difference is ascribed to hydrogenation temperatures; hydrogenation occurred in low temperatures at which *hcp* FeH should be stable (Isaev et al., 2007). However, this stoichiometric *hcp* FeH seems to be metastable above room temperature. Its XRD patterns gradually broadened with pressure increase and changed to *dhcp* (S1) or *fcc* (S2) after heating. For run S1, the compression behavior of *dhcp* was obtained up to 53 GPa. Both samples were heated to over 1500 K around 55 GPa and subsequently changed to *fcc* FeH. Decompression and compression are continued in run S3 and in run S2, respectively. Note that all volume data were collected after the sample was annealed.

Compression data are summarized in Table 3.2 and Figure 3.3. I found that both the *dhcp* and *fcc* compression curves in this study well reproduced the results by Pépin et al. (2014) and Kato et al. (2020), respectively. However, results from other previous studies deviated from them at over 70 GPa. The volume difference of *dhcp* and *fcc* in lower than 40 GPa would originate from the magnetic moment or its ordering. However, the volume difference of the EoS disappeared above that pressure. An anomaly of compressibility may exist around 50 to 60 GPa

(Meier et al., 2019), but I could not draw concrete evidence.

The hydrogen concentration *x* is empirically obtained by the formula (Fukai, 1992);

$$x = (V_{\mathrm{FeH}_x} - V_{\mathrm{Fe}}) / \Delta V_{\mathrm{H}} \quad \text{(eq. 3.1)}$$

where V_{FeH_x} is the volume of FeH*x* per formula, V_{Fe} is the atomic volume of pure iron, and ΔV_{H} is the partial volume of hydrogen in FeH*x*. The validity of this formula was confirmed in Machida et al. (2014) for *fcc* FeD*x* by neutron diffraction. The recent study by Ikuta et al. (2019) also reported the linearity between the term of $V_{\mathrm{FeH}_x} - V_{\mathrm{Fe}}$, and x. However, the pressure dependence of ΔV_{H} is controversial. Previous studies typically fixed the value between 1.8–2.6 $\mathrm{Å}^3$ (Thompson et al., 2018) or utilized a theoretical EoS of metallic hydrogen (Fukai, 1992 after Chakravarty et al., 1981). Recently, a series of computational EoS of *hcp* FeH*x* (*x*=0, 0.125, 0.25, 0.50, 1.00) was proposed which provides an alternative ΔV_{H} (Caracas, 2015).

I calculated the $V_{\mathrm{FeH}} - V_{\mathrm{Fe}}$ for the data from run S1 and S2 with the EoS of pure iron (Dorogokupets et al., 2017). The results are shown in Figure 3.4. In the run S1 and S2, *x* should be 1. So, $V_{\mathrm{FeH}} - V_{\mathrm{Fe}}$ is equal to ΔV_{H}. $V_{\mathrm{FeH}} - V_{\mathrm{Fe}}$ is well reconciled with the ΔV_{H} by Caracas (2015) above 40 GPa, while *dhcp* FeH (P < 40 GPa) expanded more than *fcc* FeH due to ferromagnetism. The volume expansivity of ferromagnetic FeH was reported in theoretical (Gomi et al., 2018; Isaev et al., 2007; Tsumuraya et al., 2012) and experimental (Hirao et al., 2004; Kato et al., 2020) studies.

(3) The miscibility gap of Fe-FeH binary system (Experiments B and C)

Hydrogen contents of FeH*x* were calculated with eq. 3.1. Pressure and temperature conditions are listed in Table 3.4. In this study, I adopted the ΔV_H by Caracas (2015) for *fcc* and *hcp*. As a referential volume, I used the P-V-T EoS of *hcp* and *fcc* Fe (Dorogokupets et al., 2017). Note that data were collected in pressure, temperature, and composition range, where *hcp* and *fcc* FeH*x* are not ferromagnetic (Gomi et al., 2018; Narygina et al., 2011; Thompson et al., 2018). So, the expansion by the ferromagnetism should be negligible. On the other hand, hydrogen contents in ferromagnetic *dhcp* FeH are estimated from the volume difference between V_{FeH} (Pépin et al., 2014) and V_{Fe} (Dewaele et al., 2006). The temperature dependence ΔV_H is ignored because the recent neutron diffraction study revealed it to be small (Ikuta et al., 2019). This assumption yields x~1 in high temperatures for stoichiometric FeH in run S1 and S3, which supports its validity. The error of x was taken as ±6%, which reflected the uncertainty of pressure and potential error using eq. 3.1 to estimate x (Ikuta et al., 2019).

The summary of the hydrogen contents is shown in Table 3.3 and Figure 3.6. All of the XRD data were collected after annealing the sample sufficiently or 50 days after the hydrogen diffusion (see below). The data containing a metastable crystal (*e.g.,* quenched crystals after melting experiments) are eliminated from the table, except for the gray hatched lines in run M3. A miscibility gap between *hcp* (x=0.44) and *fcc* (x=0.69) exists even at high pressures.

In order to confirm the existence of the miscibility gap, I performed a room-temperature experiment in which hydrogen diffused in a Fe-FeH sample in fifty days at 46 (5) GPa. The sample configuration (C) has a gradient of hydrogen in the sample chamber. At first, after weak thermal annealing, the distribution of *x* along the sample room was collected (Figure 3.7.A). Then, the sample was kept for fifty days at room temperature during which hydrogen redistributed. I obtained the distribution map of hydrogen contents again without annealing (Figure 3.7.B).

The distribution of hydrogen changed significantly during the period. The XRD profiles of the initial condition show that some parts of the sample didn't have a highly ordered arrangement of atoms (gray areas in Figure 3.7.C). This is probably because FeH*x* at these parts would contain a large amount of lattice defect. The bulk hydrogen contents there would be within the range of the miscibility gap. On the other hand, 50 days after, the phase separation to *hcp* and *fcc* FeH*x* were confirmed due to the redistribution of hydrogen. At that time, the maximum hydrogen contents in *hcp* FeH*x* and the minimum in *fcc* FeH*x* were 0.36 and 0.76, respectively. It indicated the width of the miscibility gap at 46±5 GPa and room temperature.

The coexistence of *hcp* and *fcc* was also observed at high temperatures. One of the typical sequences of XRD patterns during heating is shown in Figure 3.8. Note that the hydrogen contents of *hcp* FeH*x* were slightly dispersed during the laser heating for long (run U2–U4). This happens because hydrogen in *hcp* FeH*x* is quickly diffused away from the observing area by XRD.

(4) The stability field of *dhcp* FeH*x* (Experiment E)

I confirmed that the stability field of *dhcp* FeH*x* is smaller than previously thought. To do this, I used room temperature compression experiments with hydrogen contents decreasing (Figure 3.9) and heating experiments for stoichiometric FeH (Figure 3.10). Both data indicate that *dhcp* transitioned to *fcc* FeH*x*. Note that the condition of the data obtained is above the pressure where the hyperfine field breaks down (Mitsui and Hirao, 2010). *Fcc* FeH*x* was repeatedly synthesized above 1500 K, and 35–70 GPa (Hirose et al., 2019; Kato et al., 2020; Narygina et al., 2011; Ohta et al., 2018; Thompson et al., 2018). This supports the instability of *dhcp* FeH*x*. The *dhcp* stability field would be limited to a lower-pressures (<~60 GPa) and -temperature range (<~2000 K) ; at the least it can not exist in the core pressure and temperature conditions.

(5) Melting experiment for stoichiometric FeH*x* (Experiment F)

I performed melting experiments of stoichiometric FeH*x* up to 163 GPa and 4020 K (S1–S3). I repeated a sequence of laser heating and rapid quenching until the intensity of XRD peaks were reduced, and quenched crystals were formed. Even if the bulk composition of the sample is stoichiometric, the quenched crystal structure and hydrogen contents should be different from *fcc* FeH due to the temperature gradient during quenching. For instance, in run S2 at 4020 K, FeH_2 appeared as a quenched crystal with *hcp* FeH*x*. If no quenched crystals are observed, the sample should remain at the subsolidus.

The melting temperature of *fcc* FeH*x* is summarized in Table 3.4. Surprisingly, it is near the melting curve of pure iron (Anzellini et al., 2013) (⊿T~500 K) and at least 1000 K above from the extrapolated melting curve by Sakamaki et al. (2009) at the CMB. During heating, the hydrogen content in the solid *fcc* FeH*x* was almost constant even when the liquid FeH*x* coexisted. Furthermore, the diffraction peaks from *fcc* FeH became sharper, but it became spotty. This indicated that the *fcc* is stable even at the high temperatures.

(6) Melting experiment for stoichiometric FeH*x* (Experiment F)

Melting experiments for substoichiometric FeH*x* were performed for runs U1, U4, M1–M3. The formation of quenched crystals was observed in U4, M1, M2, and M3. As with S1–S3, the sequence of laser heating and rapid quenching were repeated in M1–M3. In the case of run U1, the diffraction from the sample was lost due to melting during heating. The typical XRD sequence is indicated in Figures 3.11 (M1) and 3.8 (U1).

In order to confirm the melting of the sample in runs U1 and U4, textual characterization was performed. The intrusion of melt into pressure mediums can be utilized as a melting criterion. Also, a FIB with a secondary electron mode image (SIM) reflected a trend toward bulk crystallographic orientation (Mashino et al., 2019; Phaneuf, 1999). The cross-section of the heating spots is shown in Figure 3.12 and Figure 3.13. They indicated that both samples were molten. The low and high bounds for melting temperatures are listed in Table 3.4 and Figure 3.14.

3.4 Discussion: The phase diagram of the Fe-FeH binary system

It is widely accepted that the Fe-FeH system has a complete solid solution in the region between Fe and FeH (Figure 1.3), but as such, the phase diagram structure cannot explain this result in the present study. Three new findings should be taken into account: 1) a miscibility gap between *hcp* and *fcc* phases exists at the center of the binary system, even up to core pressures; 2) the melting temperature for the end-members of the binary system, Fe and FeH, is high, but the melting temperature of the middle of the system is low; 3) *fcc* and *hcp* are the stable crystal structures of the end member of the system, and *dhcp* FeH has a limited stability field.

I propose a new phase diagram for the Fe-FeH binary system. The type of diagram is a simple eutectic. I plotted the expected *x*–T phase diagram with the data in the present study at around 50 GPa and 135 GPa (Figure 3.15). In this kind of phase diagram, the composition of the eutectic points yields the maximum contents of the light elements in the core. This is because the outer core can not contain a light element that exceeds the eutectic composition (the right side of the eutectic phase diagram). If so, the crystallizing solid phase would be lighter than the coexisting liquid, but such a situation contradicts the observation of the present core. When the melting temperatures of the end member are similar, the eutectic composition should be near the middle of the binary, according to the Kordes formulas (*e.g.,* Yi–Jing et al., 1985). Therefore, the eutectic point of FeH*x* could be near the middle of the binary system (x= 0.5 ~ 0.6) in high pressures.

Recent *ab initio* calculation on the Fe-FeH system (Umemoto and Hirose, 2015) demonstrated that both the outer core density profile and V_P are reconciled by that of Fe + 1.0 wt %.H (FeHx~0.56). This composition could slightly exceed the eutectic composition, but it does not preclude hydrogen from being the predominant light element in the core.

The melting temperature of FeHx near the eutectic composition is low so that it would explain the lower melting temperature of the uppermost core (Nomura et al., 2014). If the melting temperature obtained in run M3 and the melting temperature of pure iron at the same conditions (4200 K) is interpolated linearly, the $FeH_{0.33}$ or more hydrogen-enriched phase can explain the geotherm estimated by Nomura et al. (2014). The outer core could contain the other kind of light elements; therefore, the freezing point would be lower.

If hydrogen is the dominant light element in the core, *hcp* FeHx will crystallize as the inner core material, which is the same as the crystal structure of pure Fe and Fe-Ni alloys in the inner core (Tateno et al., 2012, 2010). Both *fcc* and *hcp* structures are close-packing for iron, but the symmetry of hydrogen atoms is different. For hcp FeHx, the distance of the O-sites among nearest-neighbor, which are occupied by hydrogen, is closer than that of fcc. It would change the diffusivity of hydrogen in FeHx in high temperatures, where hydrogen behaves like fluid (Fukai and Sugimoto, 1985). It could soften the bonding of iron atoms like the “pre-melting” effect (Martorell et al., 2013) and hydrogen could reduce the V_S at the inner core.

3.5 Conclusion

I have extended the melting experiments on the Fe-FeH binary system to 173 GPa and determined the phase relation of non-stoichiometric FeH*x* by using a laser-heated diamond anvil cell. The phase diagram of the Fe-FeH system is of eutectic type, which is different from the complete solid solution type phase diagram conventionally accepted. Furthermore, the stable pressure-temperature–*x* condition of the *dhcp* phase is smaller than previously expected. The miscibility gap was found between x=0.44 and 0.69 in the pressures of the experiments. The melting temperature near the eutectic composition is sufficiently low up to at least 157 GPa and it would explain the low solidus temperature of the pyrolite. If hydrogen is the sole light element in the core, the outer core would contain around 1 wt.% hydrogen and is likely within the left side of the eutectic composition. Therefore, it is feasible to solidify the dense solid inner core. Although future work should address an experiment at inner core conditions and the credibility of estimation of hydrogen contents, all features of the phase diagram of the Fe-FeH system does not preclude hydrogen bearing the terrestrial core.

Figures and tables

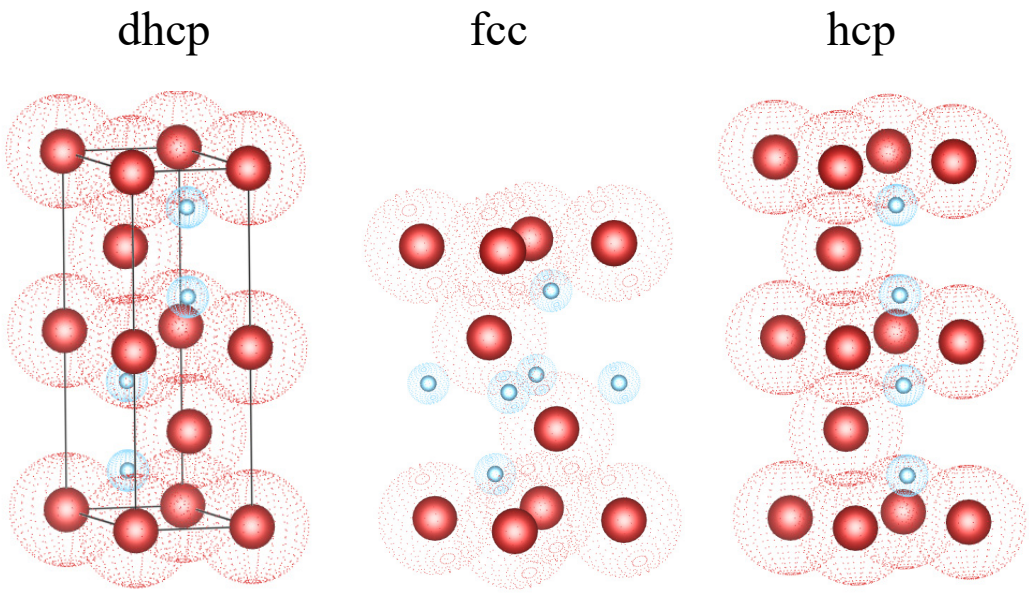

Figure 3.1 Crystal structure of FeH*x* ($x \leq 1$)

Red and blue circles show regular positions of iron and hydrogen atoms, respectively. Dot-surface spheres indicate the ideal radii of each atom. Hydrogen atoms usually occupy octahedral sites (o-site). Three phases reported as the crystal structure of FeH*x* ($x \leq 1$);

Left: Double hexagonal close-packed (*dhcp*) structure, $P6_3/mmc$

Center: Face centered cubic (*fcc*) structure, $Fm\bar{3}m$

Right: Hexagonal close-cacked (*hcp*) structure, $P6_3/mmc$

All of them have close-packed structures, but the stacking patterns of iron atoms are different as following;

dhcp's pattern is A, B, A, C, A, B, . . .

fcc's pattern is A, B, C, A, B, C, A, . . .

and *hcp*'s pattern is A, B, A, B, . . .

Both *fcc* and *hcp* have nonstoichiometric (x<1) composition for FeH*x* (Yamakata et al., 1992; Machida et al., 2019; Ikuta et al. 2019), and hydrogen atoms would take the o-sites randomly. Note that Machida et al. (2014) reported that hydrogen could occasionally exist in the tetragonal site of the *fcc* phase. All of the structural models were drown by VESTA (Momma and Izumi, 2011).

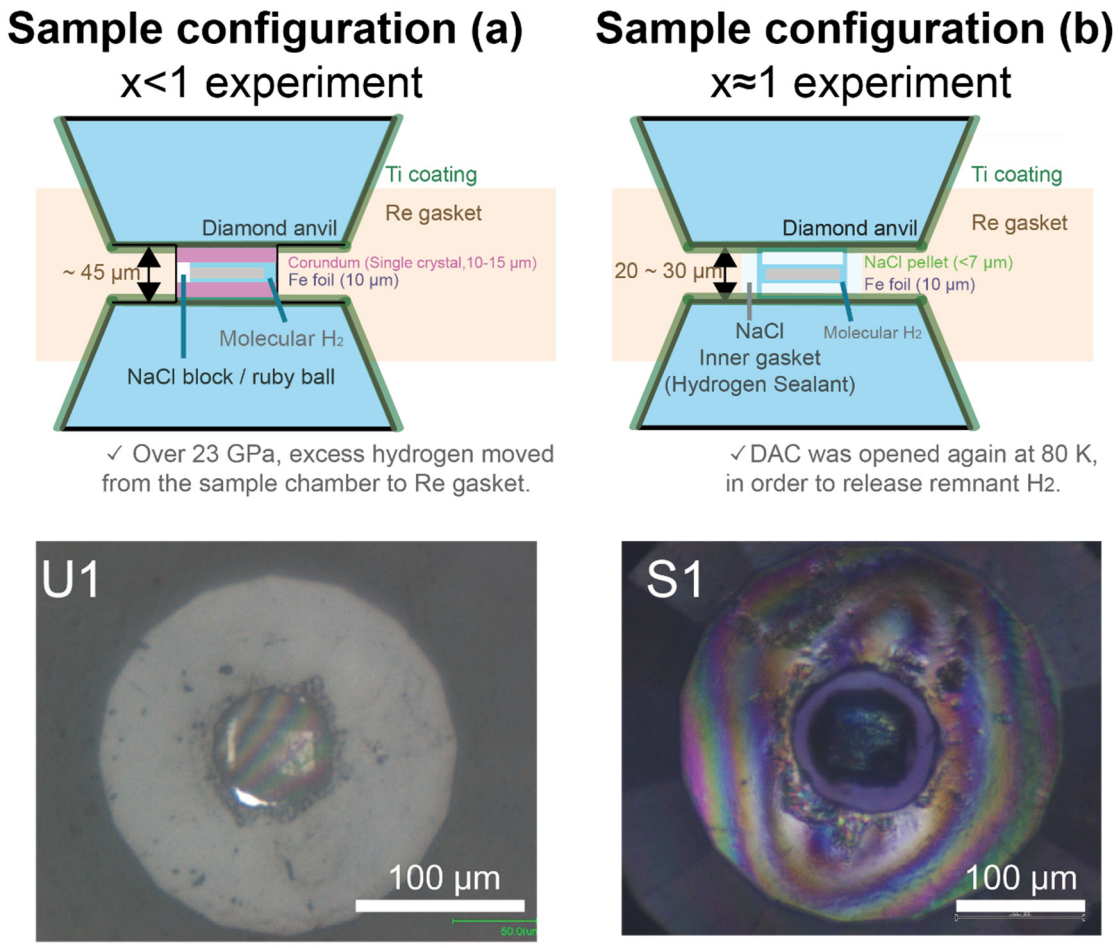

Figure 3.2 Schematic of sample configurations and photographs of the samples

The photographs were obtained just after recovery to room temperature from the liquid hydrogen loading system.

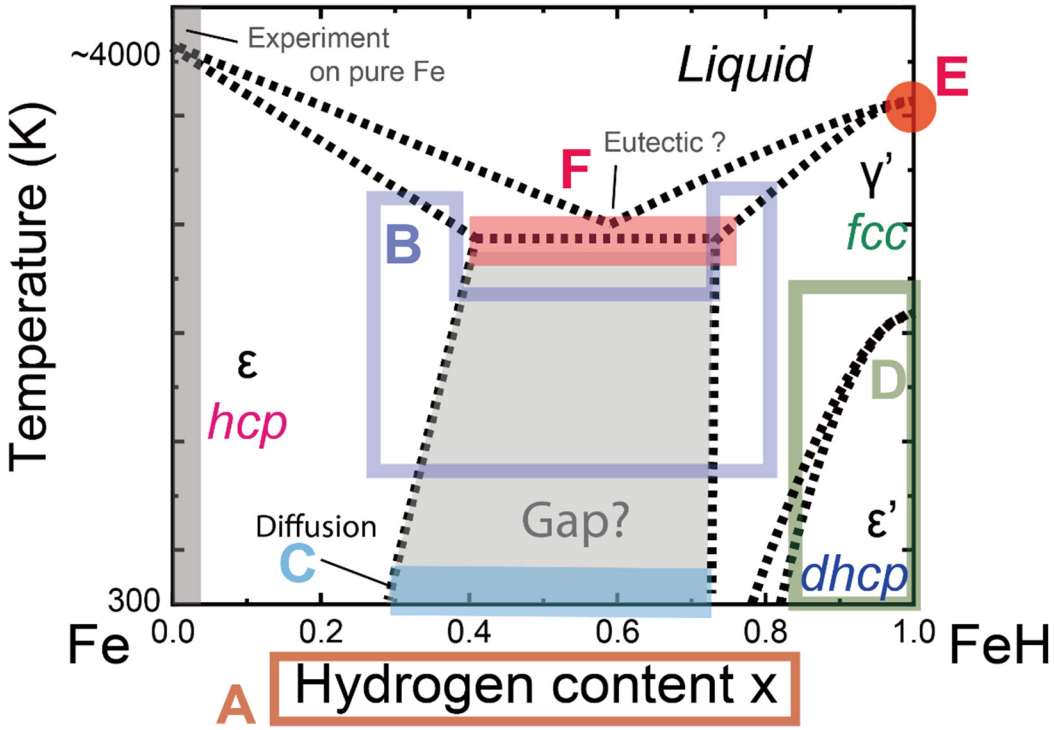

Figure 3.3 Design of this experiment.

This figure illustrates the outline of each experiment in this work on a schematic phase diagram of the Fe-FeH system. At first, I performed compression/decompression experiments of stoichiometric FeH (**Experiment A**) and refined a criterion to quantify the hydrogen contents. Each region marked with the letters B–F, correspond to the composition and temperature range where experiments were performed. The types of experiments are listed below.

Experiment B) Laser heating experiments to confirm the miscibility gap between the hcp and fcc phase.

Experiment C) A room-temperature experiment in which hydrogen diffused in a FeHx sample.

Experiment D) Compression/heating experiment to confirm the narrow stability field of dhcp.

Experiment E) Melting experiments on stoichiometric FeH.

Experiment F) Melting experiments on sub-stoichiometric FeH*x*.

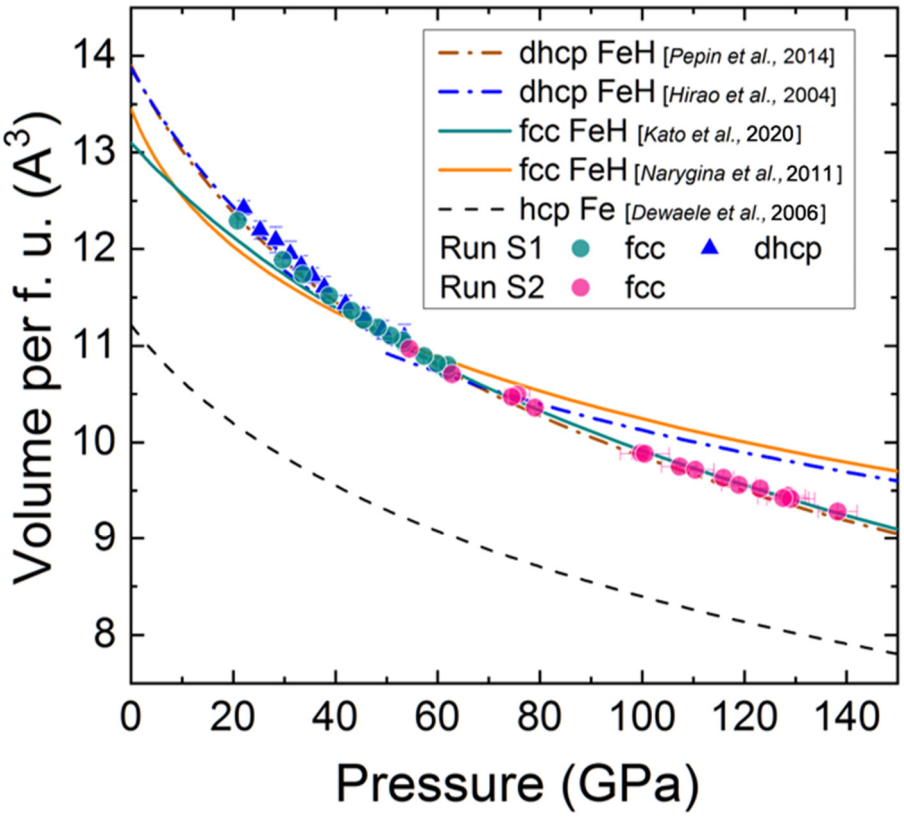

Figure 3.4 Compression behavior of *dhcp* and *fcc* FeH

Compression curves of *dhcp* FeH (blue triangles, run S1) and *fcc* FeH (green circles, run S1; pink circles, run S2). Totally, four previous studies were reported for *dhcp* FeH (red dot-dash curve, Pépin et al., 2014; blue dot-dash curve, Hirao et al. 2004) and *fcc* FeH (green curve, nonmagnetic phase from Kato et al., 2020; orange curve, Narygina et al., 2011). Our data indicate the validity of the EoS by Pépin et al. (2014) and Kato et al. (2020). The volume difference between *fcc* FeH in my data and the dhcp / fcc EoS is only 0.8% at 138 GPa. As a reference, the compression curve of *hcp* Fe was also shown (black dash line, Dewaele et al., 2006).

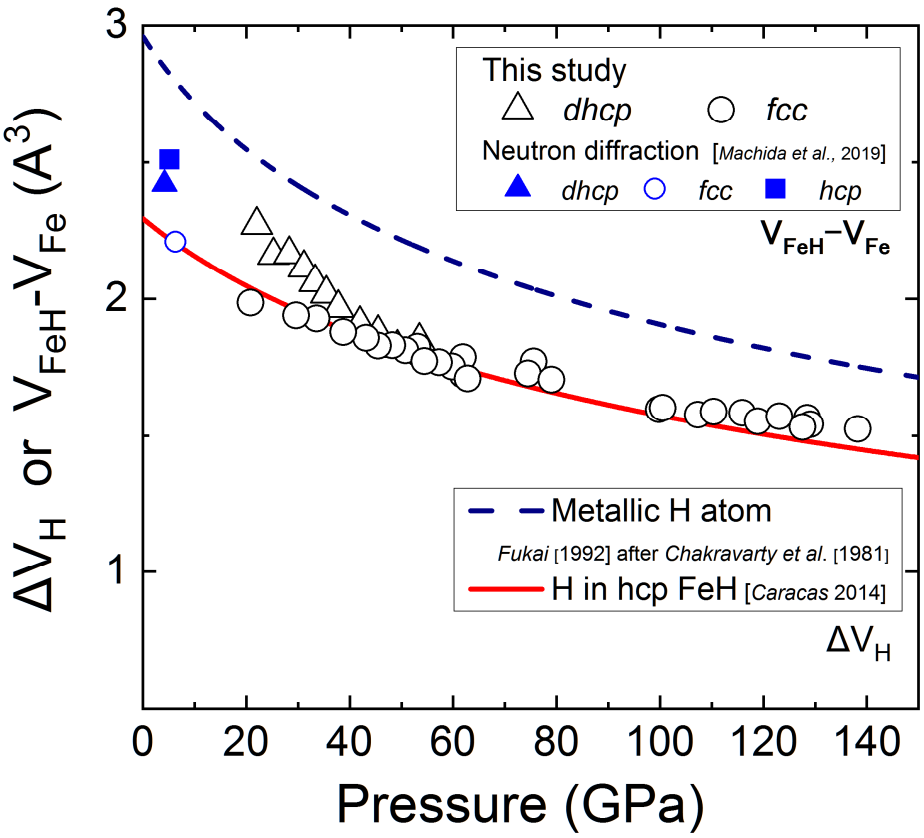

Figure 3.5 Pressure dependence of ΔV_{H}

The term of $V_{\mathrm{FeH}} - V_{\mathrm{H}}$ calculated from *dhcp* FeH (open triangles, run S1) and *fcc* FeH (open circles, runs S1 and S2) are shown with other references. ΔV_{H} obtained in neutron diffraction (Machida et al., 2019) were plotted with blue symbols. The data $V_{\mathrm{FeH}} - V_{\mathrm{H}}$ agree well with the proposed ΔV_{H} in Caracas (2015) (solid red line) above 40 GPa. The deviation of the *dhcp* FeH below 40 GPa should be ascribed to the ferromagnetism of its phase.

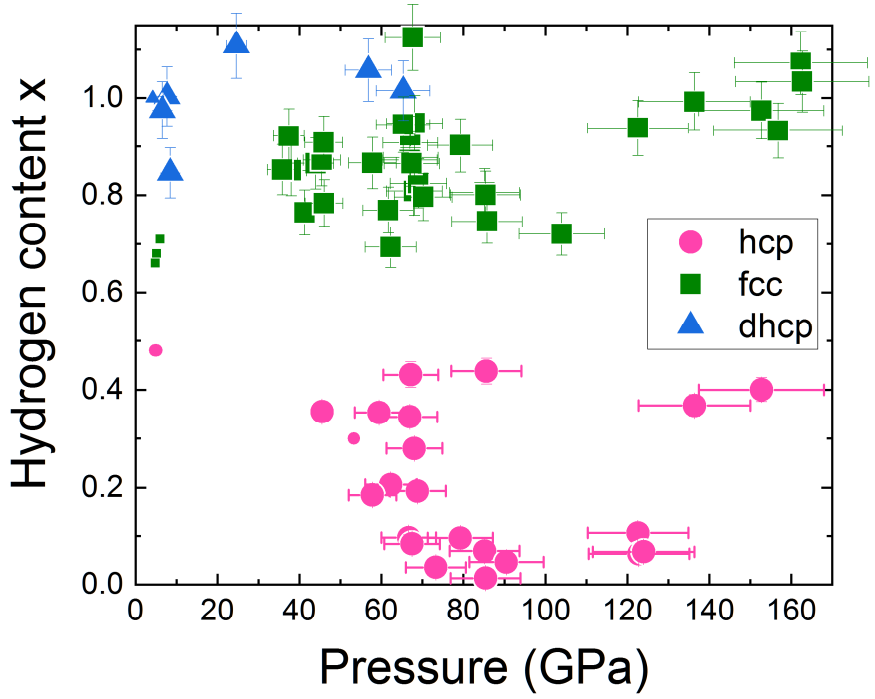

Figure 3.6 Hydrogen contents of FeH*x*

Pressure vs. hydrogen contents plot for *dhcp* FeH (blue triangles), *hcp* (pink circles), and *fcc* FeH (green squares). Small points indicate the data provided by previous studies (Kato et al., 2020; Machida et al., 2019) and large points show the data in this study. Note that the stability field of *dhcp* should disappear over ~1000 K, and a low hydrogen content *fcc* (x<0.15) region should exist at higher temperatures (Ikuta et al., 2019) while the region should be smaller and disappear above ~105 GPa. The stability field of this two–fcc phase would be separated. The P-T phase diagram of Co would be an analog of these two *fcc* phases; it also has *fcc* (ferromagnetic) to *hcp*, to *fcc* (nonmagnetic) phase transitions (Yoo et al., 2000). *Hcp* pure iron is stable up to inner core pressures (Tateno et al., 2010), which also supports FeH*x* (x<0.5) having the same structures. This result indicates that Fe–FeH binary system has a miscibility gap between $0.44 < x < 0.69$, and it expands in high-pressure and high-temperature conditions.

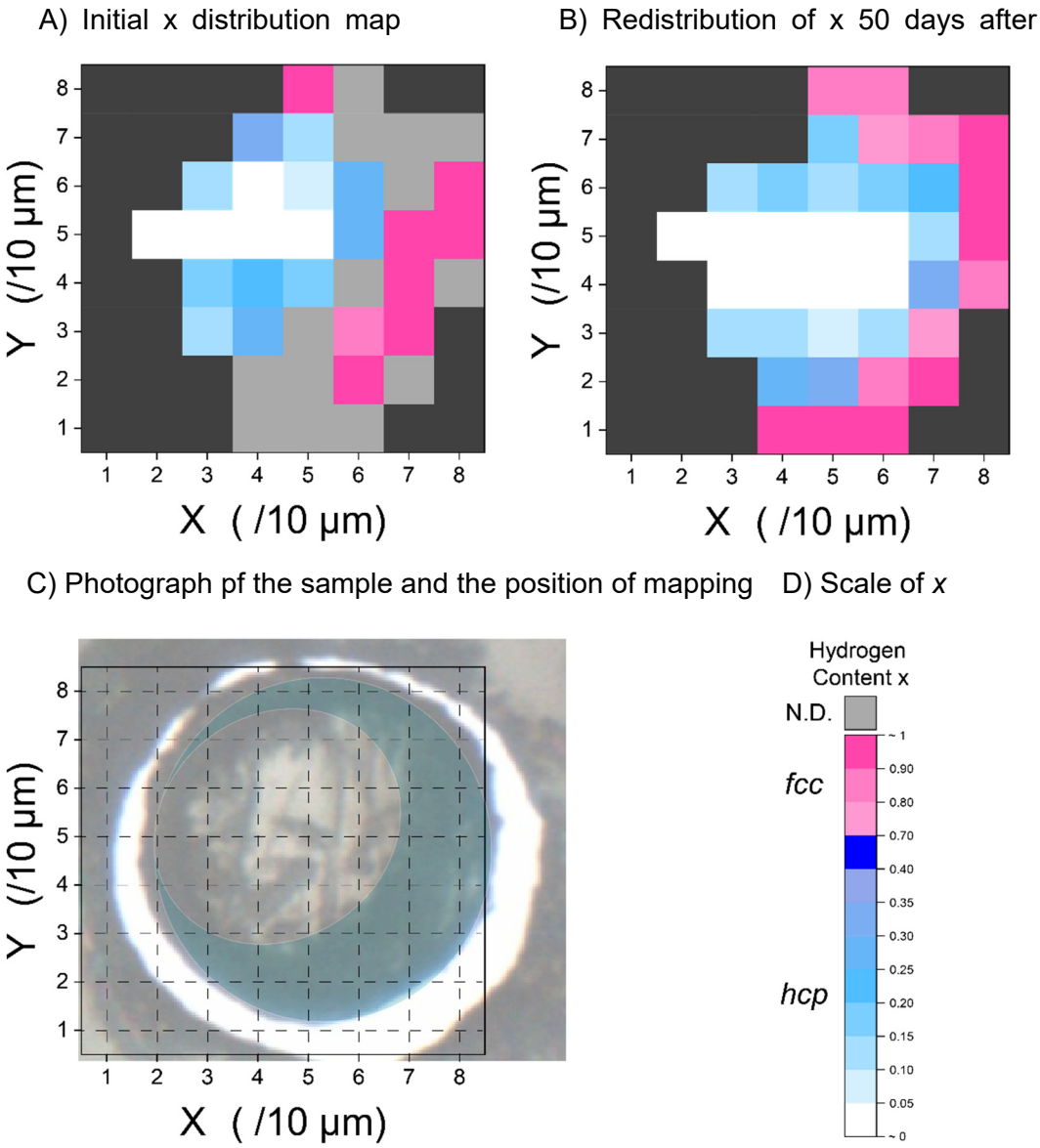

Figure 3.7 A room–temperature experiment in which hydrogen diffused in a sample

The distribution of hydrogen contents, *x*, at the initial condition (A) and fifty days after (B) are indicated. The distribution map was drawn on a 10–μm mesh, along with samples (C, each intersection of the mesh). The hydrogen contents and phases are indicated in color (D). Only the scattering from the short-range ordering was observed in gray positions.

1)

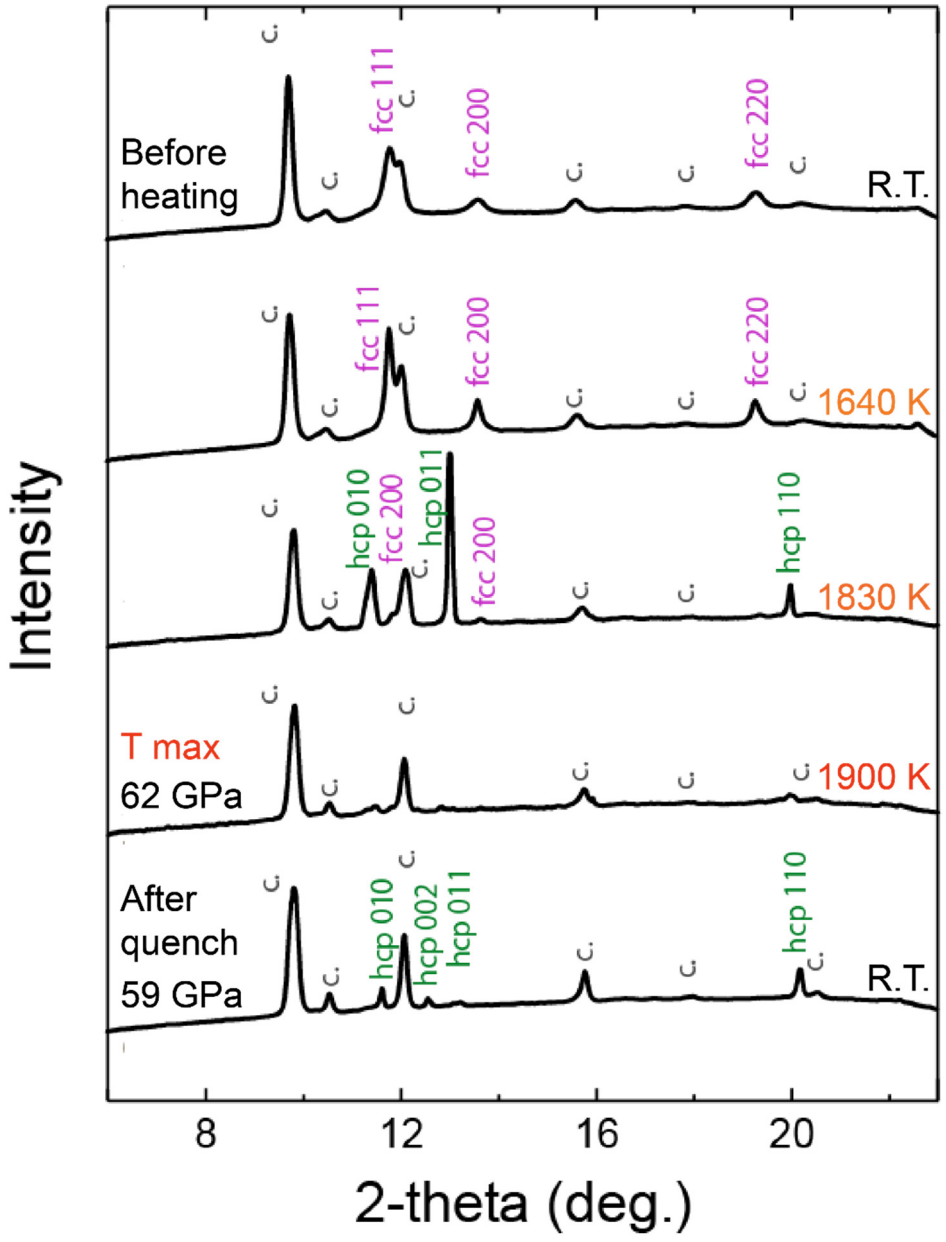

Figure 3.8 (*continued*)

2)

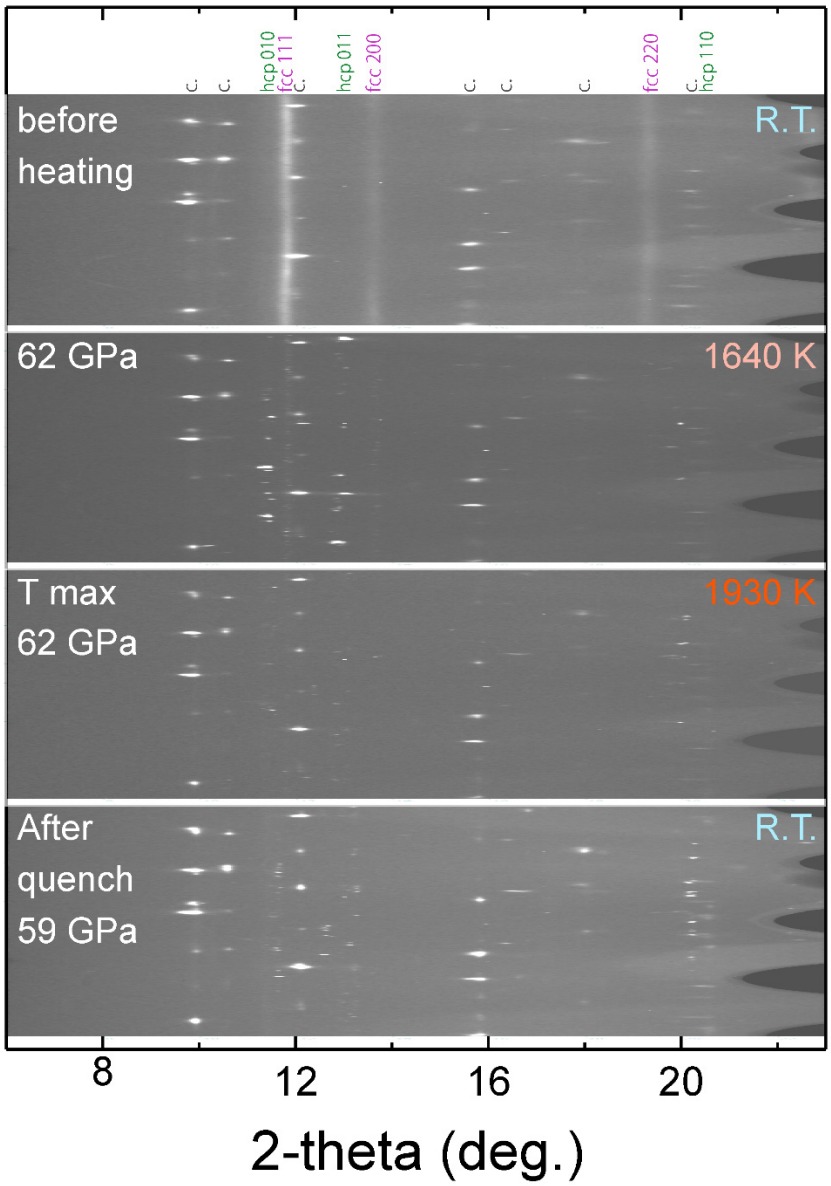

Figure 3.8 A sequence of X-ray diffraction patterns during melting experiments in run U1
1) One-dimensional patterns and 2) unrolled XRD images. Peaks with "c." indicate the diffraction from corundum. When the laser power was added, the bulk hydrogen contents were decreased because this experiment was performed in the configuration (a) in Figure 3.2. A single-phase *fcc* FeH$x_{\sim 0.77}$ separated to *fcc* FeH$x_{\sim 0.69}$ and *hcp* FeH$x_{\sim 0.21}$. At 1900 K, no peak from the solid FeHx was observed, indicating that the sample was completely molten. The wavelength of the incident X-ray beam was 0.41424(8) Å (~30 keV) in this run.

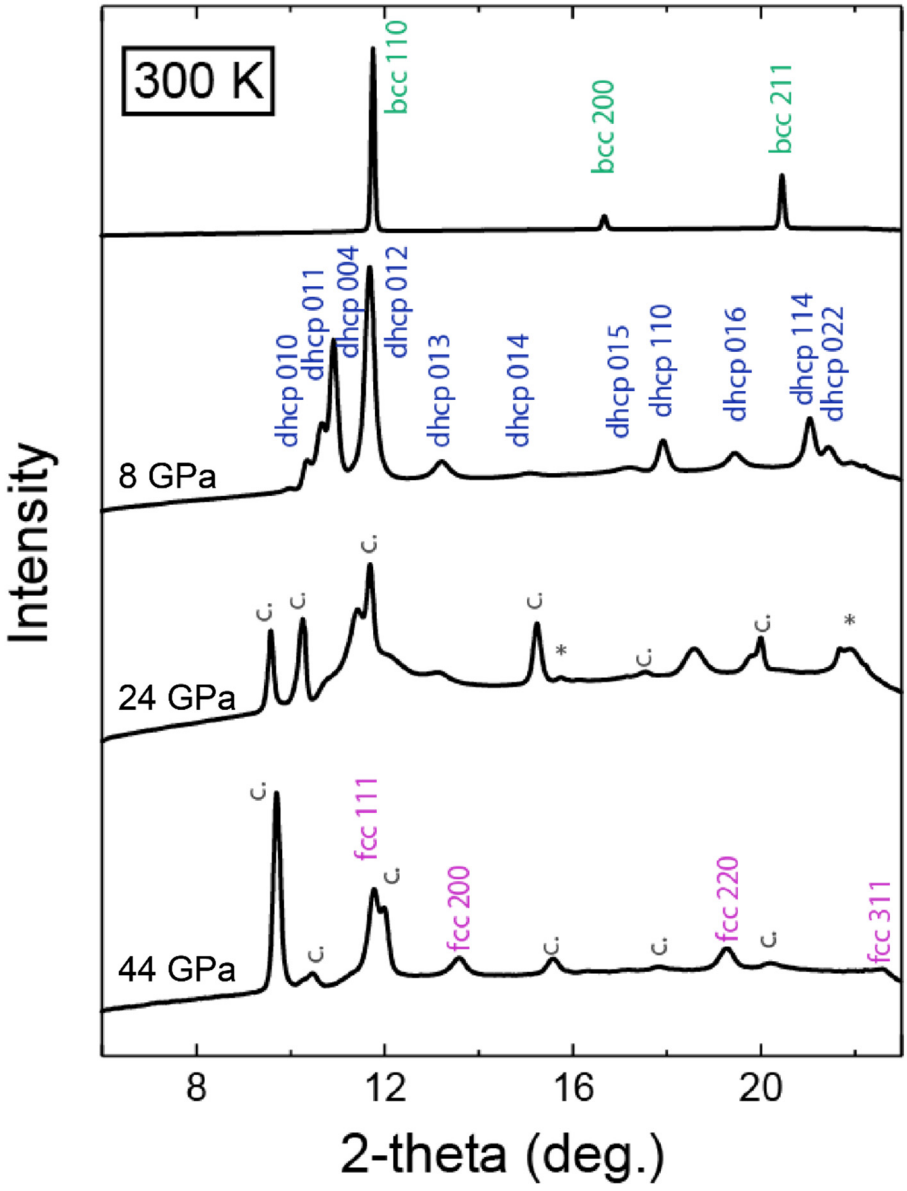

Figure 3.9 Sequence of X-ray diffraction patterns during compression in run U1

Diffraction patterns in #U1 during compression at room temperature. Peaks with "c." indicate the diffraction from corundum. Just after the hydrogen loading, the diffraction peaks from *bcc* Fe were observed. The volume was similar to that of pure Fe. After compressed and thermal annealing, the *dhcp* phase appeared. The temperature was not measurable because it was too low. Its hydrogen content was ~1.0. Subsequently, around 25 GPa, the *dhcp* phase collapsed. After additional thermal annealing, it changed to *fcc* $FeH_{0.87}$, meaning that the dhcp phase was not stable. Note that the wavelength of the incident X-ray beam was 0.41424(8) Å (~30 keV) in this run.

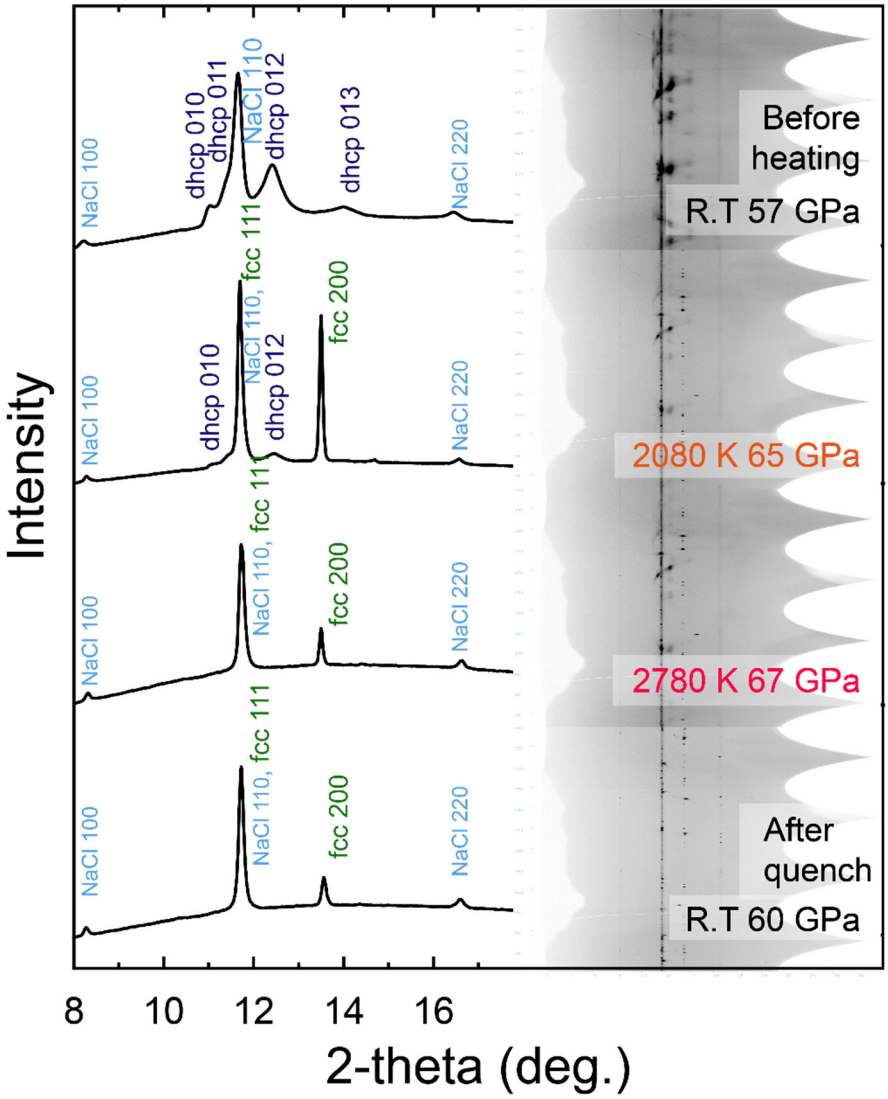

Figure 3.10 A sequence of X-ray diffraction patterns during melting experiments in run S1
One dimensional patterns (left) and unrolled XRD images (right). Before the laser heating, a single-phase *dhcp* FeH$x_{\sim 1}$ was observed. However, diffraction from the *dhcp* phase gradually weakened and almost disappeared at 2080 K and 65 GPa. *Fcc* FeH*x* is stable even at 2780 K. The wavelength used was 0.41413(6) Å.

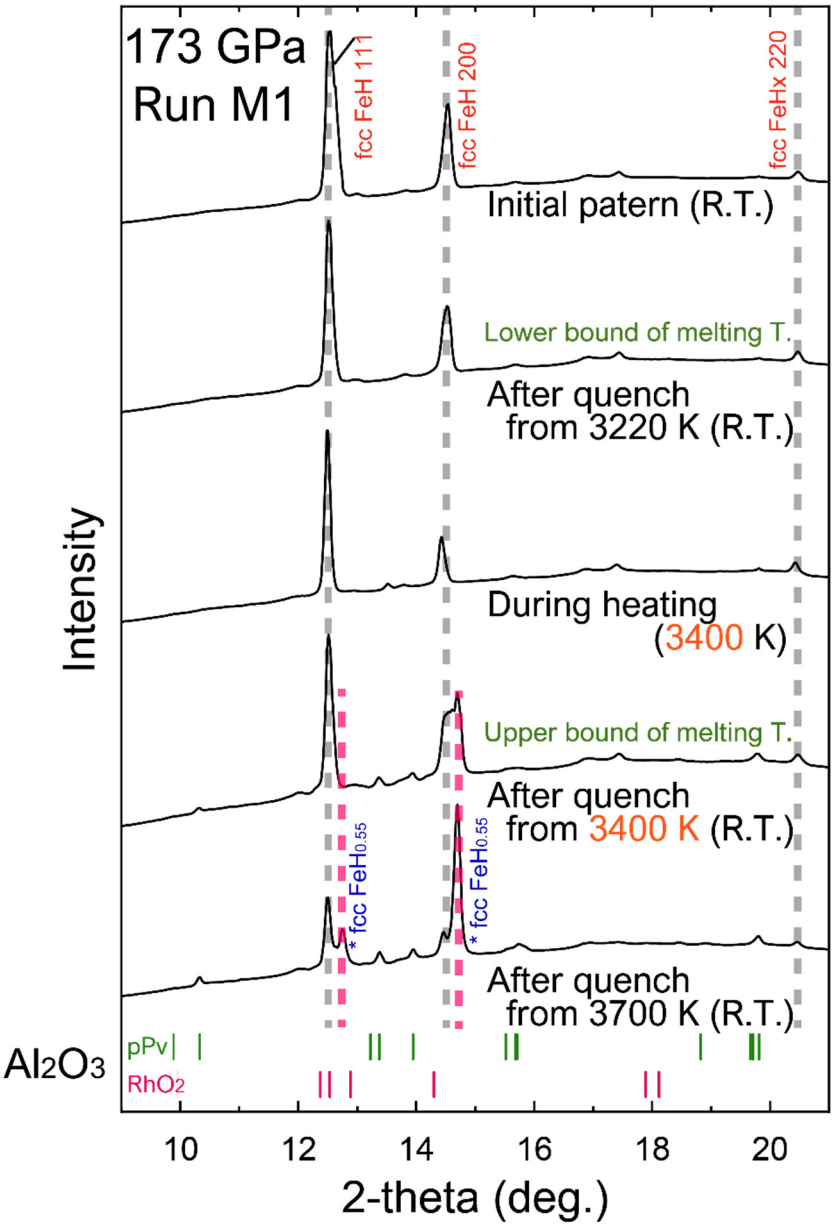

Figure 3.11 A sequence of X-ray diffraction patterns during melting experiments in run M1 In this run, the sequence of laser heating and rapid temperature quenching was repeated. The period of each quenching was around 10~100 μsec. Since I used the cell configuration (A) for this experiment, the hydrogen content in the sample chamber could decrease. Though, after heating this at 3220 K, the hydrogen content in the *fcc* $FeH_{0.95}$ did not change. However, after quenching from 3400 K, *the fcc* $FeH_{0.55}$ appeared as a quench crystal. Note that the *fcc* $FeH_{0.55}$ disappeared at high temperatures when the sample was reheated. Be it also noted that the high-pressure phase of Al_2O_3 did not overlap on the peaks of FeH*x*. The wavelength of the incident X-ray beam was 0.41314(4) Å (~30 keV).

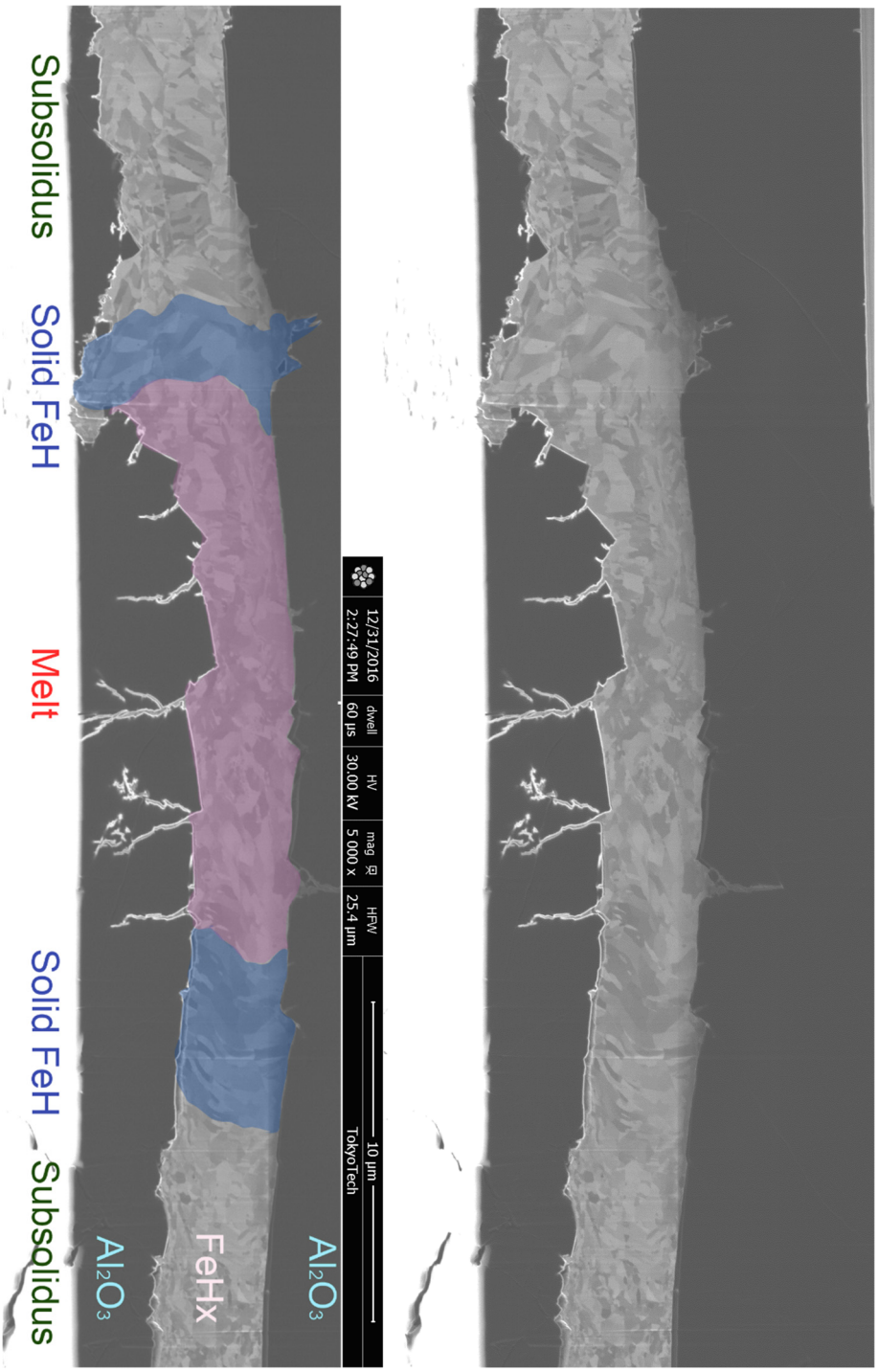

Figure 3.12 FIB scanning ion microscope (SIM) image from run U1

(Right) A full image of the cross-section around the heated spot is indicated. FeH*x* intruded into Al_2O_3 near the center.

(Left) This is an interpretation of the microstructure of the sample. Crystallographic orientation appears as the image contrast, which reflects thermal history.

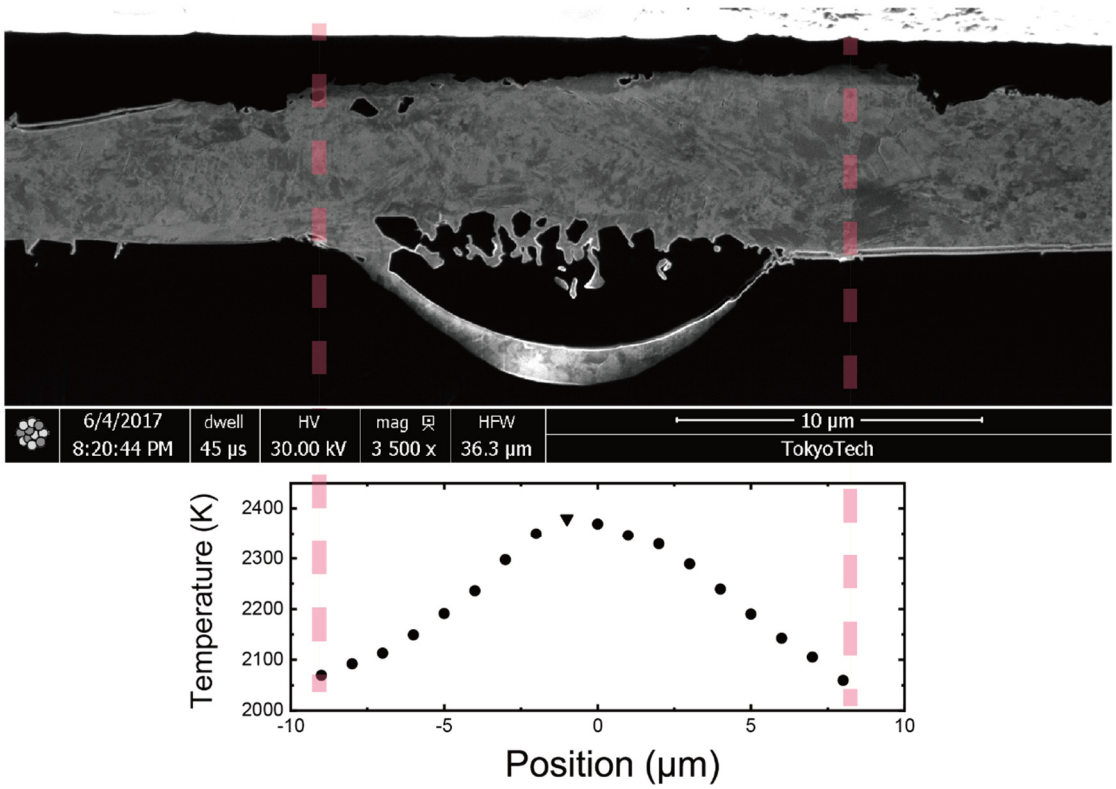

Figure 3.13 SIM image and its temperature distribution from run U4

In run U4, temperature distribution along the cross-section was obtained, which provides the temperature at the liquid/solid boundary (red broken lines) (Mori et al., 2017). The sample was identified as *fcc* $FeH_{0.85}$. The melting temperature of this sample was estimated to be 2070±100 K.

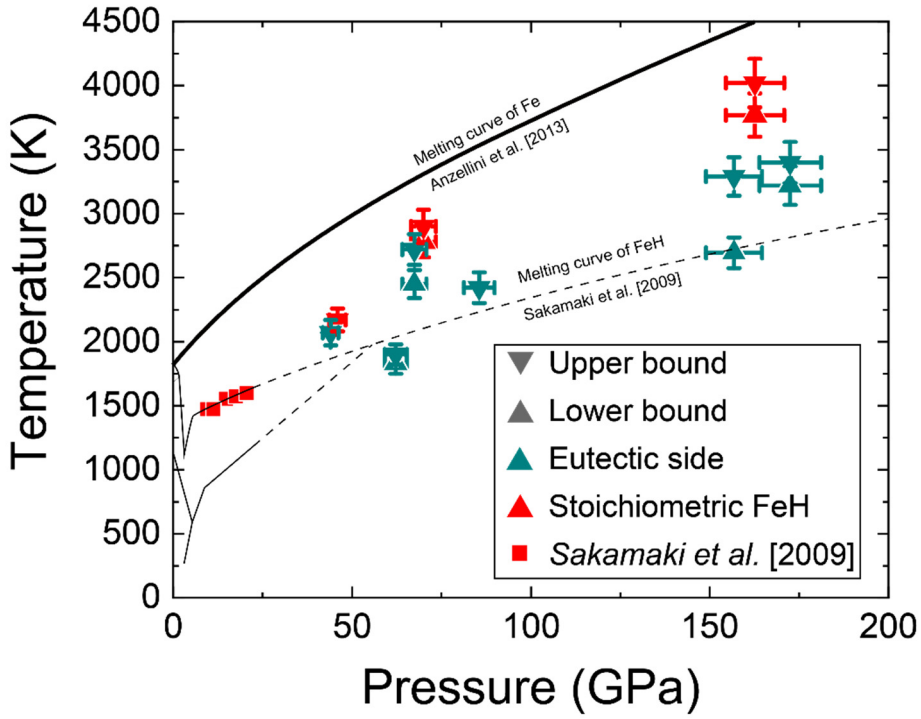

Figure 3.14 Melting temperature of FeH*x*

The melting temperatures of FeH*x* obtained in this study are plotted. Inverse triangles and regular triangles show the upper bound and lower bound of the melting temperature, respectively. Green symbols indicate that the hydrogen content of the bulk sample is sufficiently lower than 1, and red symbols represent the melting temperature of stoichiometric FeH. Red squares show the melting temperature in the previous study (Sakamaki et al., 2009). The melting curve for iron (Anzellini et al., 2013) and the extrapolated melting curve of FeH from Sakamaki et al. (2019) are also shown.

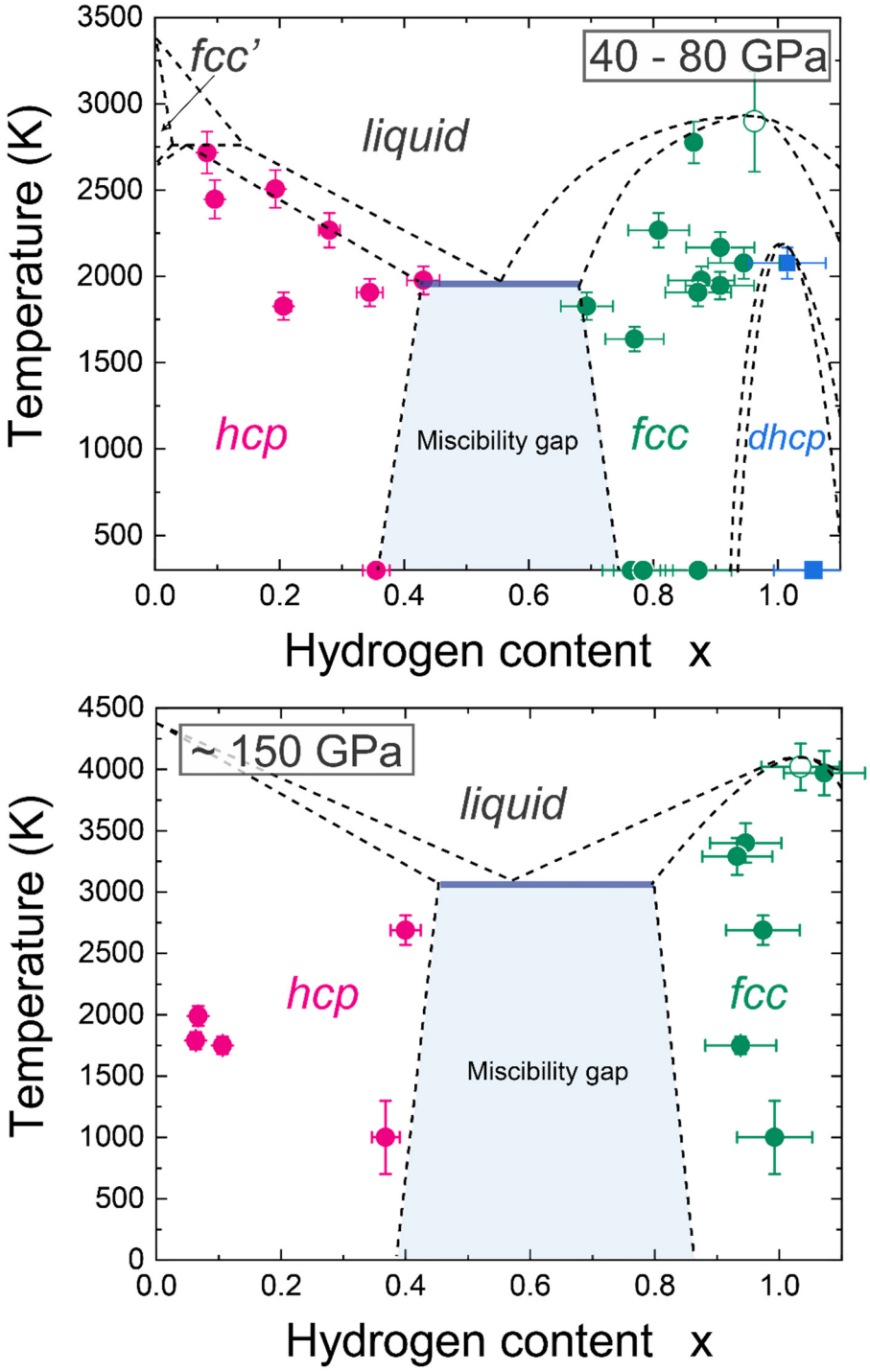

Figure 3.15 Phase diagram of the Fe-FeH binary system

Each plot indicates the stable phase observed at the conditions shown in Table 3.3. In the diagram at ~ 150 GPa, the plots after annealing were assumed that it showed hydrogen contents at the annealing temperature, 1000±300 K. The result of this study, indicates that the phase diagram of the Fe-FeH system is of eutectic type. Open circles show the upper bound of the melting temperature in run S1 and S2.

Table 3.1 Summary of experimental conditions

Run #	Highest P & T		Cell assembly	Experimental type						Phase relations
	Pressure (GPa)	Temperature (K)		(A)	(B)	(C)	(D)	(E)	(F)	
U1	62 (6)	1900 (80)	(a)		○		○		○	*dhcp*▶*fcc*▶*fcc+hcp*
U2	85 (9)	1980 (80)	(a)		○					*dhcp*▶*fcc*▶*fcc+hcp*
U3	124 (12)	1990 (80)	(a)		○					*fcc*▶*fcc+hcp*
U4	44 (4)	2070 (100)	(a)		○				○	*fcc*
D	90 (9)	2460 (110)	(c)		○	○				*fcc+hcp*
M1	173 (17)	3400 (160)	(a)		○				○	*fcc*▶*fcc+hcp*
M2	67 (7)	2720 (120)	(a)		○				○	*hcp*
M3	157 (16)	3290 (150)	(a)		○		○		○	*fcc*▶*fcc+hcp*
S1	70 (7)	2900 (130)	(b)	○			○	○		*hcp*▶*dhcp*▶*fcc*
S2	163 (16)	4020 (190)	(b)	○				○		*fcc*
S3	46 (5)	2170 (90)	(b)					○		*fcc*

Table 3.2 Experimental results of compression of stoichiometric *dhcp* and *fcc* FeH

Run	NaCl				FeH					ΔV_H
	V (Å^3)	±V	Pressure† (GPa)	±P	Phase	a (Å)	c (Å)	Volume‡ (Å^3)	±V	
S1#	126.2	0.2	19.7	0.1	*hcp*	2.60	4.25	12.44	0.03	2.20
	123.5	0.1	22.0	0.1	*dhcp*	2.60	8.48	12.43	0.07	2.27
	120.1	0.2	25.2	0.3	*dhcp*	2.58	8.43	12.20	0.09	2.16
	117.2	0.2	28.3	0.3	*dhcp*	2.58	8.41	12.09	0.13	2.16
	27.4	0.0	31.1	0.2	*dhcp*	2.57	8.37	11.95	0.13	2.11
	27.0	0.0	33.3	0.3	*dhcp*	2.56	8.34	11.83	0.10	2.06
	26.6	0.1	35.5	0.4	*dhcp*	2.55	8.32	11.72	0.08	2.02
	26.3	0.1	37.8	0.5	*dhcp*	2.54	8.30	11.60	0.11	1.97
	25.7	0.1	42.0	0.8	*dhcp*	2.53	8.26	11.43	0.09	1.91
	25.2	0.0	45.4	0.1	*dhcp*	2.52	8.25	11.31	0.09	1.88
	24.7	0.0	49.2	0.1	*dhcp*	2.51	8.20	11.16	0.10	1.82
	24.3	0.0	53.4	0.4	*dhcp*	2.51	8.15	11.09	0.13	1.85
	23.4	0.0	61.8	0.1	*fcc*	3.50		10.74	0.03	1.72
	23.4	0.0	61.9	0.3	*fcc*	3.51		10.80	0.02	1.79
	23.6	0.1	59.8	0.6	*fcc*	3.51		10.82	0.02	1.75
	23.9	0.1	57.3	1.2	*fcc*	3.52		10.89	0.01	1.77
	24.3	0.0	53.3	0.5	*fcc*	3.53		11.03	0.03	1.80
	24.3	0.1	53.1	0.6	*fcc*	3.54		11.06	0.01	1.83
	24.6	0.1	50.8	1.0	*fcc*	3.54		11.10	0.01	1.81
	24.9	0.2	48.2	1.7	*fcc*	3.55	—	11.19	0.05	1.83
	25.2	0.1	45.4	0.5	*fcc*	3.56		11.27	0.02	1.83
	25.5	0.1	43.1	0.4	*fcc*	3.57		11.36	0.02	1.86
	26.1	0.0	38.8	0.0	*fcc*	3.58		11.52	0.02	1.88
	27.0	0.0	33.6	0.1	*fcc*	3.61		11.74	0.01	1.93
	27.7	0.1	29.7	0.3	*fcc*	3.62		11.89	0.02	1.94
	124.9	0.1	20.8	0.1	*fcc*	3.66		12.29	0.03	1.99
S2	24.2	0.0	54.5	0.4	*fcc*	3.53		10.97	0.00	1.77
	23.3	0.1	62.8	0.8	*fcc*	3.50		10.71	0.04	1.71
	22.3	0.2	75.6	2.4	*fcc*	3.48		10.49	0.01	1.77
	22.3	0.1	74.5	1.0	*fcc*	3.47		10.47	0.01	1.73
	22.0	0.1	79.0	0.9	*fcc*	3.46		10.36	0.02	1.71
	20.7	0.1	99.8	1.8	*fcc*	3.41		9.89	0.02	1.60
	20.6	0.3	100.5	4.8	*fcc*	3.41		9.88	0.01	1.60
	20.2	0.2	107.3	3.5	*fcc*	3.39		9.75	0.00	1.58
	20.1	0.2	110.4	3.7	*fcc*	3.39	—	9.72	0.00	1.59
	19.8	0.1	115.9	2.0	*fcc*	3.38		9.63	0.01	1.58
	19.7	0.2	118.9	3.3	*fcc*	3.37		9.56	0.01	1.55
	19.5	0.1	123.1	1.2	*fcc*	3.36		9.52	0.00	1.57
	19.2	0.2	128.5	3.5	*fcc*	3.36		9.45	0.00	1.57
	19.2	0.2	129.1	4.7	*fcc*	3.35		9.41	0.00	1.54
	19.3	0.2	127.6	5.0	*fcc*	3.35		9.42	0.01	1.53
	18.8	0.1	138.2	3.8	*fcc*	3.34		9.28	0.00	1.53

† Calculated based on Dorogokupets & Dewaele (2007). The error was determined from the fitting error in the XRD analysis of the volume of NaCl.

‡ Indicated as a volume per formula unit (*hcp*, Z=2; *dhcp* and *fcc*, Z=4).

Decompression was performed in the green hatching lines.

Table 3.3 Experimental result of FeH*x* phase relations

Run #	Experimental conditions				Pressure medium[a]		FeH*x*																	
							hcp						*fcc*					*dhcp*						
	P	±P	T[b]	±T	V	±V	a	c	V	±V	***x***	±*x*	a	V	±V	***x***	±*x*	a	c	V	±V	***x***	±*x*
	(GPa)		(K)		(Å^3)		(Å)		(Å^3)				(Å)	(Å^3)				(Å)	(Å)	(Å^3)			
U1	8	1 *	-	R														2.66	8.69	53.08	0.23	**1.00**	0.06
	44	4 *	-	C	223.6	2.8							3.54	44.34	0.08	**0.87**	0.05						
	62	6	1640	70 C	219.4	1.5							3.50	42.80	0.05	**0.77**	0.05						
	62	6	1830	80 C	216.8	1.6	2.39	3.92	19.44	0.36	**0.21**	0.01	3.49	42.41	0.09	**0.69**	0.04						
	62	6	1900	80 C	215.9	1.6									*Liquid*								
	59	6 *	-	C	215.9	1.6	2.37	4.00	19.47	0.14	**0.35**	0.02											
	58	6 *	-	C	216.7	0.4	2.40	3.79	18.95	0.18	**0.19**	0.01	3.49	42.57	0.05	**0.87**	0.05						
U2	7	1 *	-	C	249.2	1.8												2.66	8.69	53.18	0.13	**0.97**	0.06
	38	4 *	-	C	227.0	0.3							3.56	45.11	0.04	**0.85**	0.05						
	45	5 *	-	C	222.8	0.5							3.54	44.19	0.09	**0.87**	0.05						
	67	7	1950	80 C	218.7	0.5							3.52	43.43	0.03	**0.91**	0.05						
	67	7	1980	80 C	218.0	0.5	2.44	3.87	20.03	0.80	**0.43**	0.03	3.51	43.24	0.06	**0.88**	0.05						
	67	7	1910	80 C	217.7	0.4	2.43	3.87	19.72	0.60	**0.34**	0.02	3.51	43.16	0.09	**0.87**	0.05						
	68	7	2270	100 C	217.1	0.4	2.41	3.88	19.58	0.10	**0.28**	0.02	3.50	42.98	0.04	**0.81**	0.05						
	69	7	2510	110 C	216.4	0.3	2.40	3.88	19.34	0.12	**0.19**	0.01											
	69	7 *	-	C	211.7	1.1							3.45	41.06	0.18	**0.82**	0.05						
	70	7 *	-	C	211.2	1.3							3.44	40.75	0.19	**0.80**	0.05						
	85	9	1920	80 C	209.2	0.6	2.34	3.81	18.04	0.21	**0.07**	0.00	3.44	40.77	0.07	**0.81**	0.05						
	85	9	1980	80 C	208.6	1.5	2.34	3.77	17.87	0.17	**0.01**	0.00	3.44	40.76	0.07	**0.80**	0.05						
	79	8 *	-	C	207.5	0.8	2.34	3.74	17.81	0.11	**0.10**	0.01	3.44	40.59	0.26	**0.90**	0.05						
U3	86	9 *	-	C	205.0	1.0							3.39	38.98	0.11	**0.75**	0.05						
	123	12	1750	70 C	198.4	0.5	2.30	3.69	16.96	0.03	**0.11**	0.01	3.37	38.37	0.05	**0.94**	0.06						
	123	12	1790	70 C	197.6	0.8	2.29	3.70	16.83	0.01	**0.06**	0.00											
	124	12	1990	80 C	197.6	0.3	2.30	3.70	16.87	0.03	**0.07**	0.00											
U4	37	4 *	-	C	227.3	2.6							3.58	45.73	0.02	**0.92**	0.06						
	36	4 *	-	C	228.2	1.2							3.57	45.46	0.01	**0.85**	0.05						

Table 3.3 (Continued)

Run #	P (GPa)	Perr	T (K)	Terr		V (Å^3)	±V	a (Å)	c (Å)	V (Å^3)	±V	***x***	±*x*	a (Å)	V (Å^3)	±V	***x***	±*x*	a (Å)	c (Å)	V (Å^3)	±V	***x***	±*x*
D	46		300	-	C	222.8	0.8	2.44	3.91	20.17	0.86	**0.36**	0.02											
	41		300	-	C	225.1	1.3							3.53	43.97	0.17	**0.76**	0.05						
	68	7	* -		C	212.2	0.9							3.51	43.26	0.07	**1.12**	0.07						
	73	7	* -		C	209.9	0.9	2.34	3.75	17.82	0.09	**0.04**	0.00											
	68	7	* -		C	212.0	2.0							3.48	42.00	0.64	**0.95**	0.06						
	90	9	2460	110	C	210.9	1.6	2.34	3.77	17.95	0.04	**0.05**	0.00											
M1	173	17	3400	160	P	117.5[c]	0.1							3.31	36.37	0.33	**0.95**	0.06						
M2	67	7	2450	110	C	216.9	0.6	2.40	3.83	19.09		**0.10**	0.01											
	67	7	2720	120	C	217.2	0.4	2.39	3.87	19.11	0.11	**0.08**	0.01											
	86	9	2830	130	C	210.0	0.3	2.41	3.90	19.52	0.01	**0.44**	0.03											
M3	9	1	300	-	R														2.63	8.57	51.29	0.52	**0.85**	0.05
	25	2	300	-	R														2.60	8.47	49.57	0.02	**1.11**	0.07
	46	5	300	-	R									3.52	43.46	0.41	**0.78**	0.05						
	104	10	300	-	R									3.34	37.39	0.28	**0.72**	0.04						
	153	15	2690	120	C	190.5	1.9	2.32	3.72	17.28	0.15	**0.40**	0.02	3.34	37.23	0.06	**0.97**	0.06						
	157	16	3290	150	C	189.6	0.6							3.34	37.14	0.02	**0.93**	0.06						
	136	14	* -		C	189.1	0.5	2.30	3.72	17.06	0.17	**0.37**	0.02	3.33	36.90	0.09	**0.99**	0.06						
S1	57	6	* -		N	23.9	0.2												2.49	8.19	44.04	0.38	**1.06**	0.06
	65	7	2080	90	N	23.8	0.1							3.53	44.06	0.05	**0.94**	0.06	2.50	8.19	44.14	0.36	**1.01**	0.06
	67	7	2780	120	N	23.7	0.1							3.53	44.04	0.19	**0.86**	-	◀Overlup with B2 NaCl. (large uncertanty)					
S2	162	16	3970	180	N	19.0	0.0							3.36	38.03	0.04	**1.07**	0.06						
S3	46	5	2170	90	N	25.8	0.0							3.60	46.69	0.41	**0.91**	0.06						

No hatched lines, data obtained after thermally quenched to the room temperature; pink hatched lines, data obtained during laser heating; blue hatched lines, the result of the diffusion experiment that indicated the width of the miscibility gap at 46 GPa and room temperature; gray hatched lines, the result of compression experiments without thermally annealing. Note that the data in gray lines are eliminated from the phase diagrams (Figure 3.15).

[a] The letters indicate the kind of pressure scale: C, Corundum; P, pPv-Al_2O_3, R, Raman; N, NaCl.

[b] The data temperatures showed in "*" were obtained at room temperature after being thermally quenched. The phase and *x* would reflect the heating temperature rather than the room temperature. Therefore, I omitted these data in Figure 3.15 for 40–80 GPa.

[c] The volume of pPv-Al_2O_3 is obtained after being thermally quenched.

Table 3.4 Experimental results for melting experiments

Run #	Pressure (GPa)		Lower bound (K)		Upper bound (K)		Composition†	Phase
	P	Perr	T	Terr	T	Terr		
U1	62	6	1830	80	1900	80	Eutectic side	*fcc* + *hcp*
U4	44	4	N.D.		2070‡	100	Eutectic side	*fcc*
M1	173	17	3220	150	3400	160	Eutectic side	*fcc*
M2	67	7	2450	110	2720	120	Eutectic side	*hcp*
	86	9	N.D.		2421	120	Eutectic side	*fcc* + *hcp*
M3	157	16	2695	120	3291	150	Eutectic side	*fcc* + *hcp*
S1	70	7	2780	120	2900	130	Stoichiometric	*fcc*
S2	163	16	3770	170	4020	190	Stoichiometric	*fcc*
S3	46	5	N.D.		2170	90	Stoichiometric	*fcc*

†This column indicates which composition the melting experiments were performed. Eutectic side, the melting temperature around the eutectic composition; Stoichiometric; stoichiometric FeH.

‡Melting temperature was constrained by combining the 1-D temperature profiles and liquid/solid boundary determined from the SIM image.

Chapter 4. Compression of *hcp* Fe–Si–H alloys

This chapter was updated from the published article as *"Compression of Fe–Si–H alloys to core pressures" by* ***Shoh Tagawa****, Kenji Ohta, Kei Hirose, Chie Kato, and Yasuo Ohishi, Geophys. Res. Lett. 43.,* https://doi.org/10.1002/2016GL068848.

Abstract

In Chapter 4, I examined the compression behavior of hexagonal-close-packed (*hcp*) $(Fe_{0.88}Si_{0.12})_1H_{0.71}$ and $(Fe_{0.88}Si_{0.12})_1H_{0.97}$ (in the atomic ratio) alloys up to 130 GPa in a diamond-anvil cell (DAC). While contradicting experimental results were previously reported on the compression curve of *double-hcp* (*dhcp*) $FeH_{x\approx1}$ (Figure 1.2), this study showed that the compressibility of *hcp* $Fe_{0.88}Si_{0.12}H_x$ alloys is very similar to those of *hcp* Fe and $Fe_{0.88}Si_{0.12}$, indicating that the incorporation of hydrogen into iron does not change its compression behavior remarkably. This data is also applicable to estimate the compressibility of *hcp* FeH*x*, which is one of the candidates of the core material. The present experiments suggest that the inner core may contain up to 0.66 wt.% hydrogen ($FeH_{0.37}$) if temperature is 5000 K. The calculated density profile of $Fe_{0.88}Si_{0.12}H_{0.26}$ alloy containing 0.50 wt.% hydrogen in addition to geochemically-required 6.5 wt.% silicon matches the seismological observations of the outer core, supporting that hydrogen is an important core light element.

4.1 Introduction

So far, only a little is known about the effect of hydrogen on the property of iron and iron alloy (Figure 1.2). FeH_x ($x \approx 1$) is easily formed under hydrogen-saturated conditions or by using paraffin as a hydrogen source, which has been examined repeatedly by high-pressure experiments (Badding et al., 1991; Hirao et al., 2004; Kato et al., 2020; Narygina et al., 2011; Pépin et al., 2014). By contrast, there are only a few experimental studies on FeHx ($x < 1$) (Ikuta et al., 2019; Machida et al., 2019; Yamakata et al., 1992), regardless of the fact that the core density deficit is explained by FeH_x with x = 0.28–0.56 (0.50–1.0 wt.%) (Narygina et al., 2011) and $0.16 < x < 0.6$ (0.29 wt.% –1.1 wt.%) (Chapter 2 and 3). Furthermore, *hcp* Fe-H would be the most important phase structure to examine hydrogen in the inner core conditions (Chapter 3).

Other light elements could be alloyed with Fe–H in the inner core. Silicon has been considered an important light element in the core from cosmochemical and geochemical perspectives. The high Mg/Si ratio of the Earth's mantle compared to that of solar abundance suggested ~7 wt.% Si in the core (Allègre et al., 1995). Moreover, the difference in Si isotopic composition between mantle and chondrites also supports ~6 wt.% Si in the core (Georg et al., 2007; Shahar et al., 2009). Other favorable candidates, oxygen and carbon, are difficult to incorporate into the pure Fe. It would also be similar to hydrogen bearing the inner core because FeH$x_{<0.4}$ and Fe have the same crystal structure (Chapter 3).

In this study, I examined hydrogen-bearing Fe–6.5wt.%Si alloy ($Fe_{0.88}Si_{0.12}H_{0.71}$ and $Fe_{0.88}Si_{0.12}H_{0.97}$ in the atomic ratio) at high pressures in a diamond-anvil cell (DAC). The previous study on Fe–Si–H alloy was limited to the FeSi–H system at low pressures (Terasaki et al., 2011). In this paper, the hydrogenation, volume, and compression behavior of Fe–Si–H alloys are reported up to 130 GPa. I also discuss the presence of hydrogen and its abundance in the core.

4.2 Experimental Method

In order to examine the crystal structure and compression behavior of iron-rich Fe–Si–H alloys, I performed *in situ* X-ray diffraction measurements up to 130 GPa using laser-heated diamond anvil cell technique. Two sets of experiments were carried out using diamond anvils with a culet size of 120 μm (run #1) or 150 μm (run # 2). I used Re gaskets pre-indented to about 20 μm thick. So as to prevent hydrogen embrittlement of the Re gasket and the escape of hydrogen from a sample chamber, an NaCl inner gasket was prepared with a Focused Ion Beam (FIB, Versa 3D, *FEI*). The surface of the diamond anvils was coated with a thin layer of Ti by sputtering (Ohta et al., 2015). ~5 μm thick $Fe_{0.88}Si_{0.12}$ (6.5 wt.% Si) foil (99.99% purity, *Rare Metallic*) was put into the sample chamber, together with a small NaCl plate that was used as a pressure marker. A ruby ball was additionally used in run #2. I then loaded hydrogen using a liquid hydrogen introducing system at temperatures below 20 K (Chi et al., 2011). The sample and hydrogen were compressed under low temperature and subsequently restored to room temperature. A pressure-

temperature path before thermal annealing was monitored with pressure measurement using ruby (3000 ppm Cr^{3+}, *P.M.C.*) in the second run; I compressed the sample to 13 GPa at 150 K from 1.0 GPa below 80 K, and then temperature was returned to 280 K. The presence of hydrogen in the sample chamber was confirmed by Raman spectroscopy; I observed a signal from the vibron of H_2 molecules in both runs. After compression to 27 GPa (run #1) and 62 GPa (run #2) at room temperature, Fe–Si foils were heated from both sides with Yb fiber lasers for 17 and 74 mins in runs #1 and #2, respectively, in order to promote their hydrogenation. The annealing temperature was ~1000 K.

X-ray diffraction (XRD) patterns were obtained at BL10XU, SPring-8 (Ohishi et al., 2008). The incident X-ray beam was monochromatized to a wavelength of 0.4143–0.4159 Å (~30 keV) and focused to 6 μm in diameter. To collect diffraction data, I used a flat panel X-ray detector (*PerkinElmer*) with an exposure time of 1 sec. The pressure was determined from the volume of NaCl on the basis of its equation of state (EoS) for the B1 and B2 structures (Dorogokupets and Oganov, 2007). The EoS of B2 NaCl is based on the MgO pressure scale that was also used for previous experiments on $Fe_{0.88}Si_{0.12}$ (Tateno et al., 2015). In run #1, I collected XRD measurements separately for a sample and for a pressure marker in order to avoid peak overlapping above 53 GPa. I found that the pressure gradient in a sample chamber was small, at most 2 GPa through the present experiments.

4.3 Results

(1) Hydrogenation and crystal structure of Fe–Si–H

The *hcp* phase appeared at high pressure in both runs before thermal annealing (Figure 4.1). The crystal structure did not change upon thermal annealing, although volumes increased due to hydrogenation. The *hcp* phase was preserved up to 130 GPa. It contrasts the Fe–H system, in which the *dhcp* phase was formed from bcc upon compression to >3.5 GPa at 300 K (Badding et al., 1991; Hirao et al., 2004). The *dhcp* phase is distinguished from *hcp* by additional *dhcp* 011, 013, and 015 peaks, but these peaks were not found in our experiments (Figure 4.1). In run #1, a couple of *hcp* phases were observed at 27 GPa before heating. One exhibited a volume very similar to that of $Fe_{0.88}Si_{0.12}$ (Fe–6.5wt.%Si) at equivalent pressure (Tateno et al., 2015) (note that pressures in this study and *Tateno et al.* are both based on the MgO pressure scale), and the other had a larger volume because of the incorporation of hydrogen. After thermally annealing, only the single *hcp* phase was found with a volume larger than those before heating, which indicated further hydrogenation (Figure 1). The XRD data was first collected at 20 GPa in run #2, where only the single *hcp* phase was observed before heating. As described in section 3.3, the hydrogen concentrations were $Fe_{0.88}Si_{0.12}H_{0.71}$ and $Fe_{0.88}Si_{0.12}H_{0.97}$ (in the atomic ratio) in runs #1 and #2, respectively.

The XRD pattern obtained in this study showed two characteristics. Firstly, the *hcp* 002 peak was strong for Fe–Si–H (Figure 4.1), while it is known to be weak for pure Fe and iron-rich Fe–Si alloy, in which the (001) plane aligned perpendicular to a compression direction. Secondly, Fe–Si–H developed a strong preferred orientation (Figure 4.2). These suggest that hydrogenation changes the dominant slip system and the deformation mechanism of the *hcp* phase. Lattice parameters, a and c, in run #1 were shown in Figure 4.3. The slope of the a-parameter changed slightly around 54–64 GPa, and it would be ascribed to the pressure-induced H-H interactions (Meier et al., 2019), but there is no anomaly of a magnetic transition reported in Hirao et al. (2004).

(2) The hydrogen concentration in *hcp* Fe–Si–H

The hydrogen content of $Fe_{0.88}Si_{0.12}Hx$ was determined using the equation (Fukai, 1992):

$$x = [V(Fe_{0.88}Si_{0.12}Hx) - V(Fe_{0.88}Si_{0.12})]/2\Delta V_H(P) \quad \text{(eq.4.1)}$$

Using V_H from Caracas (2015) and $V(Fe_{0.88}Si_{0.12})$ for *hcp* $Fe_{0.88}Si_{0.12}$ (Tateno et al., 2015) at each pressure, the composition of the alloy synthesized in run #1 and #2 is calculated to be $(Fe_{0.88}Si_{0.12})_1H_{0.71}$ and $(Fe_{0.88}Si_{0.12})_1H_{0.97}$, respectively (Table 4.1). The error of hydrogen contents is 9.8% for run #1 and 3.1% for run #2.

It is noted that *x* was less than 1.0 in run #1 even after thermal annealing under hydrogen-saturated conditions. It suggests that the octahedral sites of the *hcp* lattice were not fully occupied by hydrogen, in contrast to the case of *dhcp* FeH_x ($x \approx 1$) (Hirao et al., 2004; Pépin et al., 2014).

(3) Compression behavior

Pressure–volume data were collected for *hcp* $Fe_{0.88}Si_{0.12}H_{0.71}$ in a pressure range from 26 to 130 GPa (run #1) and for $Fe_{0.88}Si_{0.12}H_{0.97}$ from 64 to 121 GPa (run #2) (Figure 4.3 and Table 4.1). I examined the compression behaviors of these Fe–Si–H alloys by fitting the Vinet EoS to the data;

$$P = 3K_0 \left(\frac{V}{V_0}\right)^{-\frac{2}{3}} \left[1 - \left(\frac{V}{V_0}\right)^{\frac{1}{3}}\right] \exp\left\{\frac{2}{3}\left(K_0' - 1\right)\left[1 - \left(\frac{V}{V_0}\right)^{\frac{1}{3}}\right]\right\} \quad \text{(eq. 4.2)}$$

I fixed the V_0 value from the volume of hydrogen in *hcp* FeH*x* at ambient pressure. Antonov et al. (1998) reported the volume of non-magnetic $FeD_{0.42}$ from neutron diffraction measurements. The volume difference between *hcp* iron (Dewaele et al., 2006) and *hcp* $FeD_{0.42}$ gives $V_H = 2.017$ Å^3 at 1 bar. Note that the volume of deuterium is similar to that of hydrogen (Antonov et al., 1998).

For $Fe_{0.88}Si_{0.12}H_{0.71}$ in run #1, I obtained bulk modulus at ambient condition $K_0 = 209 \pm 4$ GPa, its pressure derivative $K_0' = 4.36 \pm 0.1$, and volume at 1 bar $V_0 = 25.35$ Å^3 per *hcp* unit-cell. In run #2, I found $K_0 = 216 \pm 4$ GPa, its pressure derivative $K_0' = 3.94 \pm 0.2$, and volume at 1 bar $V_0 = 26.39$ Å^3 per *hcp* unit-cell for $Fe_{0.88}Si_{0.12}H_{0.97}$ (Table 4.2).

The compression behavior of these $Fe_{0.88}Si_{0.12}H$*x* alloys is found to be different from that of FeH_x ($x \approx 1$) examined in two previous experimental studies (Figure 4.4). Hirao et al. (2004) reported that FeH_x became much stiffer than iron after the transition to a non-magnetic state (>50 GPa), while the more recent work by Pépin et al. (2014) showed FeH_x is more compressible than

iron up to 136 GPa. The data on $Fe_{0.88}Si_{0.12}H_x$ demonstrates that its compression behavior is very similar to that of pure iron (Dewaele et al., 2006) and $Fe_{0.88}Si_{0.12}$ (Tateno et al., 2015) (Figure 4.4), although Fe–Si–H alloys have larger K_0 but smaller K_0'. The volume difference between $Fe_{0.88}Si_{0.12}$ and $Fe_{0.88}Si_{0.12}H_{0.71}$ is 15.2% at 135 GPa and 13.7% at 300 GPa.

4.4 Discussion: Fe–Si–H alloy in the core?

The densities of silicon/hydrogen-bearing iron alloys are estimated for both inner and outer core conditions using the EoS parameters obtained for $Fe_{0.88}Si_{0.12}H_{0.71}$ and $Fe_{0.88}Si_{0.12}$ listed in Table 1. Here I consider isentropic temperature profile for the outer core, which is given by;

$$T = T_{\mathrm{ICB}} \left(\frac{\rho}{\rho_{ICB}}\right)^{\gamma} \quad \text{(eq. 4.3)}$$

where ρ is density and γ = 1.5 is Grüneisen parameter (Vočadlo et al., 2003). The thermal expansivity of Fe–Si–H is assumed to be the same as that for iron reported by Dewaele et al. (2006). I first calculated the hydrogen concentrations that match the densities observed for the inner and outer core sides of the ICB (Dziewonski and Anderson, 1981) when the temperature is 5000 K (Hirose et al., 2013). The results show that the maximum amount of hydrogen in the inner core is 0.66 wt.% ($FeH_{0.37}$ in the atomic ratio). On the other hand, if silicon is a single light element, the inner core density is explained by $Fe_{0.90}Si_{0.11}$ (5.8 wt.% Si). Considering geochemically proposed 6.5 wt.% Si for the outer core (e.g., Georg et al., 2007; Shahar et al., 2009), $Fe_{0.88}Si_{0.12}H_{0.26}$ was obtained (0.50 wt.% H). In these calculations, I assumed ideal volume mixing

between $Fe_{0.88}Si_{0.12}$ and $Fe_{0.88}Si_{0.12}H_x$. While solid data are used for these calculations for the outer core, previous shock-wave compression experiments (Brown and McQueen, 1986) and *ab initio* calculations (Ichikawa et al., 2014) reported that the volume difference between solid and liquid iron is about 2% at the outer core pressure range. Nevertheless, such a difference is indeed comparable to the resolution of density determinations from seismological observations. (Masters and Gubbins, 2003) argued that the resolution is no better than 1% when averaged over a depth width of 270 km in the lowermost outer core, suggesting that the uncertainty in the outer core PREM density is larger than 1.6% near the ICB.

The densities of $Fe_{0.90}Si_{0.11}$ / $FeH_{0.37}$ and $Fe_{0.88}Si_{0.12}H_{0.26}$ were then calculated over the entire inner and outer core pressure range, respectively, along the isentropic temperature curve with the ICB temperature of 5000 K. The compressibility of these alloys is in good agreement with the PREM density profile for both inner and outer cores (Figure 4.5). The deviation is only 0.14% in the outer core pressure range. Additionally, the hydrogen contents and the density profiles of Fe–Si–H alloys were also estimated at higher ICB temperatures of 5500 and 6000 K (Figures 4.6 and 4.7). The consistency between these calculated density profiles and the PREM values did not change even in the higher temperature profiles because the deviation is up to 0.20%. Talking EPOC (Irving et al., 2018) as a reference model, $Fe_{0.88}Si_{0.12}H_{0.18}$ can reconcile its density profile when T_{ICB} is 5000 K and the deviation is 0.38% in the outer core pressure range.

The calculation is also available to estimate the maximum contents of hydrogen of the outer core. Considering that hydrogen is the sole light element, it was yield to 1.18 wt.% when T_{ICB} is 5500 K and 1.24 wt.% when T_{ICB} is 5000 K, respectively. Although this estimation is slightly larger than the result in the previous *ab initio* calculation (1.02 wt.% H when T_{ICB} is 5400 K) (Umemoto and Hirose, 2015), it provides better constraint than the results from previous experimental studies. Note that the EoS of Pépin et al. (2014) would be affected by the magnetic transition of FeH and became softer, extrapolating to high pressures; performing the same calculation using its EoS, the maximum hydrogen contents is 1.46 wt.% when T_{ICB} is 5500 K.

In addition to silicon, sulfur could be incorporated into the inner core material, while carbon and oxygen are minor. Alfé et al. (2002) argued that sulfur and silicon are not partitioned between the outer core and the inner core and Mori et al. (2017) confirmed that liquid Fe + 5.7 wt.% S coexisted with 3.9 wt.% S at 254 GPa. On the other hand, the behavior of oxygen and carbon is the opposite. Ozawa et al. (2010) reported that oxygen is hardly soluble in solid Fe (<0.1 wt.% at the ICB conditions), and Mashino et al. (2019) showed that the maximum solubility of carbon in solid *hcp* iron was lower than 1 wt.% above 200 GPa. The effect of the alloying of sulfur on the compressibility of *hcp* FeH*x* would be similar to that of silicon (Sata et al., 2010). Therefore, *hcp* Fe-H-X is feasible as an inner core material, which well reconciles the density profile of PREM.

Figures and tables

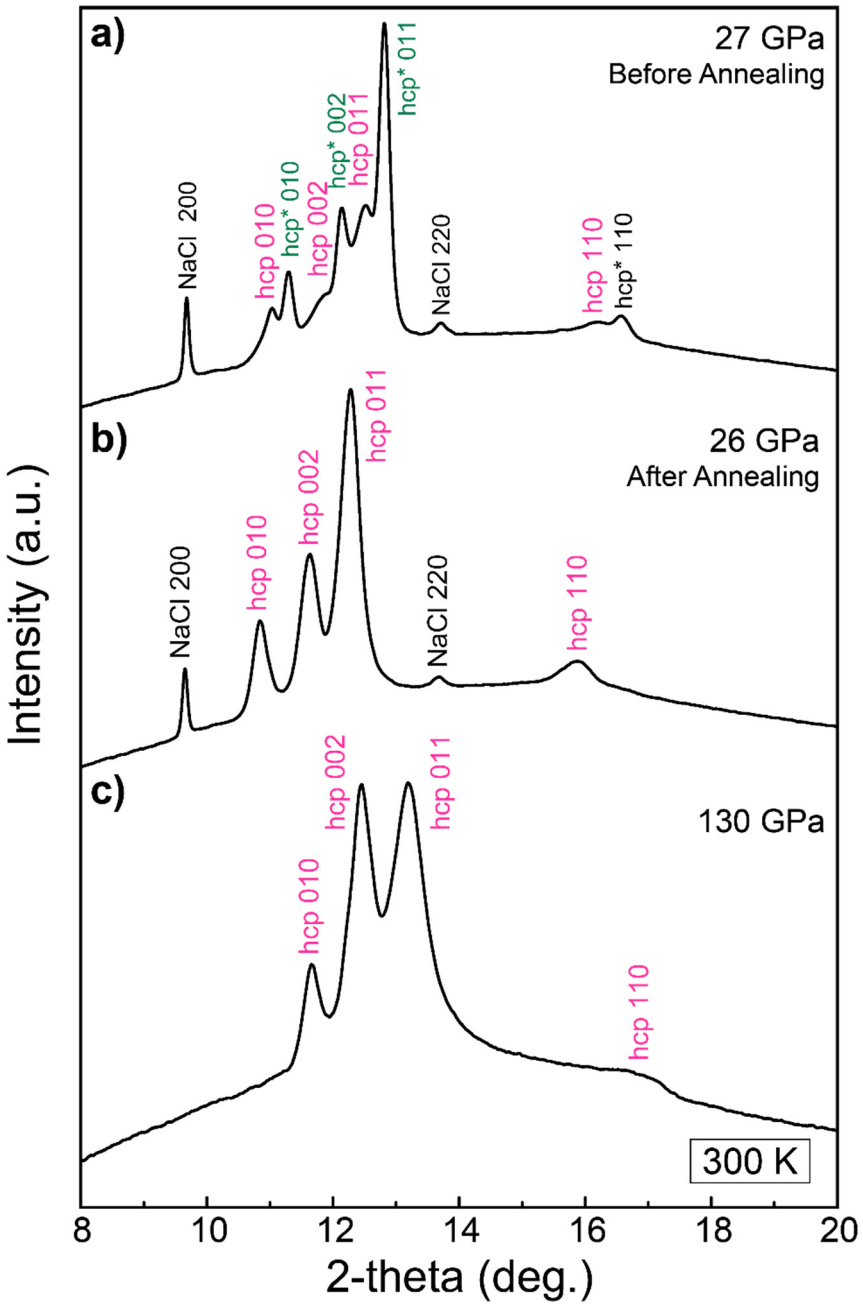

Figure 4.1 Integrated XRD patterns collected at room temperature during run # 1
Before (a) and after (b) thermally annealing at around 26 GPa, and c) at 130 GPa, which was the highest pressure condition in this study. Two *hcp* phases were found in (a; *hcp* marked with green text, almost no hydrogen Fe-Si; marked with pink text, Fe-Si-H) before thermal annealing, and they became single upon heating (b; marked with pink Fe-Si-H). Note that the wavelength of the incident X-ray beam was 0.41426(8) Å (~30 keV).

Figure 4.2 Two-dimensional XRD pattern of *hcp* $Fe_{0.88}Si_{0.12}H_{0.71}$ at 130 GPa.

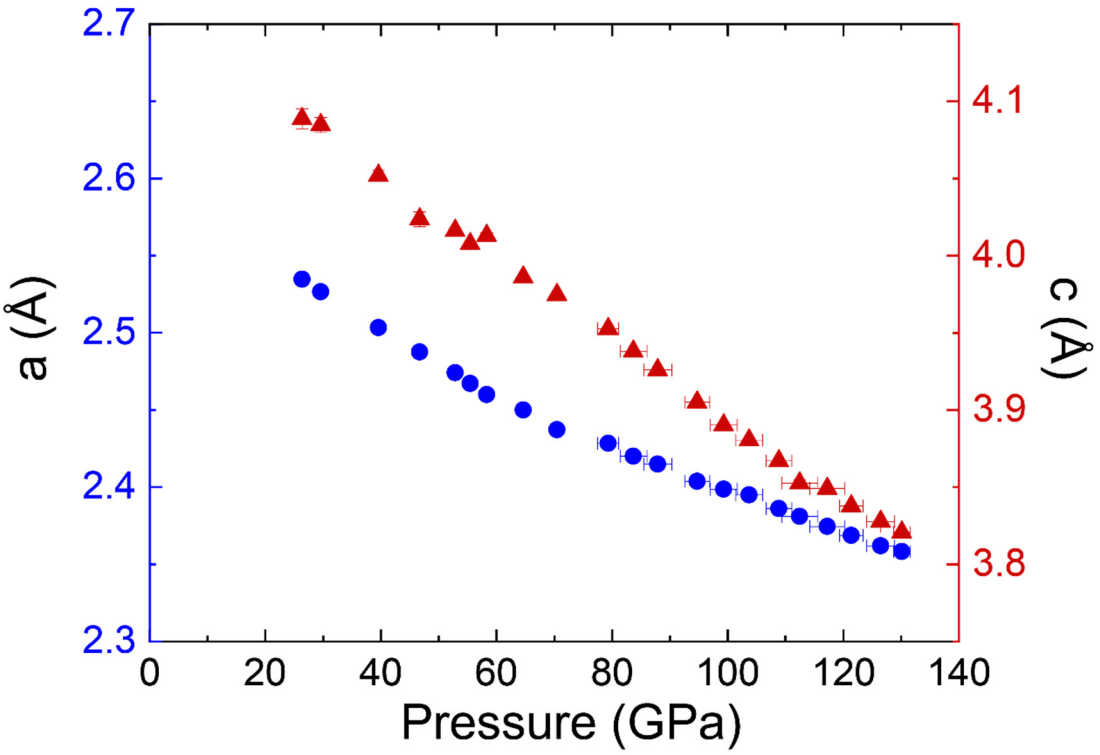

Figure 4.3 Changes in lattice parameters of *hcp* $Fe_{0.88}Si_{0.12}H_{0.71}$ observed in run #1

Both a- and c-parameters exhibit anomalous behavior around 60 GPa, possibly due to electronic topological transition (Glazyrin et al., 2013; Meier et al., 2019) or isostructural magnetic collapse (Antonangeli et al., 2008). The latter is less likely because the volume compression curve does not show any anomalies (Figure 4.4).

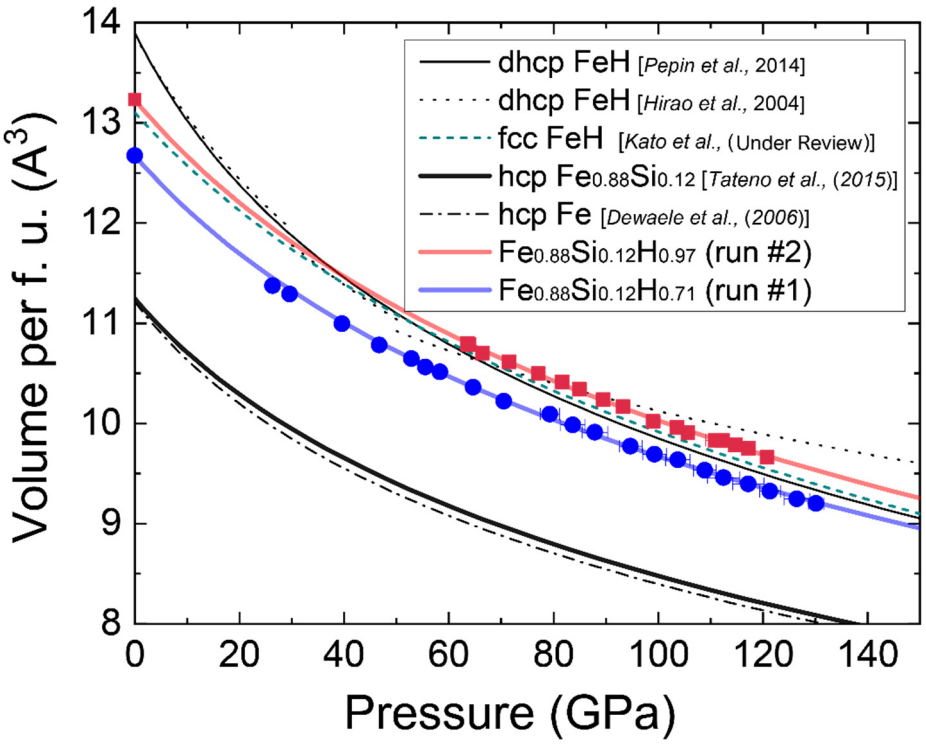

Figure 4.4 Compression curves of *hcp* $Fe_{0.88}Si_{0.12}Hx$

Symbols and solid color lines show experimental data for *hcp* $Fe_{0.88}Si_{0.12}H_{0.71}$ (blue, run #1) and $Fe_{0.88}Si_{0.12}H_{0.97}$ (red, run #2). Previous data on *dhcp* FeH by Hirao et al. (2004) (black dotted curve) and by Pépin et al. (2014) (thin solid curve), and *fcc* FeH by Kato et al. (2020) (green dotted curve) are given for comparison. The compression curves of *hcp* Fe (dash-dot curve) (Dewaele et al., 2006) and $Fe_{0.88}Si_{0.12}$ (thick solid curve) (Tateno et al., 2015) are also shown as references. Half of the unit-cell volume is given for *dhcp* FeH.

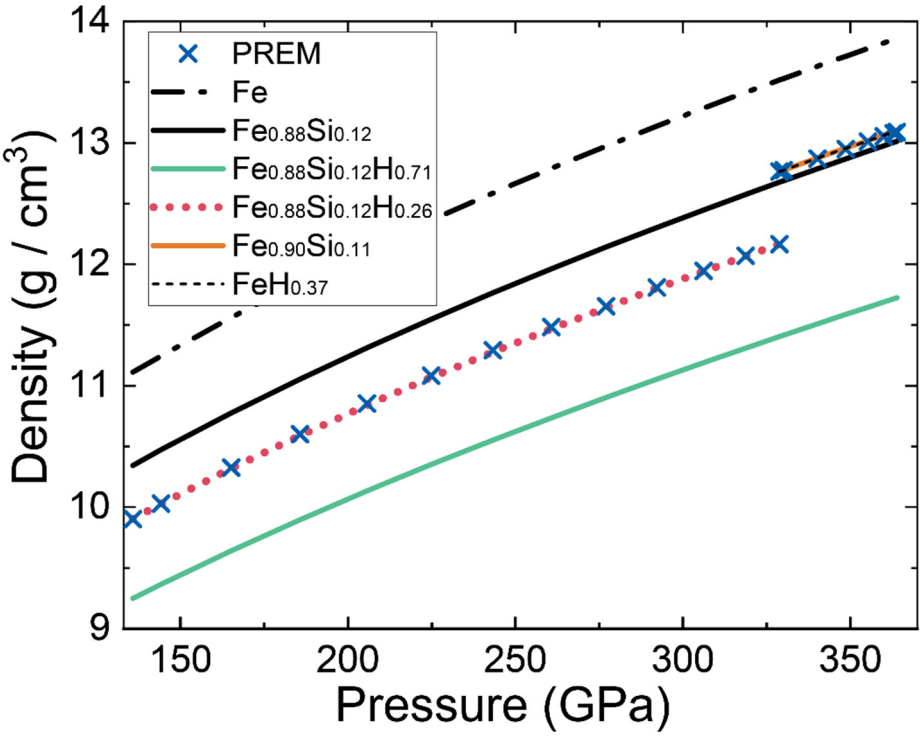

Figure 4.5 Comparison of the density of $Fe_{0.88}Si_{0.12}H_{0.26}$ alloy along the isentropic temperature profile (T_{ICB} = 5000 K) with the PREM density

The density of $Fe_{0.88}Si_{0.12}H_{0.26}$ is shown in the red dotted curve and the PREM density is indicated in cross marks. The density profiles of Fe (Dewaele et al., 2006) (dash-dot curve), $Fe_{0.88}Si_{0.12}$ (Tateno et al., 2015) (black solid curve) and $Fe_{0.88}Si_{0.12}H_{0.71}$ (this study, run #1, solid green curve) are also shown. The densities of $Fe_{0.90}Si_{0.11}$ and $FeH_{0.37}$ match the PREM value for the inner core.

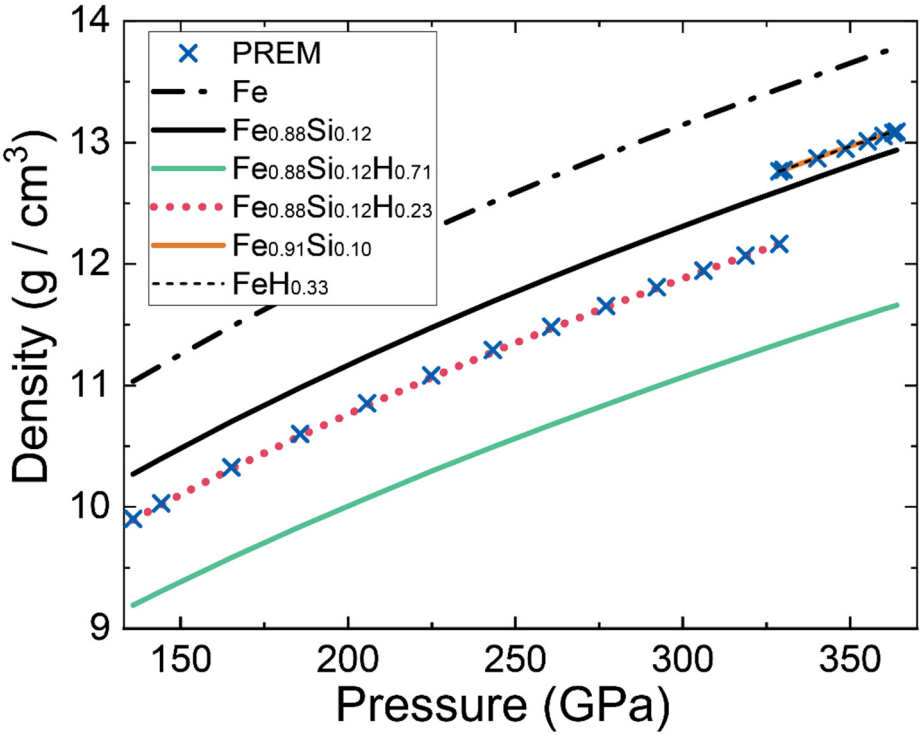

Figure 4.6 Comparison of the density of Fe–Si–H alloys along isentropic temperature profile (T_{ICB} = 5500 K) with the PREM density.

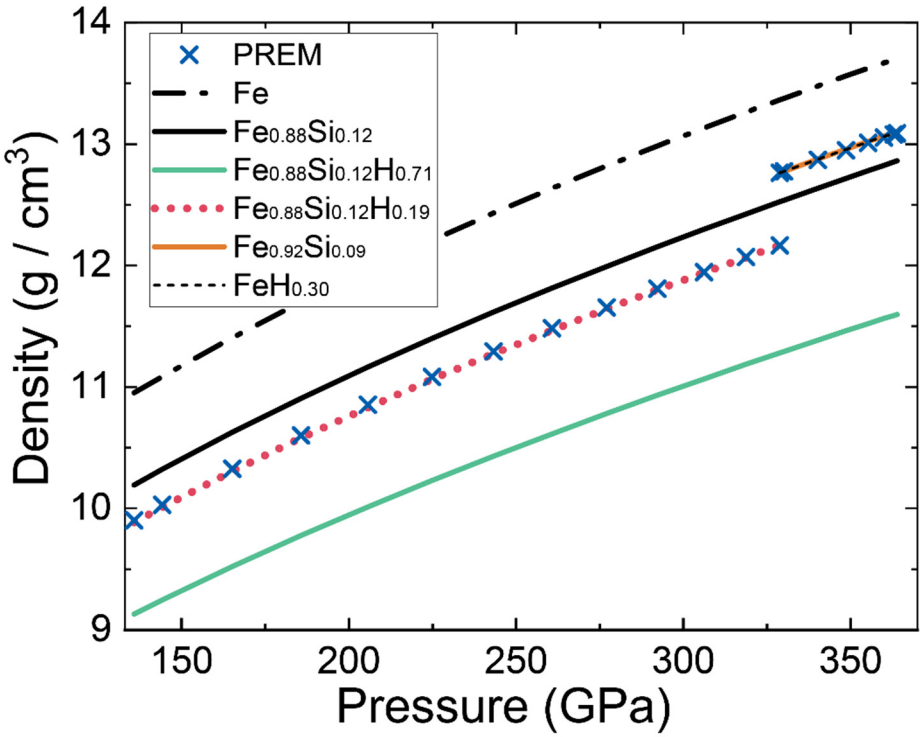

Figure 4.7 Comparison of the density of Fe–Si–H alloys isentropic temperature profile (T_{ICB} = 6000 K) with the PREM density.

Table 4.1 Experimental results of compression of *hcp* Fe–Si–H alloys

			NaCl				$Fe_{0.88}Si_{0.12}Hx$		
Run	V (Å^3)	±V (Å^3)	Dorogokupets & Dewaele (2007) Pressure (GPa)	±P (GPa)	Sata et al. (2002) Pressure (GPa)	±P (GPa)	Volume (Z=2) (Å^3)	±V (Å^3)	$x^{\dagger}$
	119.02	0.10	26.3	0.1	25.6	0.1	22.75	0.07	0.66
	116.11	0.06	29.6	0.1	28.6	0.1	22.58	0.05	0.68
	26.01	0.01	39.6	0.0	38.9	0.0	21.99	0.03	0.71
	25.05	0.03	46.7	0.3	45.7	0.3	21.56	0.05	0.71
	24.33	0.00	52.8	0.0	51.7	0.0	21.29	0.02	0.73
	24.05	0.01	55.5	0.1	54.4	0.1	21.12	0.01	0.72
	23.76	0.00	58.3	0.0	57.3	0.0	21.03	0.02	0.74
	23.16	0.01	64.7	0.1	63.7	0.1	20.72	0.00	0.74
	22.66	0.02	70.5	0.2	69.8	0.2	20.45	0.01	0.74
	21.98	0.13	79.3	1.8	79.3	2.0	20.19	0.01	0.78
1	21.67	0.16	83.7	2.3	84.1	2.5	19.97	0.01	0.76
	21.39	0.16	87.9	2.4	88.7	2.7	19.83	0.01	0.77
	20.96	0.13	94.7	2.2	96.3	2.5	19.54	0.00	0.76
	20.69	0.13	99.3	2.3	101.6	2.6	19.38	0.00	0.76
	20.44	0.12	103.7	2.3	106.6	2.7	19.27	0.01	0.78
	20.17	0.11	108.9	2.2	112.6	2.6	19.07	0.01	0.77
	19.99	0.15	112.5	3.1	116.8	3.7	18.92	0.02	0.75
	19.75	0.14	117.2	3.0	122.5	3.6	18.79	0.01	0.76
	19.56	0.09	121.4	2.0	127.5	2.5	18.65	0.00	0.72
	19.33	0.11	126.5	2.4	133.6	3.0	18.50	0.00	0.67
	19.17	0.06	130.2	1.4	138.1	1.8	18.40	0.01	0.65
	23.26	0.04	63.6	0.5	62.6	0.5	21.59	0.05	0.98
	23.24	0.04	63.8	0.5	62.9	0.5	21.57	0.00	0.97
	23.00	0.04	66.5	0.4	65.6	0.4	21.41	0.04	0.96
	22.58	0.03	71.5	0.3	70.9	0.3	21.23	0.07	0.98
	22.14	0.03	77.1	0.4	76.9	0.4	21.00	0.10	0.99
	21.81	0.05	81.7	0.7	81.9	0.8	20.83	0.08	1.00
	21.58	0.05	85.0	0.7	85.5	0.8	20.68	0.08	1.00
	21.29	0.06	89.5	0.9	90.5	1.1	20.47	0.11	0.99
2	21.05	0.06	93.3	1.0	94.7	1.1	20.33	0.11	0.99
	20.71	0.08	99.0	1.3	101.2	1.5	20.04	0.11	0.97
	20.45	0.05	103.6	0.9	106.5	1.0	19.92	0.10	0.98
	20.34	0.05	105.7	0.9	108.9	1.1	19.82	0.08	0.97
	20.07	0.09	110.9	1.8	115.0	2.1	19.66	0.10	0.98
	19.99	0.05	112.4	0.9	116.7	1.1	19.65	0.03	0.99
	19.87	0.06	114.8	1.2	119.6	1.4	19.57	0.03	0.99
	19.75	0.04	117.3	0.9	122.6	1.1	19.50	0.07	0.99
	19.58	0.04	120.8	1.0	126.8	1.1	19.32	0.09	0.94

† Calculation results of $x = \frac{[V(\mathrm{Fe_{0.88}Si_{0.12}H}x) - V(Fe_{0.88}Si_{0.12})]}{2V_H(\mathrm{P})}$. The average of the maximum and minimum x of each run yields the hydrogen content of the samples, 0.71 for run #1 and 0.97 for run #2.

Table 4.2 EoS parameters for $Fe_{0.88}Si_{0.12}Hx$ and related alloys

	Unit Cell V_0 (Å^3)	K_0 (GPa)	K_0'	EoS[a]	
			hcp Fe–Si–H[b]		
$Fe_{0.88}Si_{0.12}H_{0.71}$	25.35(fix)	209(4)	4.36(13)	V	This study
$Fe_{0.88}Si_{0.12}H_{0.97}$	26.39(fix)	216(4)	3.94(16)	V	This study
			dhcp $FeH_{x\approx1}$		
	50.76[c]	182(45)	8.5(2.9)	BM	Hirao et al. (2004) (≥ 50 GPa)
	55.60(20)[c]	131.1(3.0)	4.83	V	Pépin et al. (2014)
			fcc $FeH_{x\approx1}$		
	53.8 [c]	99	11.7	BM	Narygina et al. (2011)
	52.4 [c]	227	3.4	V	Kato et al. (*under review*)
			hcp FeH_x		
$FeH_{0.5}$	23.57	244.2	4.277	BM	Caracas (2015)
$FeH_{1.0}$	25.97	224.8	4.203	BM	Caracas (2015)
			hcp Fe–Si		
$Fe_{0.88}Si_{0.12}$	22.49	181.5	4.90	V	Tateno et al. (2015)[d]
			hcp Fe		
Fe	22.43(10)	163.4(7.9)	5.38(16)	V	Dewaele et al. (2006)

[a] V, Vinet; BM, third order Birch–Murnaghan.

[b] In published work, the EoS parameters were slightly different because of the difference for the pressure marker and V_H.

[c] Z = 4.

[d] Pressure was recalculated using MgO pressure scale by Dorogokupets & Dewaele (2007)

Chapter 5. General discussion

This chapter aims to verify a geochemical consistency of hydrogen existing in the Earth's core and discusses core compositions by integrating these new findings. First, I will test the consistency of the hydrogen-rich core with a more realistic core formation model and discuss the water accretion scenarios. Then, I will constrain this to the present composition of the Earth's core. Then, I will note future perspectives related to this dissertation.

5.1 Consistency with core formation models

The single-stage core formation model, which I applied in Chapter 2, provides a useful shorthand for the accretion history, and it is the simplest way to estimate the hydrogen content in the core. However, a more realistic model can draw a more concrete conclusion. Here, I tested the hydrogen distribution of the proto-Earth on a widely accepted continuous core formation model, based on the geochemical models constructed by trace element and isotopic compositions.

The recent publications by Siebert et al. (2012, 2013) found a plausible core formation pressure, temperature, and fO_2 pathway that would reproduce the trace element abundances of the Earth. They performed high-pressure metal-silicate partitioning experiments for V and Cr, in addition to Ni and Co, and found that terrestrial accretion under oxidizing conditions explains the mantle residue of these elements. Badro et al. (2015) refined the formulation and provided P-T-fO_2 paths and Si and O content in the core as the function of Earth's accretion mass. The model

considers accretion of planetesimals (~ 1/1000 M_E, the Earth's mass) that fully equilibrate with the magma ocean upon impact.

This model assumes that the core formation occurs at the base of the magma ocean (Figure 5.1). A detailed explanation for the model was provided in the supplementary materials by Dauphas (2017). The equilibration pressure, $P_{E.}$ in each step, is defined as $P_{E.} = P_{final} \times f^{2/3}$, where f is the mass fraction of the core and mantle of that step, and P_{final} is the final pressure of the magma ocean when the core formation ended. The pressure increase in the silicate part was approximated linearly with depth. A silicate part from $P>P_E$ to the CMB pressure is solidified as a solid mantle. Also, assuming constant density in the magma ocean, although it is a rough assumption, the mass fraction of the magma ocean (M_{MO}) is written as;

$$f_{\mathrm{MO}} = \frac{\mathrm{M_{MO}}}{\mathrm{M_{BSE}} - \mathrm{M_{MO}}} = \frac{6371^3 - \left(6371 - 2886 * \frac{\mathrm{P}_{final}}{135}\right)^3}{6371^3 - 3485^3}$$

The mass fractions of the metal in the planetesimals, which is the impactor, and in the proto-Earth of each step are fixed at 0.325.

The temperature of the base of the magma ocean, T_E has to lie near the solidus or liquidus temperature of the mantle. T_E also represents the condition of the core formation at each step. Badro et al. (2015) found a likely result to explain the trace element abundance considering that the evolution of T_E is along the liquidus curve, according to Fiquet et al. (2010): P_{final} is 60 GPa, and fO_2 changes from a high to the present-day value. The pressure and temperature evolution in

this model are indicated in Figure 1.5 and Figure 2.13. Note that fO_2, oxygen fugacity, was defined as $\Delta IW = 2\log_{10}\left(x_{FeO}^{silicate}/x_{Fe}^{metal}\right)$, where $x_{FeO}^{silicate}$ and x_{Fe}^{metal} are mole fractions of FeO in magma ocean and Fe in impactor metal, respectively. The composition evolution of Si and O in the core, and FeO in the magma ocean is shown in Supplementary Table 2 in Badro et al. (2015).

Following the model, I calculated the hydrogen partitioning along with the pressure, temperature, core composition, and redox condition path. In order to simplify the model, I assumed that Earth was iteratively accreted in N=100 steps, and the mantle composition, other than FeO, is the same as the KLB-1, independent of the accretion materials. Furthermore, Ni + Cr in the core is fixed to 6 wt.%, which is the plausible average value of the core's formation and the present Earth (Rubie et al., 2015). The other trace elements in the core were ignored in the calculation because they should be lower than 0.5 wt.%. Besides, the partitioning of elements between the magma ocean and mantle, other than water, was also ignored. For water, I assumed that there was no water in the solidified mantle.

Water in the magma ocean could affect the liquidus temperature of pyrolite, but it should be minor, according to the effect of water on the phase diagram of KLB-1 (Iwamori, 1998). Also, the water did not change the metal-silicate partitioning coefficient of the trace elements, such as Ni and Co, (Righter and Drake, 1999). The model by Badro et al. (2015) was based on the core formation under oxidized conditions, so it would be feasible for a water-bearing magma ocean.

Then, I performed the mass balance calculation with the partitioning coefficient of hydrogen obtained in Chapter 2 in each impact step. At first, I used the lower limit of the remnant water content of the "BSE" at the end of core formation, 687 ppm, as a constraint of the model (Hirschmann 2016; see in the discussion in Chapter 2, BSE = atmosphere + ocean + mantle). It yields the results in Figure 5.2. The final hydrogen concentration of the Earth's core could take on any values between 0 and 1 wt.%. Note that it would be difficult to exclude the possibility that there is no hydrogen in the Earth's core, completely. If the water-bearing materials were delivered at the final of 10% of the Earth, the hydrogen content of the water is limited to 0.1 wt.%. Moreover, the water in BSE was only originated from the later accretion of water-bearing materials in the stage of LHB (Gomes et al., 2005), and no hydrogen is in the core (see the path 3 in Figure 5.2).

However, it is unlikely that no water was brought during the core formation. In the following discussion, the water concentration of the Earth's building block was chosen as a constraint of models rather than the remnant water amount in the BSE. First, I consider the composition model of the Earth proposed by Dauphas (2017), which tested a path that could also explain the isotopic character of the Earth. The evolution of $\Delta^{17}O$, $\varepsilon^{48}Ca$, $\varepsilon^{50}Ti$, $\varepsilon^{54}Cr$, $\varepsilon^{64}Ni$, $\varepsilon^{92}Mo$, $\varepsilon^{100}Ru$, and $\mu^{142}Nd$ during the core formation were calculated to find the building blocks of the Earth and their accretion timing. The four classes of primitive chondrite, enstatite (EC), ordinary (OC), and carbonaceous chondrites (CI and CO/CV), were assumed as first components.

The best fit mixture of these materials accreted to the Earth shows that the first 60% of the accretion consists of 51% (31–79%) EC, 40% (16–55%) OC, 0% (0–5%) CI, and 9% (4–11%) CO/CV (weight fraction) and then for the latter 40% of the Earth's growth, almost EC was brought about. Note that the figures in parentheses show the possible range of the fraction of each component, which is presented as a study using the same calculation code (Brasser et al., 2018).

The water content of OC was chosen as 0.9 wt.% (Alexander et al., 2012). The water content of CO/CV during the proto-solar system should be larger than the present value (e.g., Marrocchi et al., 2018). In this work, I assumed that it is represented by the initial value of CV, 8.1 wt.% water (Alexander, 2019). Using these values, the material brought to proto-Earth in the first 60% of its mass contains 1.09 wt.% water, while dry materials like E-chondrite are delivered for the last 40%. This is equal to 28.4 times ocean mass of water (OM) delivered as a total. Taking these values, the core's final hydrogen content is 0.20 wt.%. Besides, considering the highest water concentration in Dauphas's model, 55% OC, 5% CI, and 11% CO/CV as the composition of the first 60% of the accretion material, the hydrogen amount in the core is 0.55 wt.%.

On the other hand, Braukmüller et al. (2019) proposed a more CI-rich composition. This study compared the volatile element depletion pattern of C chondrites with the bulk silicate Earth and concluded that the Earth would consist of more than 10 wt.% CI-like materials. If the Earth's forming materials consist of 10% of CI chondrite and the rest is E chondrite, it yields 0.91 wt.%

hydrogen in the core. This model seems feasible for the present Earth, but maybe too oxidized because the FeO content in the mantle is likely to excess 8 wt.%.

Except for the extreme case, hydrogen could be a dominant light element in the core. Although it is needed to test more models with a broad parameter range, its tendency would not change (e.g., Figure 2.13). Furthermore, Olson and Sharp (2019) pointed out that during the first 5 myr of the Earth's formation, >10 ocean mass of water could be sustained in the magma ocean due to the ingassing from the nebular gas. The proto-Earth would have grown to ~0.4 M_E mass at that time (e.g. Rubie et al., 2015). So, the hydrogen amount in the core could be significant.

5.2 Composition model of the Earth's core

If hydrogen is the predominant light element in the Earth's core, which combination of the elements could explain the composition of the Earth's core? I summarized the available area of each ternary Fe-H-X system of the core compositions (Figure 5.3, values for other than hydrogen is available in Table 1.2. The eutectic points and the maximum contents of the hydrogen are obtained from the Chater 3 and 4 of this study). Because of the eutectic compositions, the Fe-H-O system has a broad region of the possible area as a composition model of the core.

It is consistent with the scenario of hydrogen in the core because the hydrogen brought to the proto-Earth likely in the form of water. Oxygen should also have dissolved into core metals during core segregation in a wet magma ocean as a consequence of the reaction between H_2O and

metallic Fe, $H_2O^{silicate} + xFe^{core} \rightarrow 2H^{core} + (1\text{-}x)O^{core} + xFeO^{silicate}$.

The exchange coefficient K_D^O for the metal-silicate partitioning of oxygen, $FeO^{silicate} = Fe^{metal} + O^{metal}$ (Chapter 2, Fischer et al., 2015, Hirose et al., 2017), indicates 1.1–1.9 wt.% of O in metals at the conditions of core-mantle equilibration in the single-stage model. Earlier first-principles calculations demonstrated that liquid Fe-O alloy is also compatible with seismological observations of the outer core (Badro et al., 2014). A combination of 0.29–0.53 wt.% H (Chapter 2) and 1.1–1.9 wt.% O in the liquid core explains 50–80% of the core density deficit and the velocity excess. Note that incorporation of such amounts of H and O into the core suggests that 1.2–6.1 wt.% FeO was added to the magma ocean. Therefore, up to 3/4 of FeO included in the present-day mantle (pyrolite) may have originated from metallic Fe. The incorporation of hydrogen into the core could control the FeO/Fe ratio of the bulk Earth (Righter et al., 2014).

If oxygen is the primary light element in the core, it limits the Si contents of the core because of the exsolution of SiO_2 (Hirose et al., 2017). If the initial contents of oxygen are the same as the result by Badro et al. (2015) the present core contains 1.3–2.2 wt.% Si and 1.5–2.3 wt.% O, after the SiO_2 crystallization, which explains ~40% of the core density deficit (CDD) (max 9.5% for Si and max 8.6% for O in the core according to Umemoto and Hirose, 2020). Although up to 1.9 wt.% sulfur could exist in the core (McDonough, 2014; Suer et al., 2017), hydrogen allocates ~45% of the CDD in the core. Carbon contents in the core should be minor

not only because of the geochemical constraints (Wood et al., 2013) but also the mutual exclusively with hydrogen (Hirose et al., 2019). In this study, I proposed the preferable composition of the light elements in the outer core as 1) 0.43 wt.% H, 1.3 wt.% Si, 2.3 wt.% O, 1.9 wt.% S and no C (O-rich model) or 2) 0.45 wt.% H, 2.2 wt.% Si, 1.5 wt.% O, 1.9 wt.% S and no C (Si-rich model: this composition model neglect the constraint by Ozawa et al. (2016)). Density and Vp of the models were calculated following the method in Umemoto and Hirose (2020). Both of the models well explain the density and V_P of PREM (Figure 5.4)

The core possibly contains only Si-O-S and no H and C if the Earth was formed from almost dry materials and without the nebular gas. However, considering the crystallization of SiO_2 (Hirose et al., 2017) and the maximum contents of Si, O, and S (Umemoto and Hirose, 2020; Suer et al., 2017), only two outer composition models could be possible under this assumption;

A) >7 wt.% O & <1 wt.% Si & 2 wt.% S, B) >10 wt.% Si & <0.5wt.% O & 2 wt.% S

However, I consider that both of the composition models are unlikely. If the core composition is (A), the core formation was started in $\Delta IW = -0.6$ (Badro et al., 2015), which is really oxidized. However, such materials are typically C or O chondrite and contain a substantial amount of water (Doyle et al., 2019). The core composition (B) cannot explain the Si/Mg ratio of the present Earth (Allègre et al., 1995) because of the excess of Si amount. Therefore, hydrogen is a feasible major light element in the Earth's core.

5.3 Future perspectives

In this section, I will summarize essential further studies related to this dissertation.

(1) Can hydrogen explain the lower V_S and anisotropy of V_P in the inner core?

The low V_S in the solid inner core is the most critical problem for the quest to determine the light elements because it is substantially slower than that of Fe alloys, and no composition model agrees. So far, ideas such as the incorporation of carbon (Chen et al., 2014; Li et al., 2018) and "premelting" effects (Martorell et al., 2013) were proposed, but it is still an open question.

Hydrogen could lower the V_S of iron alloys. At high temperatures, hydrogen atoms in *hcp* FeH*x* would behave like a fluid (Fukai and Sugimoto, 1985). Such fluid-like behavior of hydrogen weakens the bonds between the iron atoms and could decrease the *G* and then V_S of Fe–H–X alloys, which would bring about a similar effect to "premelting" (Martorell et al., 2013). It should be tested experimentally and theoretically (more discussion was in the Appendix).

Furthermore, other criteria such as anisotropy of V_P in the inner core and mutual interactions between hydrogen and other light elements should be examined as future studies.

(2) Direct observation of hydrogen in FeH alloys

The method to calculate the hydrogen content in FeH*x* should be improved. I obtained the hydrogen content of samples by the lattice expansion of iron, but this method is indirect and could be improved. One crucial way is neutron diffraction measurements for FeH*x* using a

diamond anvil cell. Although a large sample volume, about 100 times larger than a usual one, is necessary for the measurement, a new design DAC with a large volume sample was reported to have reached 94 GPa (Boehler et al., 2013) and was served to the measurement. Using the technique, the pressure and temperature dependence of the volume of interstitial hydrogen should be established. Besides, neutron scattering would obtain the dynamics of a hydrogen atom in iron lattice. To reveal the relationship between its diffusion and V_S would be essential work because hydrogen could weaken a bond of Fe atoms. Also, the technical improvement of SIMS measurement on a DAC sample for FeH*x* and water-bearing silicate is necessary. There is a broad potential to reveal open questions.

(3) Timing and origin of the water

Hydrogen's partitioning coefficient could constrain the timing of the water delivery. For example, even if a lot of the water delivered in the later stage of the core formation the amount of hydrogen in the core does not increase. Then, 10 to 100 times seawater achieving only to the mantle and then it could be a planet with a massive amount of ocean. So water delivery likely occurs in the early stage of the Earth formation if hydrogen is the major light element of the Earth's core. The study combining the large metal-silicate partitioning coefficient of hydrogen, and planetary formation theory would be looked for.

Some planetary formation theories could bring a vast amount of water in the early stage.

Some scenario like "Pebble accretion model" which suggests that meter-sized pebbles fell toward the region where the terrestrial planet formed in the early protoplanetary disk (Sato et al., 2016), or Jupiter and Saturn's rapid gas accretion model, which some extended amount of the water delivered the first <500 kyr of the Earth formation, support the hydrogen is in the core.

Note that the oxidation of a hydrogen-rich atmosphere could be a more critical mechanism to bring hydrogen into the core, although previous studies assume it is minor. Because the core absorbs almost water in the early stage of formation, the D/H ratio of the Earth could only reflect the latter half of the water delivery (Figure 5.5).

(4) Low D/H ratio of the deep mantle

A recent study reveals that ocean island basalts (OIB) from a deep reservoir shows a lower D/H ratio (Hallis et al., 2015). The paper concluded that the primordial water affected by the nebular gas was preserved in Earth's deep mantle. However, it could be that hydrogen escaped from the core if the core has a low D/H ratio. This is because the D_H becomes smaller at high pressures. By extrapolating the K_D obtained in Chapter 2 to 3700 K, 136 GPa and $\Delta IW = -4.5$, $D_{H,mol}$ is 38, although it could be more reductive (Righter et al., 2014). $D_{H,mol}$ become smaller if the CMB temperature was decreased during the Earth's history. A slight amount of hydrogen returned to the bottom of the mantle if there is a small portion of liquid silicate. Therefore, the low D/H found in OIB could be the signature of the core affected by hydrogen from the nebula.

(5) Direct observation of hydrogen in the core -Neutrino oscillations-

Neutrino oscillations are strongly affected by the effective proton-to-nucleon (Z/A) ratio. Hydrogen (^{1}H) is the only nucleus that doesn't have a neutron. Therefore, its incorporation into the core changes the Z/A ratio of the core material. Neutrino oscillation tomography with large and high-sensitivity next-generation detectors could enable us to confirm the hydrogen content in the core after observation for the next several decades (Bourret et al., 2019; Rott et al., 2015). This method is useful, but there are several problems to be addressed due to the small differences in the Z/A ratios between the composition models of the core. First, the water content in the mantle should be confirmed because it also causes neutrino oscillations. Second, this method can assay each composition model, but it would be difficult to determine all light element content in the core. The composition model of the core needs to be well-established and proposed by experimental petrology. Despite these difficulties, neutrino oscillation will play a significant role in determining the core composition and can provide robust evidence that hydrogen is in the core.

Figures

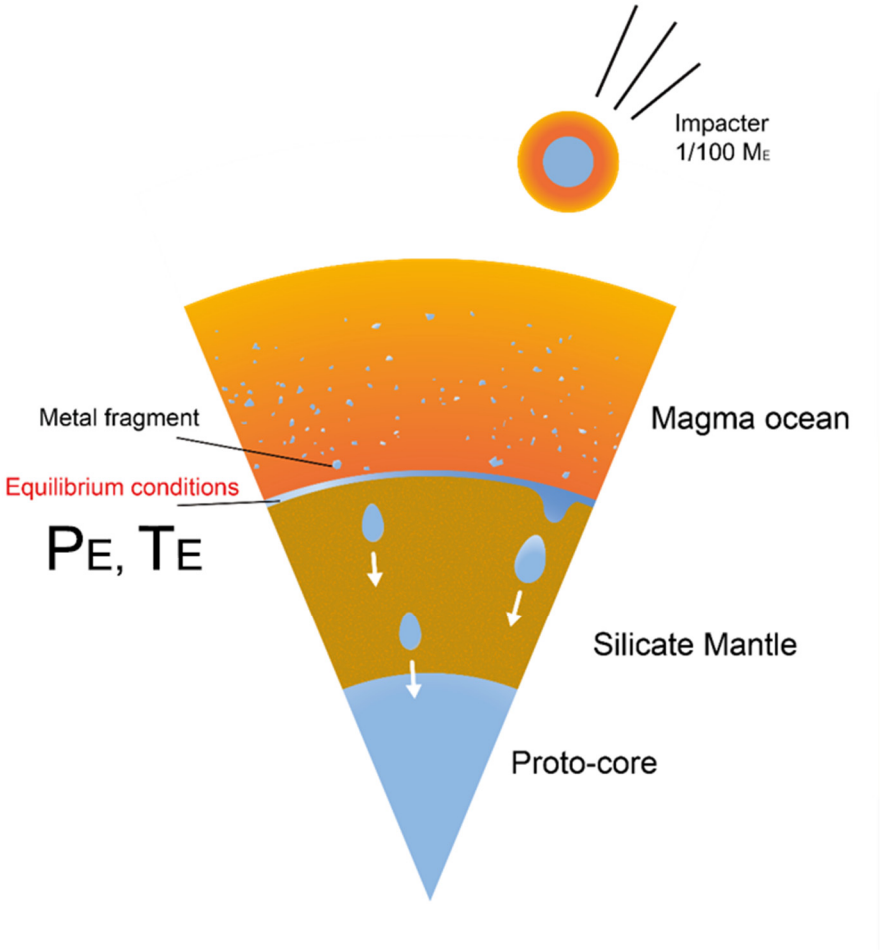

Figure 5.1 Schematic diagram of the continuous core formation scenario

The magma ocean and metal accreted as an impactor reach the equilibrium at the bottom of the magma ocean.

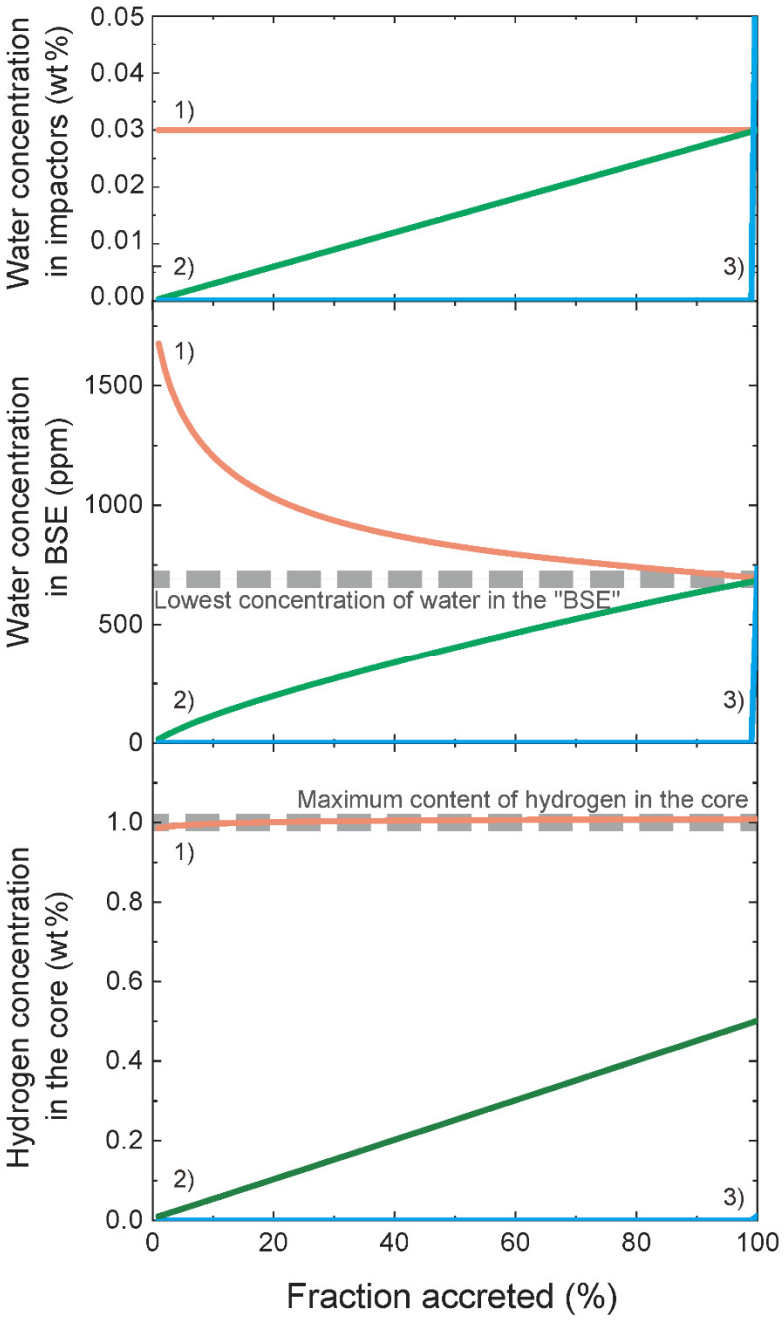

Figure 5.2 Evolution of hydrogen and water contents in the core and silicate mantle

I performed the core formation calculation along the P, T, and *f*O2 on path "6" in Badro et al. (2015). The remnant water content of the "BSE" at the end of core formation, was 687 ppm, as a constraint of the model. The upper panel consisted of the characteristic pass of water concentration in impactors, the middle panel involved the changing of water concentration of BSE, and the lower panel involved the changing of the hydrogen concentration in the core.

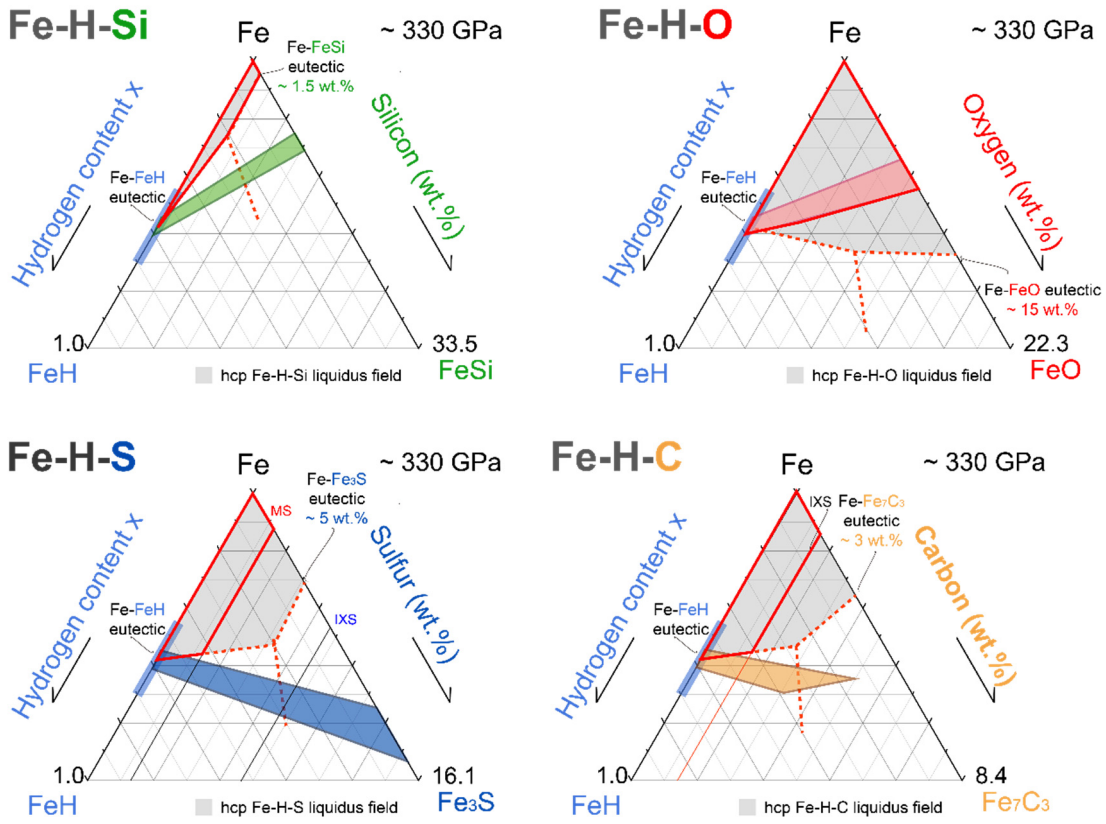

Figure 5.3 Possible outer core composition in Fe-H-X ternary systems

Gray hatched areas represent the field that *hcp* Fe-H-X is crystallized, which is constraint by Fe–H (this study), Fe–Si (Ozawa et al., 2016), Fe–S (Mori et al., 2017), Fe–O (Oka et al., 2019), and Fe–C (Mashino et al., 2019) binary systems. Colored regions show the range of the maximum composition of the outer core that explains its density based on studies on iron alloys (this study; Umemoto and Hirose, 2019). If the core is the ternary system as Fe-H-X, the core component should be in the area hatched by both colored and grey regions. I also indicated the maximum amount constraint by other criteria: metal silicate (MS) partitioning and inelastic X-ray-scattering (IXS) study for Fe-X liquid. The area surrounded by solid red lines indicates the possible component for four or more light elements systems in the core.

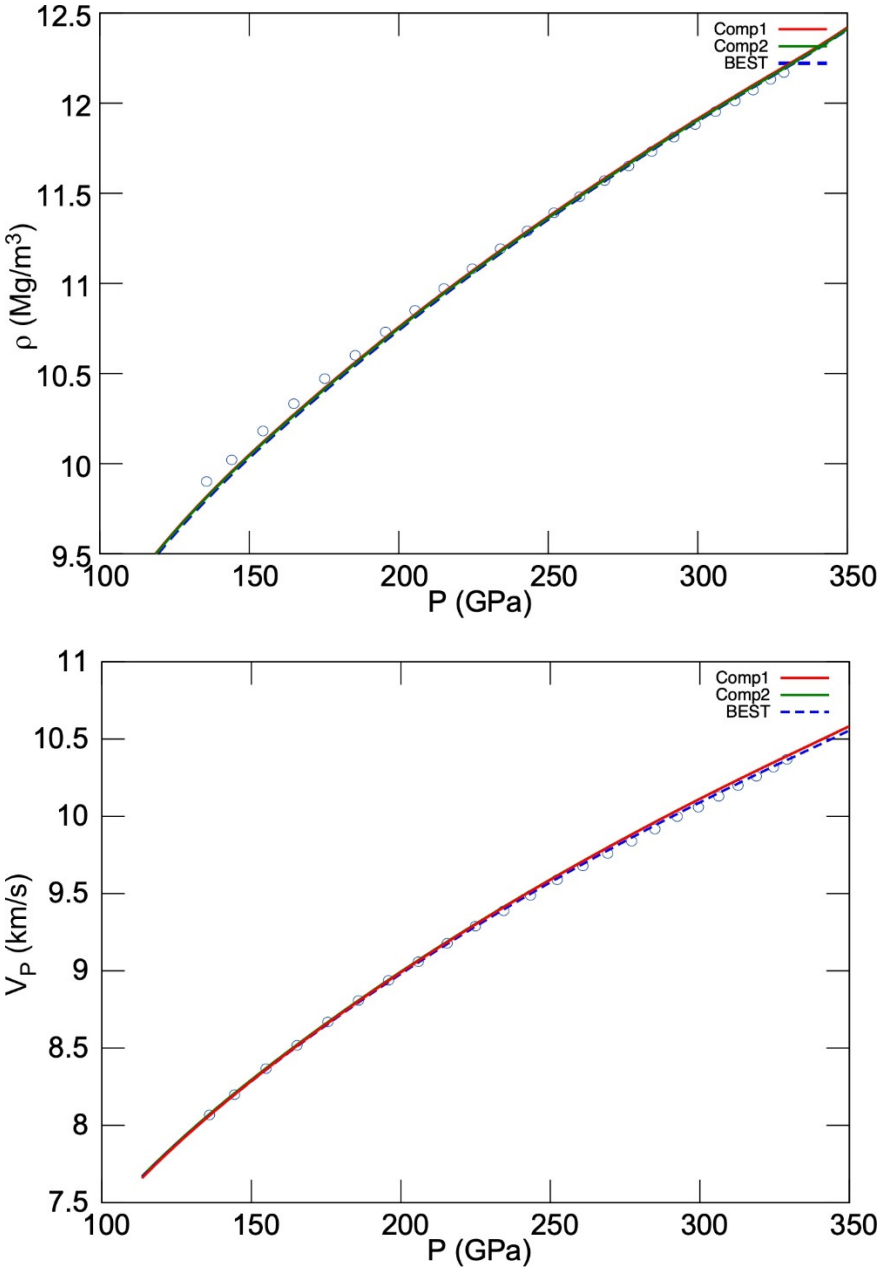

Figure 5.4 ρ and V_P of hydrogen bearing the Earth's core composition models

Comp 1 (red curve) and Comp 2 (green curve) show ρ and V_P of chemical composition of O-rich model (0.43 wt.% H, 1.3 wt.% Si, 2.3 wt.% O, 1.9 wt.% S, and no C), and Si-rich model (0.45 wt.% H, 2.2 wt.% Si, 1.5 wt.% O, 1.9 wt.% S, and no C), respectively. Blue circles indicate the ρ and V_P of PREM. ICB temperature is assumed as 5,400K. The value was provided by Dr. K. Umemoto and obtained in the same way in Umemoto and Hirose (2020). Note that the "Best" (blue curve) represents the composition that minimizes the deviation of ρ and V_P from the PREM in the study, which also contains 0.64 wt.% H.

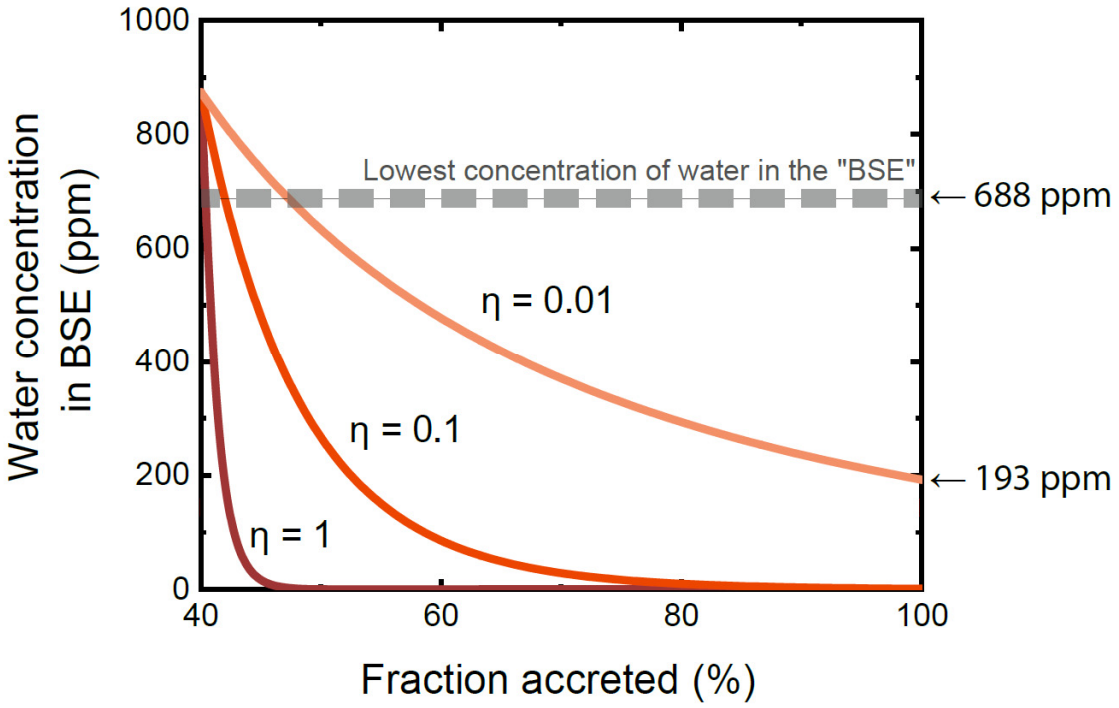

Figure 5. 5 Estimation of the contribution of hydrogen from nebula gasses

This figure shows the simulation result for the changing of water concentration in the BSE if hydrogen ingassing from nebula gas stops at 40% of the Earth's accretion. I assumed the water concentration at the timing is 880 ppm in the BSE (It is the same concentration as Figure 5.2 (A) at the timing). η is a parameter indicating the efficiency of equilibrium of core and mantle, which is defined as $\frac{M^{MO}_{\text{equilibrates with the metal}}}{M_{MO}}$ and it would be within the range of 1–0.005 (its average is typically larger than 0.01). Even if η is low, almost hydrogen originated from nebula gas partitioning into the core.

Concluding Remarks

The objective of the present thesis is to ascertain whether or not hydrogen is a major light element in the terrestrial core. In Chapter 2, I quantified the partitioning coefficient of hydrogen as a function of pressure, temperature, and fO_2. Then, in Chapter 3, I determined the phase diagram of the Fe-FeH binary system and found that the miscibility gap exists at $0.44 < x < 0.69$ up to core pressures. Features of the phase diagram of the Fe-FeH system do not rule out the hydrogen in the core up to ~1 wt.%. In Chapter 4, I carried out the compression experiments for the *hcp* Fe-Si-H alloy and found that this alloy explains the density profile of the PREM. It also constraint the maximum content of hydrogen in the core experimentally, which is 1.24 wt.% (x=0.70). Although future work should address V_S at high-temperature conditions, and the credibility of estimation of hydrogen contents, all features I found for the Fe-H system do not preclude hydrogen bearing the terrestrial core. According to studies on other light element systems and this work, the core is likely to contain around 0.4 wt.% H, which is comparable to 50 times the amount of seawater. Hydrogen and water amount of the Earth's interior is a key for grasping the Earth's building blocks. I hope this work will contribute to future studies to understand the origin of our planet. As a conclusion of the study, hydrogen is a feasible light element in the Earth's core.

References

Abe, Y., Ohtani, E., Okuchi, T., Righter, K, Drake, M., 2000. Water in the early earth, in: Canup, R.M., Righter, Kevin (Eds.), Origin of the Earth and Moon. University of Arizona Press, Tucson, pp. 413–433.

Akahama, Y., Kawamura, H., 2004. High-pressure Raman spectroscopy of diamond anvils to 250 GPa: Method for pressure determination in the multimegabar pressure range. J. Appl. Phys. 96, 3748–3751. https://doi.org/10.1063/1.1778482

Alexander, C.M.O., 2019. Quantitative models for the elemental and isotopic fractionations in chondrites: The carbonaceous chondrites. Geochim. Cosmochim. Acta 254, 277–309. https://doi.org/10.1016/j.gca.2019.02.008

Alexander, C.M.O., Bowden, R., Fogel, M.L., Howard, K.T., Herd, C.D.K., Nittler, L.R., 2012. The Provenances of Asteroids, and Their Contributions to the Volatile Inventories of the Terrestrial Planets. Science 337, 721–723. https://doi.org/10.1126/science.1223474

Alfé, D., Gillan, M.J., Price, G.D., 2002. Composition and temperature of the earth's core constrained by combining ab initio calculations and seismic data. Earth Planet. Sci. Lett. 195, 91–98. https://doi.org/10.1016/S0012-821X(01)00568-4

Allègre, C., Manhès, G., Lewin, É., 2001. Chemical composition of the Earth and the volatility control on planetary genetics. Earth Planet. Sci. Lett. 185, 49–69. https://doi.org/10.1016/S0012-821X(00)00359-9

Allègre, C.J., Poirier, J.-P., Humler, E., Hofmann, A.W., 1995. The chemical composition of the Earth. Earth Planet. Sci. Lett. 134, 515–526. https://doi.org/10.1016/0012-821X(95)00123-T

Anderson, O.L., Isaak, D.G., 2002. Another look at the core density deficit of Earth's outer core. Phys. Earth Planet. Inter. 131, 19–27. https://doi.org/10.1016/S0031-9201(02)00017-1

Andrault, D., Bolfan-Casanova, N., Nigro, G. Lo, Bouhifd, M.A., Garbarino, G., Mezouar, M., 2011. Solidus and liquidus profiles of chondritic mantle: Implication for melting of the Earth across its history. Earth Planet. Sci. Lett. 304, 251–259. https://doi.org/10.1016/j.epsl.2011.02.006

Antonangeli, D., Benedetti, L.R., Farber, D.L., Steinle-Neumann, G., Auzende, A.L., Badro, J., Hanfland, M., Krisch, M., 2008. Anomalous pressure evolution of the axial ratio ca in hcp cobalt: Interplay between structure, magnetism, and lattice dynamics. Appl. Phys. Lett. 92. https://doi.org/10.1063/1.2897038

Antonov, V.E., Cornell, K., Fedotov, V.K., Kolesnikov, A.I., Ponyatovsky, E.G., Shiryaev, V.I., Wipf, H., 1998. Neutron diffraction investigation of the dhcp and hcp iron hydrides and deuterides. J. Alloys Compd. 264, 214–222. https://doi.org/10.1016/S0925-8388(97)00298-3

Anzellini, S., Dewaele, A., Mezouar, M., Loubeyre, P., Morard, G., 2013. Melting of Iron at Earth's Inner Core Boundary Based on Fast X-ray Diffraction. Science 340, 464–466. https://doi.org/10.1126/science.1233514

Badding, J. V., Hemley, R.J., Mao, H.K., 1991. High-Pressure Chemistry of Hydrogen in Metals: In Situ Study of Iron Hydride. Science 253, 421–424. https://doi.org/10.1126/science.253.5018.421

Badro, J., Brodholt, J.P., Piet, H., Siebert, J., Ryerson, F.J., 2015. Core formation and core composition from coupled geochemical and geophysical constraints. Proc. Natl. Acad. Sci. U. S. A. 112, 12310–12314. https://doi.org/10.1073/pnas.1505672112

Badro, J., Cote, A.S., Brodholt, J.P., 2014. A seismologically consistent compositional model of Earth's core. Proc. Natl. Acad. Sci. 111, 7542–7545. https://doi.org/10.1073/pnas.1316708111

Bass, J.D., Zhang, J.S., 2015. Theory and Practice: Techniques for Measuring High-P–T Elasticity, in: Treatise on Geophysics. Elsevier, pp. 293–312. https://doi.org/10.1016/B978-0-444-53802-4.00037-3

Birch, F., 1952. Elasticity and constitution of the Earth's interior. J. Geophys. Res. 57, 227–286. https://doi.org/10.1029/JZ057i002p00227

Blanchard, I., Jennings, E.S., Franchi, I.A., Zhao, X., Petitgirard, S., Miyajima, N., 2018. The Fate of Carbon during Earth's Core – Mantle Differentiation, in: AGU Fall Meeting 2018 Abstract. https://doi.org/10.31223/osf.io/9t7ps

Boehler, R., Guthrie, M., Molaison, J.J., dos Santos, A.M., Sinogeikin, S., Machida, S., Pradhan, N., Tulk, C.A., 2013. Large-volume diamond cells for neutron diffraction above 90 GPa. High Press. Res. 33, 546–554. https://doi.org/10.1080/08957959.2013.823197

Bourret, S., Coelho, J.A.B., Kaminski, E., 2019. Probing the Earth Core Composition with Neutrino Oscillation Tomography, in: 36th International Cosmic Ray Conference - ICRC2019-. pp. 0–7.

Brasser, R., Dauphas, N., Mojzsis, S.J., 2018. Jupiter's Influence on the Building Blocks of Mars and Earth. Geophys. Res. Lett. https://doi.org/10.1029/2018GL078011

Braukmüller, N., Wombacher, F., Funk, C., Münker, C., 2019. Earth's volatile element depletion pattern inherited from a carbonaceous chondrite-like source. Nat. Geosci. 12, 564–568. https://doi.org/10.1038/s41561-019-0375-x

Brown, J.M., McQueen, R.G., 1986. Phase transitions, Grüneisen parameter, and elasticity for shocked iron between 77 GPa and 400 GPa. J. Geophys. Res. Solid Earth 91, 7485–7494. https://doi.org/10.1029/JB091iB07p07485

Caracas, R., 2015. The influence of hydrogen on the seismic properties of solid iron. Geophys. Res. Lett. 42, 3780–3785. https://doi.org/10.1002/2015GL063478

Caracas, R., Cohen, R.E., 2005. Effect of chemistry on the stability and elasticity of the perovskite and post-perovskite phases in the $MgSiO_3$-$FeSiO_3$- Al_2O_3 system and implications for the lowermost mantle. Geophys. Res. Lett. 32, 1–4. https://doi.org/10.1029/2005GL023164

Chabot, N.L., Wollack, E.A., Klima, R.L., Minitti, M.E., 2014. Experimental constraints on Mercury's core composition. Earth Planet. Sci. Lett. 390, 199–208. https://doi.org/10.1016/j.epsl.2014.01.004

Chakravarty, S., Rose, J.H., Wood, D., Ashcroft, N.W., 1981. Theory of dense hydrogen. Phys. Rev. B 24, 1624–1635. https://doi.org/10.1103/PhysRevB.24.1624

Chen, B., Gao, L., Funakoshi, K., Li, J., 2007. Thermal expansion of iron-rich alloys and implications for the Earth's core. Proc. Natl. Acad. Sci. U. S. A. 104, 9162–9167. https://doi.org/10.1073/pnas.0610474104

Chen, B., Li, Z., Zhang, D., Liu, J., Hu, M.Y., Zhao, J., Bi, W., Alp, E.E., Xiao, Y., Chow, P., Li, J., 2014. Hidden carbon in Earth's inner core revealed by shear softening in dense Fe_7C_3. Proc. Natl. Acad. Sci. 111, 17755–17758. https://doi.org/10.1073/pnas.1411154111

Chi, Z., Nguyen, H., Matsuoka, T., Kagayama, T., Hirao, N., Ohishi, Y., Shimizu, K., 2011. Cryogenic implementation of charging diamond anvil cells with H_2 and D_2. Rev. Sci. Instrum. 82, 105109. https://doi.org/10.1063/1.3652981

Clesi, V., Bouhifd, M.A., Bolfan-Casanova, N., Manthilake, G., Schiavi, F., Raepsaet, C., Bureau, H., Khodja, H., Andrault, D., 2018. Low hydrogen contents in the cores of terrestrial planets. Sci. Adv. 4, e1701876. https://doi.org/10.1126/sciadv.1701876

Dasgupta, R., Chi, H., Shimizu, N., Buono, A.S., Walker, D., 2013. Carbon solution and partitioning between metallic and silicate melts in a shallow magma ocean: Implications for the origin and distribution of terrestrial carbon. Geochim. Cosmochim. Acta. https://doi.org/10.1016/j.gca.2012.10.011

Dauphas, N., 2017. The isotopic nature of the Earth's accreting material through time. Nature 541, 521–524. https://doi.org/10.1038/nature20830

de Koker, N.P., Stixrude, L., Karki, B.B., 2008. Thermodynamics, structure, dynamics, and freezing of Mg_2SiO_4 liquid at high pressure. Geochim. Cosmochim. Acta 72, 1427–1441. https://doi.org/10.1016/j.gca.2007.12.019

Dewaele, A., Loubeyre, P., Occelli, F., Mezouar, M., Dorogokupets, P.I., Torrent, M., 2006. Quasihydrostatic Equation of State of Iron above 2 Mbar. Phys. Rev. Lett. 97, 215504. https://doi.org/10.1103/PhysRevLett.97.215504

Dewaele, A., Torrent, M., 2013. Equation of state of α-Al_2O_3. Phys. Rev. B - Condens. Matter Mater. Phys. 88, 1–5. https://doi.org/10.1103/PhysRevB.88.064107

Dixon, J.E., Leist, L., Langmuir, C., Schilling, J.-G., 2002. Recycled dehydrated lithosphere observed in plume-influenced mid-ocean-ridge basalt. Nature 420, 385–389. https://doi.org/10.1038/nature01215

Dorogokupets, P.I., Dewaele, A., 2007. Equations of state of MgO, Au, Pt, NaCl-B1, and NaCl-B2: Internally consistent high-temperature pressure scales. High Press. Res. 27, 431–446. https://doi.org/10.1080/08957950701659700

Dorogokupets, P.I., Dymshits, A.M., Litasov, K.D., Sokolova, T.S., Ahrens, T.J., 2017. Thermodynamics and Equations of State of Iron to 350 GPa and 6000 K. Sci. Rep. 7, 41863. https://doi.org/10.1038/srep41863

Dorogokupets, P.I., Oganov, A.R., 2007. Ruby, metals, and MgO as alternative pressure scales: A semiempirical description of shock-wave, ultrasonic, x-ray, and thermochemical data at high temperatures and pressures. Phys. Rev. B - Condens. Matter Mater. Phys. 75, 1–16. https://doi.org/10.1103/PhysRevB.75.024115

Doyle, A.E., Young, E.D., Klein, B., Zuckerman, B., Schlichting, H.E., 2019. Oxygen fugacities of extrasolar rocks: Evidence for an Earth-like geochemistry of exoplanets. Science 366, 356–359. https://doi.org/10.1126/science.aax3901

Dziewonski, A.M., Anderson, D.L., 1981. Preliminary reference Earth model. Phys. Earth Planet. Inter. 25, 297–356. https://doi.org/10.1016/0031-9201(81)90046-7

Elsässer, C., Zhu, J., Louie, S.G., Meyer, B., Fähnle, M., Chan, C.T., 1998. Ab initio study of iron and iron hydride : II . Structural and magnetic properties of close-packed Fe and FeH. J. Phys. Condens. Matter 10, 5113–5129. https://doi.org/10.1088/0953-8984/10/23/013

Fiquet, G., Auzende, A.L., Siebert, J., Corgne, A., Bureau, H., Ozawa, H., Garbarino, G., 2010. Melting of Peridotite to 140 Gigapascals. Science 329, 1516–1518. https://doi.org/10.1126/science.1192448

Fischer-Gödde, M., Kleine, T., 2017. Ruthenium isotopic evidence for an inner Solar System origin of the late veneer. Nature 541, 525–527. https://doi.org/10.1038/nature21045

Fischer, R.A., Campbell, A.J., Caracas, R., Reaman, D.M., Heinz, D.L., Dera, P., Prakapenka, V.B., 2014. Equations of state in the Fe-FeSi system at high pressures and temperatures. J. Geophys. Res. Solid Earth 119, 2810–2827. https://doi.org/10.1002/2013JB010898

Fischer, R.A., Campbell, A.J., Shofner, G.A., Lord, O.T., Dera, P., Prakapenka, V.B., 2011. Equation of state and phase diagram of FeO. Earth Planet. Sci. Lett. 304, 496–502. https://doi.org/10.1016/j.epsl.2011.02.025

Fischer, R.A., Cottrell, E., Hauri, E., Lee, K.K.M., Le Voyer, M., 2019. The carbon content of Earth's core from metal – silicate partitioning experiments, in: Goldschmidt 2019 Abstract. Barcelona.

Fischer, R.A., Nakajima, Y., Campbell, A.J., Frost, D.J., Harries, D., Langenhorst, F., Miyajima, N., Pollok, K., Rubie, D.C., 2015. High pressure metal–silicate partitioning of Ni, Co, V, Cr, Si, and O. Geochim. Cosmochim. Acta 167, 177–194. https://doi.org/10.1016/j.gca.2015.06.026

Fukai, Y., 1992. Some Properties of the Fe-H System at High Pressures and Temperatures, and their Implications for the Earth's Core, in: Syono, Y., Manghnani, M.H. (Eds.), High-Pressure Research: Applications to Earth and Planetary Sciences. pp. 373–385. https://doi.org/10.1029/GM067p0373

Fukai, Y., Sugimoto, H., 1985. Diffusion of hydrogen in metals. Adv. Phys. 34, 263–326. https://doi.org/10.1080/00018738500101751

Fukai, Y., Suzuki, T., 1986. Iron-water reaction under high pressure and its implication in the evolution of the Earth. J. Geophys. Res. 91, 9222. https://doi.org/10.1029/JB091iB09p09222

Genda, H., Ikoma, M., 2008. Origin of the ocean on the Earth: Early evolution of water D/H in a hydrogen-rich atmosphere. Icarus 194, 42–52. https://doi.org/10.1016/j.icarus.2007.09.007

Georg, R.B., Halliday, A.N., Schauble, E.A., Reynolds, B.C., 2007. Silicon in the Earth's core. Nature 447, 1102–1106. https://doi.org/10.1038/nature05927

Glazyrin, K., Pourovskii, L. V., Dubrovinsky, L., Narygina, O., McCammon, C., Hewener, B., Schünemann, V., Wolny, J., Muffler, K., Chumakov, A.I., Crichton, W., Hanfland, M., Prakapenka, V.B., Tasnádi, F., Ekholm, M., Aichhorn, M., Vildosola, V., Ruban, A. V., Katsnelson, M.I., Abrikosov, I.A., 2013. Importance of Correlation Effects in *hcp* Iron Revealed by a Pressure-Induced Electronic Topological Transition. Phys. Rev. Lett. 110, 117206. https://doi.org/10.1103/PhysRevLett.110.117206

Gomes, R., Levison, H.F., Tsiganis, K., Morbidelli, A., 2005. Origin of the cataclysmic Late Heavy Bombardment period of the terrestrial planets. Nature 435, 466–469. https://doi.org/10.1038/nature03676

Gomi, H., Fei, Y., Yoshino, T., 2018. The effects of ferromagnetism and interstitial hydrogen on the equation of states of hcp and dhcp FeHx: Implications for the Earth's inner core age. Am. Mineral. 103, 1271–1281. https://doi.org/10.2138/am-2018-6295

Greenwood, J.P., Itoh, S., Sakamoto, N., Warren, P., Taylor, L., Yurimoto, H., 2011. Hydrogen isotope ratios in lunar rocks indicate delivery of cometary water to the Moon. Nat. Geosci. 4, 79–82. https://doi.org/10.1038/ngeo1050

Grewal, D.S., Dasgupta, R., Sun, C., Tsuno, K., Costin, G., 2019. Delivery of carbon, nitrogen, and sulfur to the silicate Earth by a giant impact. Sci. Adv. 5, eaau3669. https://doi.org/10.1126/sciadv.aau3669

Hallis, L.J., Huss, G.R., Nagashima, K., Taylor, G.J., Halldórsson, S.A., Hilton, D.R., Mottl, M.J., Meech, K.J., 2015. Evidence for primordial water in Earth's deep mantle. Science 350, 336–339. https://doi.org/10.1126/science.aac4834

Helffrich, G., 2014. Outer core compositional layering and constraints on core liquid transport properties. Earth Planet. Sci. Lett. 391, 256–262. https://doi.org/10.1016/j.epsl.2014.01.039

Hirao, N., Kondo, T., Ohtani, E., Takemura, K., Kikegawa, T., 2004. Compression of iron hydride to 80 GPa and hydrogen in the Earth's inner core. Geophys. Res. Lett. 31, L06616 1-4. https://doi.org/10.1029/2003GL019380

Hirose, K., Fei, Y., Ma, Y., Mao, H.-K., 1999. The fate of subducted basaltic crust in the Earth's lower mantle. Nature 397, 53–56. https://doi.org/10.1038/16225

Hirose, K., Labrosse, S., Hernlund, J., 2013. Composition and State of the Core. Annu. Rev. Earth Planet. Sci. 41, 657–691. https://doi.org/10.1146/annurev-earth-050212-124007

Hirose, K., Morard, G., Sinmyo, R., Umemoto, K., Hernlund, J., Helffrich, G., Labrosse, S., 2017. Crystallization of silicon dioxide and compositional evolution of the Earth's core. Nature 543, 99–102. https://doi.org/10.1038/nature21367

Hirose, K., Tagawa, S., Kuwayama, Y., Sinmyo, R., Morard, G., Ohishi, Y., Genda, H., 2019. Hydrogen Limits Carbon in Liquid Iron. Geophys. Res. Lett. 2019GL082591. https://doi.org/10.1029/2019GL082591

Hirschmann, M.M., 2016. Constraints on the early delivery and fractionation of Earth's major volatiles from C/H, C/N, and C/S ratios. Am. Mineral. 101, 540–553. https://doi.org/10.2138/am-2016-5452

Ichikawa, H., Tsuchiya, T., Tange, Y., 2014. The P-V-T equation of state and thermodynamic properties of liquid iron. J. Geophys. Res. Solid Earth 119, 240–252. https://doi.org/10.1002/2013JB010732

Iizuka-Oku, R., Yagi, T., Gotou, H., Okuchi, T., Hattori, T., Sano-Furukawa, A., 2017. Hydrogenation of iron in the early stage of Earth's evolution. Nat. Commun. 8, 14096. https://doi.org/10.1038/ncomms14096

Ikoma, M., Genda, H., 2006. Constraints on the Mass of a Habitable Planet with Water of Nebular Origin. Astrophys. J. 648, 696–706. https://doi.org/10.1086/505780

Ikuta, D., Ohtani, E., Sano-Furukawa, A., Shibazaki, Y., Terasaki, H., Yuan, L., Hattori, T., 2019. Interstitial hydrogen atoms in face-centered cubic iron in the Earth's core. Sci. Rep. 9, 7108. https://doi.org/10.1038/s41598-019-43601-z

Irving, J.C.E., Cottaar, S., Lekic, V., 2018. Seismically determined elastic parameters for Earth's outer core. Sci. Adv. 4, eaar2538. https://doi.org/10.1126/sciadv.aar2538

Isaev, E.I., Skorodumova, N. V, Ahuja, R., Vekilov, Y.K., Johansson, B., 2007. Dynamical stability of Fe-H in the Earth's mantle and core regions. Proc. Natl. Acad. Sci. 104, 9168–9171. https://doi.org/10.1073/pnas.0609701104

Iwamori, H., 1998. Transportation of H_2O and melting in subduction zones. Earth Planet. Sci. Lett. 160, 65–80. https://doi.org/10.1016/S0012-821X(98)00080-6

Jacobson, S.A., Walsh, K.J., 2015. Earth and Terrestrial Planet Formation, in: The Early Earth: Accretion and Differentiation. pp. 49–70. https://doi.org/10.1002/9781118860359.ch3

Kato, C., Umemoto, K., Ohta, K., Tagawa, S., Hirose, K., Ohishi, Y., 2020. Stability of fcc phase FeH to 137 GPa. Am. Mineral. 105. https://doi.org/10.2138/am-2020-7153

Kawaguchi, S.I., Nakajima, Y., Hirose, K., Komabayashi, T., Ozawa, H., Tateno, S., Kuwayama, Y., Tsutsui, S., Baron, A.Q.R., 2017. Sound velocity of liquid Fe-Ni-S at high pressure. J. Geophys. Res. Solid Earth 122, 3624–3634. https://doi.org/10.1002/2016JB013609

Kennett, B.L.N., Engdahl, E.R., Buland, R., 1995. Constraints on seismic velocities in the Earth from traveltimes. Geophys. J. Int. 122, 108–124. https://doi.org/10.1111/j.1365-246X.1995.tb03540.x

Kusakabe, M., Hirose, K., Sinmyo, R., Kuwayama, Y., Ohishi, Y., Helffrich, G., 2019. Melting Curve and Equation of State of β-Fe_7N_3 : Nitrogen in the Core? J. Geophys. Res. Solid Earth 124, 3448–3457. https://doi.org/10.1029/2018JB015823

Lécuyer, C., Gillet, P., Robert, F., 1998. The hydrogen isotope composition of seawater and the global water cycle. Chem. Geol. 145, 249–261. https://doi.org/10.1016/S0009-2541(97)00146-0

Li, J., Fei, Y., 2014. Experimental Constraints on Core Composition, in: Treatise on Geochemistry. Elsevier, pp. 527–557. https://doi.org/10.1016/B978-0-08-095975-7.00214-X

Li, Y., Vočadlo, L., Alfè, D., Brodholt, J., 2018. Mg partitioning between solid and liquid iron under the Earth's core conditions. Phys. Earth Planet. Inter. 274, 218–221. https://doi.org/10.1016/j.pepi.2017.12.003

Machida, A., Saitoh, H., Hattori, T., Sano-Furukawa, A., Funakoshi, K., Sato, T., Orimo, S., Aoki, K., 2019. Hexagonal Close-packed Iron Hydride behind the Conventional Phase Diagram. Sci. Rep. 9, 12290. https://doi.org/10.1038/s41598-019-48817-7

Machida, A., Saitoh, H., Sugimoto, H., Hattori, T., Sano-Furukawa, A., Endo, N., Katayama, Y., Iizuka, R., Sato, T., Matsuo, M., Orimo, S.-I., Aoki, K., 2014. Site occupancy of interstitial deuterium atoms in face-centred cubic iron. Nat. Commun. 5, 5063. https://doi.org/10.1038/ncomms6063

Malavergne, V., Bureau, H., Raepsaet, C., Gaillard, F., Poncet, M., Surblé, S., Sifré, D., Shcheka, S., Fourdrin, C., Deldicque, D., Khodja, H., 2019. Experimental constraints on the fate of H and C during planetary core-mantle differentiation. Implications for the Earth. Icarus 321, 473–485. https://doi.org/10.1016/j.icarus.2018.11.027

Mao, W.L., Sturhahn, W., Heinz, D.L., Mao, H.-K., Shu, J., Hemley, R.J., 2004. Nuclear resonant x-ray scattering of iron hydride at high pressure. Geophys. Res. Lett. 31, L15618. https://doi.org/10.1029/2004GL020541

Marrocchi, Y., Bekaert, D. V., Piani, L., 2018. Origin and abundance of water in carbonaceous asteroids. Earth Planet. Sci. Lett. 482, 23–32. https://doi.org/10.1016/j.epsl.2017.10.060

Martorell, B., Vocadlo, L., Brodholt, J., Wood, I.G., 2013. Strong premelting effect in the elastic properties of *hcp*-Fe under inner-core conditions. Science 342, 466–468. https://doi.org/10.1126/science.1243651

Marty, B., 2012. The origins and concentrations of water, carbon, nitrogen and noble gases on Earth. Earth Planet. Sci. Lett. 313–314, 56–66. https://doi.org/10.1016/j.epsl.2011.10.040

Mashino, I., Miozzi, F., Hirose, K., Morard, G., Sinmyo, R., 2019. Melting experiments on the Fe–C binary system up to 255 GPa: Constraints on the carbon content in the Earth's core. Earth Planet. Sci. Lett. 515, 135–144. https://doi.org/10.1016/j.epsl.2019.03.020

Masters, G., Gubbins, D., 2003. On the resolution of density within the Earth. Phys. Earth Planet. Inter. 140, 159–167. https://doi.org/10.1016/j.pepi.2003.07.008

McDonough, W.F., 2014. Compositional Model for the Earth's Core, in: Carlson, R.W., Holland, H.D., Turekian, K.K. (Eds.), Treatise on Geochemistry. Elsevier, pp. 559–577. https://doi.org/10.1016/B978-0-08-095975-7.00215-1

Meier, T., Trybel, F., Khandarkhaeva, S., Steinle-Neumann, G., Chariton, S., Fedotenko, T., Petitgirard, S., Hanfland, M., Glazyrin, K., Dubrovinskaia, N., Dubrovinsky, L., 2019. Pressure-Induced Hydrogen-Hydrogen Interaction in Metallic FeH Revealed by NMR. Phys. Rev. X 9, 31008. https://doi.org/10.1103/physrevx.9.031008

Mitsui, T., Hirao, N., 2010. Ultrahigh-pressure study on the magnetic state of iron hydride using an energy domain synchrotron radiation 57 Fe Mössbauer spectrometer. MRS Proc. 1262, 1262-W06-09. https://doi.org/10.1557/PROC-1262-W06-09

Momma, K., Izumi, F., 2011. VESTA 3 for three-dimensional visualization of crystal, volumetric and morphology data. J. Appl. Crystallogr. 44, 1272–1276. https://doi.org/10.1107/S0021889811038970

Mori, Y., Ozawa, H., Hirose, K., Sinmyo, R., Tateno, S., Morard, G., Ohishi, Y., 2017. Melting experiments on Fe–Fe_3S system to 254 GPa. Earth Planet. Sci. Lett. 464, 135–141. https://doi.org/10.1016/j.epsl.2017.02.021

Muralidharan, K., Deymier, P., Stimpfl, M., de Leeuw, N.H., Drake, M.J., 2008. Origin of water in the inner Solar System: A kinetic Monte Carlo study of water adsorption on forsterite. Icarus 198, 400–407. https://doi.org/10.1016/j.icarus.2008.07.017

Nakajima, Y., Imada, S., Hirose, K., Komabayashi, T., Ozawa, H., Tateno, S., Tsutsui, S., Kuwayama, Y., Baron, A.Q.R., 2015. Carbon-depleted outer core revealed by sound velocity measurements of liquid iron–carbon alloy. Nat. Commun. 6, 8942. https://doi.org/10.1038/ncomms9942

Nakajima, Y., Takahashi, E., Sata, N., Nishihara, Y., Hirose, K., Funakoshi, K.I., Ohishi, Y., 2011. Thermoelastic property and high-pressure stability of Fe_7C_3: Implication for iron-carbide in the Earth's core. Am. Mineral. 96, 1158–1165. https://doi.org/10.2138/am.2011.3703

Narygina, O., Dubrovinsky, L.S., McCammon, C.A., Kurnosov, A., Kantor, I.Y., Prakapenka, V.B., Dubrovinskaia, N.A., 2011. X-ray diffraction and Mössbauer spectroscopy study of fcc iron hydride FeH at high pressures and implications for the composition of the Earth's core. Earth Planet. Sci. Lett. 307, 409–414. https://doi.org/10.1016/j.epsl.2011.05.015

Nomura, R., Hirose, K., Uesugi, K., Ohishi, Y., Tsuchiyama, A., Miyake, A., Ueno, Y., 2014. Low Core-Mantle Boundary Temperature Inferred from the Solidus of Pyrolite. Science 343, 522–525. https://doi.org/10.1126/science.1248186

O'Brien, D.P., Walsh, K.J., Morbidelli, A., Raymond, S.N., Mandell, A.M., 2014. Water delivery and giant impacts in the "Grand Tack" scenario. Icarus 239, 74–84. https://doi.org/10.1016/j.icarus.2014.05.009

Ohishi, Y., Hirao, N., Sata, N., Hirose, K., Takata, M., 2008. Highly intense monochromatic X-ray diffraction facility for high-pressure research at SPring-8. High Press. Res. 28, 163–173. https://doi.org/10.1080/08957950802208910

Ohta, K., Ichimaru, K., Einaga, M., Kawaguchi, S., Shimizu, K., Matsuoka, T., Hirao, N., Ohishi, Y., 2015. Phase boundary of hot dense fluid hydrogen. Sci. Rep. 5, 16560. https://doi.org/10.1038/srep16560

Ohta, K., Suehiro, S., Hirose, K., Ohishi, Y., 2018. Electrical resistivity of *fcc* phase iron hydrides at high pressures and temperatures. Comptes Rendus - Geosci. https://doi.org/10.1016/j.crte.2018.05.004

Oka, A., Nakamoto, T., Ida, S., 2011. Evolution of snow line in optically thick protoplanetary disks: effects of water ice opacity and dust grain size. Astrophys. J. 738, 141. https://doi.org/10.1088/0004-637X/738/2/141

Oka, K., Hirose, K., Tagawa, S., Kidokoro, Y., Nakajima, Y., Kuwayama, Y., Morard, G., Coudurier, N., Fiquet, G., 2019. Melting in the Fe-FeO system to 204 GPa: Implications for oxygen in Earth's core. Am. Mineral. 104, 1603–1607. https://doi.org/10.2138/am-2019-7081

Okamoto, H., 2004. Fe-H (Iron-Hydrogen). J. Phase Equilibria Diffus. 25, 101–102. https://doi.org/10.1361/10549710417867

Okuchi, T., 1997. Hydrogen partitioning into molten iron at high pressure: implications for Earth's core. Science 278, 1781–1784. https://doi.org/10.1126/science.278.5344.1781

Okuchi, T., Takahashi, E., 1997. Hydrogen in molten iron at high pressure: The first measurement. Geophys. Monogr. Ser. 101, 249–260. https://doi.org/10.1029/GM101p0249

Olson, P.L., Sharp, Z.D., 2019. Nebular atmosphere to magma ocean: A model for volatile capture during Earth accretion. Phys. Earth Planet. Inter. 294, 106294. https://doi.org/10.1016/j.pepi.2019.106294

Ozawa, H., Hirose, K., Tateno, S., Sata, N., Ohishi, Y., 2010. Phase transition boundary between B1 and B8 structures of FeO up to 210 GPa. Phys. Earth Planet. Inter. 179, 157–163. https://doi.org/10.1016/j.pepi.2009.11.005

Ozawa, H., Hirose, K., Yonemitsu, K., Ohishi, Y., 2016. High-pressure melting experiments on Fe-Si alloys and implications for silicon as a light element in the core. Earth Planet. Sci. Lett. 456, 47–54. https://doi.org/10.1016/j.epsl.2016.08.042

Palme, H., O'Neill, H.S.C., 2014. Cosmochemical Estimates of Mantle Composition, in: Treatise on Geochemistry. Elsevier, pp. 1–39. https://doi.org/10.1016/B978-0-08-095975-7.00201-1

Pépin, C.M., Dewaele, A., Geneste, G., Loubeyre, P., Mezouar, M., 2014. New Iron Hydrides under High Pressure. Phys. Rev. Lett. 113, 265504. https://doi.org/10.1103/PhysRevLett.113.265504

Peslier, A.H., Schönbächler, M., Busemann, H., Karato, S.I., 2017. Water in the Earth's Interior: Distribution and Origin. Space Sci. Rev. 212, 1–68. https://doi.org/10.1007/s11214-017-0387-z

Phaneuf, M.., 1999. Applications of focused ion beam microscopy to materials science specimens. Micron 30, 277–288. https://doi.org/10.1016/S0968-4328(99)00012-8

Poirier, J.P., 1994. Light elements in the Earth's outer core: A critical review. Phys. Earth Planet. Inter. 85, 319–337. https://doi.org/10.1016/0031-9201(94)90120-1

Rama Murthy, V., Hall, H.T., 1970. The chemical composition of the Earth's core: Possibility of sulphur in the core. Phys. Earth Planet. Inter. 2, 276–282. https://doi.org/10.1016/0031-9201(70)90014-2

Raymond, S.N., O'Brien, D.P., Morbidelli, A., Kaib, N.A., 2009. Building the terrestrial planets: Constrained accretion in the inner Solar System. Icarus 203, 644–662. https://doi.org/10.1016/j.icarus.2009.05.016

Raymond, S.N., Quinn, T., Lunine, J.I., 2007. High-resolution simulations of the final assembly of Earth-like planets. 2. Water delivery and planetary habitability. Astrobiology 7, 66–84. https://doi.org/10.1089/ast.2006.06-0126

Righter, K., Danielson, L., Drake, M.J., Domanik, K., 2014. Partition Coefficients at High Pressure and Temperature, in: Treatise on Geochemistry. Elsevier, pp. 449–477. https://doi.org/10.1016/B978-0-08-095975-7.00210-2

Righter, K., Drake, M.J., 1999. Effect of water on metal-silicate partitioning of siderophile elements: a high pressure and temperature terrestrial magma ocean and core formation. Earth Planet. Sci. Lett. 171, 383–399. https://doi.org/10.1016/S0012-821X(99)00156-9

Rott, C., Taketa, A., Bose, D., 2015. Spectrometry of the Earth using Neutrino Oscillations. Sci. Rep. 5, 15225. https://doi.org/10.1038/srep15225

Rubie, D.C., Jacobson, S.A., Morbidelli, A., O'Brien, D.P., Young, E.D., de Vries, J., Nimmo, F., Palme, H., Frost, D.J., 2015. Accretion and differentiation of the terrestrial planets with implications for the compositions of early-formed Solar System bodies and accretion of water. Icarus 248, 89–108. https://doi.org/10.1016/j.icarus.2014.10.015

Saitoh, H., Machida, A., Sugimoto, H., Yagi, T., Aoki, K., 2017. P–V–T relation of the Fe–H system under hydrogen pressure of several gigapascals. J. Alloys Compd. 706, 520–525. https://doi.org/10.1016/j.jallcom.2017.02.209

Sakamaki, K., Takahashi, E., Nakajima, Y., Nishihara, Y., Funakoshi, K., Suzuki, T., Fukai, Y., 2009. Melting phase relation of FeH*x* up to 20 GPa: Implication for the temperature of the Earth's core. Phys. Earth Planet. Inter. 174, 192–201. https://doi.org/10.1016/j.pepi.2008.05.017

Sakamoto, N., Seto, Y., Itoh, S., Kuramoto, K., Fujino, K., Nagashima, K., Krot, A.N., Yurimoto, H., 2007. Remnants of the Early Solar System Water Enriched in Heavy Oxygen Isotopes. Science 317, 231–233. https://doi.org/10.1126/science.1142021

Sata, N., Hirose, K., Shen, G., Nakajima, Y., Ohishi, Y., Hirao, N., 2010. Compression of FeSi, Fe_3C, $Fe_{0.95}O$, and FeS under the core pressures and implication for light element in the Earth's core. J. Geophys. Res. Solid Earth 115, 1–13. https://doi.org/10.1029/2009JB006975

Sato, T., Okuzumi, S., Ida, S., 2016. On the water delivery to terrestrial embryos by ice pebble accretion. Astron. Astrophys. 589, A15. https://doi.org/10.1051/0004-6361/201527069

Scheler, T., Degtyareva, O., Gregoryanz, E., 2011. On the effects of high temperature and high pressure on the hydrogen solubility in rhenium. J. Chem. Phys. 135. https://doi.org/10.1063/1.3652863

Schiller, M., Bizzarro, M., Fernandes, V.A., 2018. Isotopic evolution of the protoplanetary disk and the building blocks of Earth and the Moon. Nature 555, 507–510. https://doi.org/10.1038/nature25990

Seagle, C.T., Campbell, A.J., Heinz, D.L., Shen, G., Prakapenka, V.B., 2006. Thermal equation of State of Fe_3S and implications for sulfur in Earth's core. J. Geophys. Res. Solid Earth 111, 1–7. https://doi.org/10.1029/2005JB004091

Seto, Y., Nishio-Hamane, D., Nagai, T., Sata, N., 2010. Development of a Software Suite on X-ray Diffraction Experiments. Rev. High Press. Sci. Technol. 20, 269–276. https://doi.org/10.4131/jshpreview.20.269

Shahar, A., Ziegler, K., Young, E.D., Ricolleau, A., Schauble, E.A., Fei, Y., 2009. Experimentally determined Si isotope fractionation between silicate and Fe metal and implications for Earth's core formation. Earth Planet. Sci. Lett. 288, 228–234. https://doi.org/10.1016/j.epsl.2009.09.025

Shibazaki, Y., Ohtani, E., Fukui, H., Sakai, T., Kamada, S., Ishikawa, D., Tsutsui, S., Baron, A.Q.R., Nishitani, N., Hirao, N., Takemura, K., 2012. Sound velocity measurements in dhcp-FeH up to 70 GPa with inelastic X-ray scattering: Implications for the composition of the Earth's core. Earth Planet. Sci. Lett. 313–314, 79–85. https://doi.org/10.1016/j.epsl.2011.11.002

Shibazaki, Y., Ohtani, E., Terasaki, H., Suzuki, A., Funakoshi, K., 2009. Hydrogen partitioning between iron and ringwoodite: Implications for water transport into the Martian core. Earth Planet. Sci. Lett. 287, 463–470. https://doi.org/10.1016/j.epsl.2009.08.034

Shibazaki, Y., Terasaki, H., Ohtani, E., Tateyama, R., Nishida, K., Funakoshi, K. ichi, Higo, Y., 2014. High-pressure and high-temperature phase diagram for Fe0.9Ni0.1-H alloy. Phys. Earth Planet. Inter. 228, 192–201. https://doi.org/10.1016/j.pepi.2013.12.013

Siebert, J., Badro, J., Antonangeli, D., Ryerson, F.J., 2013. Terrestrial accretion under oxidizing conditions. Science 339, 1194–1197. https://doi.org/10.1126/science.1227923

Siebert, J., Badro, J., Antonangeli, D., Ryerson, F.J., 2012. Metal-silicate partitioning of Ni and Co in a deep magma ocean. Earth Planet. Sci. Lett. 321–322, 189–197. https://doi.org/10.1016/j.epsl.2012.01.013

Stevenson, D.J., 1977. Hydrogen in the Earth's core. Nature 268, 130–131. https://doi.org/10.1038/268130a0

Suer, T.A., Siebert, J., Remusat, L., Menguy, N., Fiquet, G., 2017. A sulfur-poor terrestrial core inferred from metal–silicate partitioning experiments. Earth Planet. Sci. Lett. 469, 84–97. https://doi.org/10.1016/j.epsl.2017.04.016

Takahashi, E., 1986. Melting of a dry peridotite KLB-1 up to 14 GPa: Implications on the Origin of peridotitic upper mantle. J. Geophys. Res. 91, 9367. https://doi.org/10.1029/JB091iB09p09367

Takahashi, S., Ohtani, E., Ikuta, D., Kamada, S., Sakamaki, T., Hirao, N., Ohishi, Y., 2019. Thermal Equation of State of Fe_3C to 327 GPa and Carbon in the Core. Minerals 9, 744. https://doi.org/10.3390/min9120744

Tateno, S., Hirose, K., Komabayashi, T., Ozawa, H., Ohishi, Y., 2012. The structure of Fe-Ni alloy in Earth's inner core. Geophys. Res. Lett. 39, 2–5. https://doi.org/10.1029/2012GL052103

Tateno, S., Hirose, K., Ohishi, Y., Tatsumi, Y., 2010. The structure of iron in Earth's inner core. Science 330, 359–361. https://doi.org/10.1126/science.1194662

Tateno, S., Hirose, K., Sakata, S., Yonemitsu, K., Ozawa, H., Hirata, T., Hirao, N., Ohishi, Y., 2018. Melting Phase Relations and Element Partitioning in MORB to Lowermost Mantle Conditions. J. Geophys. Res. Solid Earth 123, 5515–5531. https://doi.org/10.1029/2018JB015790

Tateno, S., Kuwayama, Y., Hirose, K., Ohishi, Y., 2015. The structure of Fe–Si alloy in Earth's inner core. Earth Planet. Sci. Lett. 418, 11–19. https://doi.org/10.1016/j.epsl.2015.02.008

Tateno, S., Ozawa, H., Hirose, K., Suzuki, T., I-Kawaguchi, S., Hirao, N., 2019. Fe_2S: The Most Fe-Rich Iron Sulfide at the Earth's Inner Core Pressures. Geophys. Res. Lett. 46, 11944–11949. https://doi.org/10.1029/2019GL085248

Terasaki, H., Shibazaki, Y., Sakamaki, T., Tateyama, R., Ohtani, E., Funakoshi, K., Higo, Y., 2011. Hydrogenation of FeSi under high pressure. Am. Mineral. 96, 93–99. https://doi.org/10.2138/am.2011.3628

Thompson, E.C., Campbell, A.J., Tsuchiya, J., 2017. Elasticity of ε-FeOOH: Seismic implications for Earth's lower mantle. J. Geophys. Res. Solid Earth 122, 5038–5047. https://doi.org/10.1002/2017JB014168

Thompson, E.C., Davis, A.H., Bi, W., Zhao, J., Alp, E.E., Zhang, D., Greenberg, E., Prakapenka, V.B., Campbell, A.J., 2018. High-Pressure Geophysical Properties of *Fcc* Phase FeH_x. Geochemistry, Geophys. Geosystems 19, 305–314. https://doi.org/10.1002/2017GC007168

Tsujino, N., Nishihara, Y., Nakajima, Y., Takahashi, E., Funakoshi, K., Higo, Y., 2013. Equation of state of γ-Fe: Reference density for planetary cores. Earth Planet. Sci. Lett. 375, 244–253. https://doi.org/10.1016/j.epsl.2013.05.040

Tsumuraya, T., Matsuura, Y., Shishidou, T., Oguchi, T., 2012. First-Principles Study on the Structural and Magnetic Properties of Iron Hydride. J. Phys. Soc. Japan 81, 064707. https://doi.org/10.1143/JPSJ.81.064707

Tsuno, K., Frost, D.J., Rubie, D.C., 2013. Simultaneous partitioning of silicon and oxygen into the Earth's core during early Earth differentiation. Geophys. Res. Lett. 40, 66–71. https://doi.org/10.1029/2012GL054116

Umemoto, K., Hirose, K., 2020. Chemical compositions of the outer core examined by first principles calculations. Earth Planet. Sci. Lett. 531, 116009. https://doi.org/10.1016/j.epsl.2019.116009

Umemoto, K., Hirose, K., 2015. Liquid iron-hydrogen alloys at outer core conditions by first-principles calculations. Geophys. Res. Lett. 42, 7513–7520. https://doi.org/10.1002/2015GL065899

Vočadlo, L., Alfé, D., Gillan, M.J., Price, G.D., 2003. The properties of iron under core conditions from first principles calculations. Phys. Earth Planet. Inter. 140, 101–125. https://doi.org/10.1016/j.pepi.2003.08.001

Wade, J., Wood, B.J., 2005. Core formation and the oxidation state of the Earth. Earth Planet. Sci. Lett. 236, 78–95. https://doi.org/10.1016/j.epsl.2005.05.017

Wakamatsu, T., Ohta, K., Yagi, T., Hirose, K., Ohishi, Y., 2018. Measurements of sound velocity in iron–nickel alloys by femtosecond laser pulses in a diamond anvil cell. Phys. Chem. Miner. 0, 0. https://doi.org/10.1007/s00269-018-0944-3

Walsh, K.J., Morbidelli, A., Raymond, S.N., O'Brien, D.P., Mandell, A.M., 2011. A low mass for Mars from Jupiter's early gas-driven migration. Nature 475, 206–209. https://doi.org/10.1038/nature10201

Williams, C.D., Mukhopadhyay, S., 2019. Capture of nebular gases during Earth's accretion is preserved in deep-mantle neon. Nature 565, 78–81. https://doi.org/10.1038/s41586-018-0771-1

Wood, B.J., Li, J., Shahar, A., 2013. Carbon in the Core: Its Influence on the Properties of Core and Mantle. Rev. Mineral. Geochemistry. https://doi.org/10.2138/rmg.2013.75.8

Wood, B.J., Walter, M.J., Wade, J., 2006. Accretion of the Earth and segregation of its core. Nature 441, 825–833. https://doi.org/10.1038/nature04763

Wu, J., Desch, S.J., Schaefer, L., Elkins-Tanton, L.T., Pahlevan, K., Buseck, P.R., 2018. Origin of Earth's Water: Chondritic Inheritance Plus Nebular Ingassing and Storage of Hydrogen in the Core. J. Geophys. Res. Planets 123, 2691–2712. https://doi.org/10.1029/2018JE005698

Yamakata, M., Yagi, T., Utsumi, W., Fukai, Y., 1992. In situ X-ray Observation of Iron Hydride under High Pressure and High Temperature. Proc. Japan Acad. Ser. B Phys. Biol. Sci. 68, 172–176. https://doi.org/10.2183/pjab.68.172

Yamamoto, K., Sakamoto, N., Yurimoto, H., 2010. Analysis of the noise properties of a solid-state SCAPS ion imager and development of software noise reduction. Surf. Interface Anal. 42, 1603–1605. https://doi.org/10.1002/sia.3599

Yi-Jing, D., Tzu-Tung, Y., Li-Rong, C., 1985. Theoretical Calculation of the Mole Fraction at the Eutectic Point for a Binary System. Phys. status solidi 130, K5–K10. https://doi.org/10.1002/pssb.2221300142

Ying, J., Zhao, J., Bi, W., Alp, E.E., Xiao, Y., Chow, P., Shen, G., Struzhkin, V. V., 2020. Magnetic phase diagram of ε'- FeH. Phys. Rev. B 101, 020405. https://doi.org/10.1103/PhysRevB.101.020405

Yoo, C.S., Cynn, H., Söderlind, P., Iota, V., 2000. New β(fcc)-Cobalt to 210 GPa. Phys. Rev. Lett. 84, 4132–4135. https://doi.org/10.1103/PhysRevLett.84.4132

Yoshimura, S., 2015. Diffusive fractionation of H_2O and CO_2 during magma degassing. Chem. Geol. 411, 172–181. https://doi.org/10.1016/j.chemgeo.2015.07.003

Yurimoto, H., Nagashima, K., Kunihiro, T., 2003. High precision isotope micro-imaging of materials, in: Applied Surface Science. pp. 793–797. https://doi.org/10.1016/S0169-4332(02)00825-5

Appendix. Nuclear resonant X-ray scattering of Fe-Si-H at high pressures

This appendix has been prepared by ***Shoh Tagawa****, Yoichi Nakajima, and Kei Hirose*.

1. Introduction

Besides the density measurement at high pressures (Chapter 4), V_P and V_S are essential information to constrain the hydrogen contents in the core. A Birch plot, which is a graph with velocity vs. density, enables direct comparison between a candidate of the core material and PREM. The low V_S in the solid inner core is the most critical problem for the quest to determine the light elements because it is substantially slower than that of Fe alloys, and no composition model agrees. So far, the incorporation of carbon (Chen et al., 2014; Li et al., 2018) and the "premelting" effect (Martorell et al., 2013) have been proposed, but it is still an open question.

Nuclear resonant X-ray scattering (NIS) provides a way of determining the phonon density of states (PDOS) by excitation of nuclear resonance of ^{57}Fe. The low-energy part of the PDOS renders Debye sound velocity, V_D (Hu et al., 2003). If an equation of state (EoS) and the Grüneisen parameter, γ, was determined, V_D yields V_S and V_P. For FeH*x*, several previous studies were provided (Mao et al., 2004; Thompson et al., 2018). They positively concluded hydrogen could be in the core, but still, the ρ-V_S curve of FeH*x* deviated from the PREM. This study aims to reveal the effect of the incorporation of silicon on the V_S of solid FeH*x*.

2. Experimental method

In order to perform nuclear inelastic scattering (NIS) measurements, we synthesized an *hcp* Fe-Si hydride sample from the reaction of ^{57}Fe-enriched $Fe_{0.88}Si_{0.12}$ foil with hydrogen. An ingot of $Fe_{0.88}Si_{0.12}$ (6.4 wt.%Si) enriched with 95% ^{57}Fe was prepared by the arc melting method (Rare Metallic, Co. Ltd.). A foil with approximately 30 × 30 × 5 μm^3 size was cut from a piece of the ingot. We used a panoramic diamond anvil cell (p-DAC) designed for NIS measurements, which was similar to that used in previous works (*e.g.* Mao et al., 2001). The cullet size of diamond anvils was 150 μm. Beryllium was used as the gasket, which was pre-indented to ~20 μm thickness, and then a hole with ~60 μm diameter was drilled as the sample chamber. The ^{57}Fe-enriched $Fe_{0.88}Si_{0.12}$ foil was placed into the sample chamber. Liquid hydrogen was loaded into the chamber at temperatures below 20 K and at 1 bar using a liquid hydrogen loading system. The sample with hydrogen was then compressed to ~30 GPa at below 50 K in order to avoid the formation of the *dhcp* phase. After the cold compression, the sample with hydrogen was heated to room temperature and then decompressed to ~10 GPa. The pressure was determined based on the Raman shift of diamond anvils (Akahama and Kawamura, 2004). The presence of hydrogen in the sample chamber was confirmed by the hydrogen vibron mode using Raman spectroscopy.

In order to confirm the synthesis of $Fe_{0.88}Si_{0.12}H_x$, we performed *in situ* XRD measurements at the beamline BL10XU of the SPring-8 synchrotron facility (Ohishi et al., 2008).

A monochromatic X-ray beam of ~30 keV was focused down to ~7 μm and XRD patterns were collected using an imaging plate (*RIGAKU,* R-AXIS IV) or a flat panel detector (*Perkin Elmer*). The XRD patterns were analyzed by using IP Analyzer and PD Indexer software packages (Seto et al., 2010).

The NIS measurements on the synthesized $Fe_{0.88}Si_{0.12}Hx$ were carried out at the beamline BL09XU of the SPring-8 synchrotron facility (Yoda et al., 2007). The storage ring was operated with the 11 bunch-train × 29 mode in which each bunch was separated by 145.5 ns. We used a high-energy resolution monochromatic X-ray beam with an energy width of ~2.5 meV at 14.4125 keV of ^{57}Fe Mössbauer nuclear resonance energy. The energy resolution during NIS measurements was monitored by the nuclear resonant scattering from a ^{57}Fe foil placed in the backward direction from p-DAC. The monochromatic X-ray was focused down to 10 × 5 μm^2 (full width at half of the maximum) by a Kirkpatrick-Baez mirror system. The inelastic scattering signals from the sample were collected by three avalanche photodiode detectors, which were located at ~4 mm distance from the sample and in the radial direction to the X-ray beam. NIS spectra were collected in an energy range of -60 to +80 meV around the ^{57}Fe Mössbauer nuclear resonance energy, with an energy step of 0.4 meV and a collection time of 6 s at each step. We measured NIS spectra in a pressure range of 9.6 to 81 GPa at 300 K, with a total collection time of 8 to 12 hrs at each pressure. The pressure was checked before and after each NIS measurement,

and the change of pressure was within 1 GPa. The averaged pressure before and after each measurement represented the experimental pressure. The uncertainty of pressure was estimated to be 5%. The collected NIS spectra were analyzed with the PHOENIX software (Sturhahn, 2000) to obtain the partial phonon density of state (PDOS) of ^{57}Fe in the iron sublattice and the sound velocities of the sample.

3. Result

(1) XRD measurements

The X-ray diffraction patterns of the ^{57}Fe-enriched $Fe_{0.88}Si_{0.12}$ sample with hydrogen were obtained in a pressure range of 11.9 to 81 GPa (Figure A1). The XRD data at 11.9 GPa were collected upon decompression at 300 K from ~ 30 GPa after the cold compression. The XRD at higher pressures was collected after some of the NIS measurements. All peaks from the samples were assigned with the *hcp* structure as well as reported in Chapter 4. The *hcp* phase was stable up to 81 GPa. The observed volume of the *hcp* phase was larger than those of *hcp* Fe (Dewaele et al., 2006) and *hcp* $Fe_{0.88}Si_{0.12}$ (Tateno et al., 2015) estimated at an equivalent pressure using the equations of state (Figure A2). This can be due to the formation of $Fe_{0.88}Si_{0.12}H_x$ in the present experiment.

The XRD measurements of the present sample at 11.9 GPa exhibit a single *hcp* phase and a fairly uniform volume within ±0.4% through the sample foil. The sample was decompressed to

11.9 GPa at room temperature after cold compression in this study. The decompression to ~10 GPa at room temperature after cold compression may homogenize the hydrogen distribution in *hcp* $Fe_{0.88}Si_{0.12}Hx$, whereas in Chapter 4 the *hcp* $Fe_{0.88}Si_{0.12}Hx$ was synthesized by annealing the sample to ~1000 K at 27 GPa In addition, the $Fe_{0.88}Si_{0.12}$ foil was surrounded by thermal insulator NaCl, whereas the sample foil contacted directly with hydrogen without any pressure medium.

To evaluate the elastic behavior and hydrogen concentration in the present *hcp* $Fe_{0.88}Si_{0.12}Hx$ sample, we construct the equation of state (EoS) from the present compression volume data. We fit the Vinet EoS (Vinet et al., 1987) to the obtained pressure-volume (P-V) data (Table A1). Assuming the $K'_0 = 4.8$ as that for *hcp* $Fe_{0.88}Si_{0.12}H_{0.61}$ (Tagawa et al., 2016), we obtained $V_0 = 23.08 \pm 0.06$ Å^3 and $K_0 = 204.7 \pm 6.6$ GPa. The compression curves among hydrogen-bearing and -free Fe-Si alloys are almost parallel to each other (Figure A2).

Following the procedure by Tagawa et al. (2016), we estimate the hydrogen concentration in the present *hcp* $Fe_{0.88}Si_{0.12}Hx$ sample. It is well known that hydrogen dissolves interstitially to host metals and then expands the metal volumes (Fukai, 1992). The volume of *hcp* $FeD_{0.42}$ at 1 bar was reported based on neutron diffraction measurements (Antonov et al., 1998). By comparing the volume difference between *hcp* $FeD_{0.42}$ and *hcp* Fe (Dewaele et al., 2006), the volume of an interstitial hydrogen atom (ΔV_H) in *hcp* $FeD_{1.0}$ is estimated to be 2.017 Å^3 per formula unit at 1 bar (note that the number of formula unit Z = 2 in the *hcp* structure). The V_0

difference of the present *hcp* $Fe_{0.88}Si_{0.12}Hx$ ($V_0 = 23.08 \pm 0.06$ Å^3) from *hcp* $Fe_{0.88}Si_{0.12}$ ($V_0 = 22.49$ Å^3) is 0.29 ± 0.03 Å^3 per formula unit. The used EoS parameters for *hcp* $Fe_{0.88}Si_{0.12}$ was obtained from the re-analysis of the P-V data reported by Tateno et al. (2015). With the atomic hydrogen volume in *hcp* $FeD_{1.0,}$ the composition of the present sample is calculated to *hcp* $Fe_{0.88}Si_{0.12}H_{0.15\pm0.05}$. The uncertainty of the hydrogen content was obtained based on the errors of its elastic parameters and the observed volume in XRD measurements.

(2) NIS measurements

The NIS spectra of ^{57}Fe-enriched *hcp* $Fe_{0.88}Si_{0.12}H_{0.15\pm0.05}$ were collected at room temperature of 300 K and 9.6, 24, 42, 64, and 81 GPa (Table A2). We analyzed the collected NIS spectra using the PHOENIX software (Sturhahn, 2000) and obtained the partial phonon density of state (PDOS) of ^{57}Fe in the sample (Figure A3). The relation between the PDOS D(E) and Debye sound velocity V_D can be described by Hu et al. (2003):

$$\lim_{E\to 0} \mathrm{D(E)} = \frac{m}{2\pi^2\hbar^3\rho V_D^3}\mathrm{E}^2 \qquad \text{(eq. A1)}$$

where E is the energy, m is the mass of the nuclear resonant isotope, $\hbar$ is the Planck constant, and ρ is the density of the material. This relation can be applied to a low-energy region. Figure A4 shows the D(E) and E^2 relations in a low energy range. We fitted eq. A1 to the PDOS data in an energy range of ~3.7 to 21.4 meV in order to obtain V_D. The used energy range was determined based on the χ^2 analysis to obtain the best fit. The ρ of *hcp* $Fe_{0.88}Si_{0.12}H_{0.15\pm0.05}$ at each pressure

was calculated using the EoS obtained by the present XRD measurements. The obtained V_D was given in Table A2.

Using the V_D data obtained by NIS measurements and EoS parameters by XRD measurements, we also obtained P-wave velocity (V_P) and S-wave velocity (V_S) at each pressure of NIS measurements. The thermodynamic relation among velocities and EoS parameters can be described by the following equations (Mao et al., 2001):

$$\frac{K_S}{\rho} = V_P^2 - \frac{4}{3}V_S^2 \quad \text{(eq. A2)}$$

$$\frac{3}{V_D^3} = \frac{1}{V_P^3} + \frac{2}{V_S^2} \quad \text{(eq. A3)}$$

where Ks is the adiabatic bulk modulus. Ks can be equivalent to the isothermal one K_T at 300 K. We obtained Ks and ρ at each pressure using the present EoS. With the V_D data, we obtained V_P and V_S via eqs. A2 and A3. The shear modulus *G* was also determined using the velocity and elastic parameters as following the definition $G = \rho V_S^2$. The obtained velocities and used elastic parameters are given in Table A2.

The relation between velocity and density of *hcp* $Fe_{0.88}Si_{0.12}H_{0.15}$ was obtained from the application of Birch's law (Birch, 1961) to the present observations. The V_D, V_P, and V_S data obtained from NIS measurements are plotted as a function of density in Figure A5. Birch's law predicts a linear relationship between the velocity and density of materials. Based on the Birch's law, we fitted a linear curve $V_{P, S}$ [km] = a + b ρ [g/cm3], where a and b are the constant values to

the obtained V_P and V_S data. Because the slopes of V_P and V_S were found to change between 9.6 GPa and 24 GPa in the present study (Figure A5), we fit the linear curves to the data collected above 20 GPa. The relatively smaller velocities at 9.6 GPa can be due to a magnetic transition in *hcp* $Fe_{0.88}Si_{0.12}H_{0.15}$. Previous Mössbauer spectroscopy measurements show that the loss of magnetism in *dhcp* FeH*x* occurs at ~22 GPa, which causes the change in the slopes of its velocities along pressure and density (Mao et al., 2004). The slope changes observed in this study can also indicate the change of magnetic structure in *hcp* $Fe_{0.88}Si_{0.12}H_{0.15}$. The fitted parameters to velocity-density data of the present sample above 20 GPa are a = -0.57±0.36 km/s and b = 0.548 ± 0.039 (km/s)/(g/cm^3) for V_D, a = -2.91±0.33 km/s and b = 1.217 ±0.036 (km/s)/(g/cm^3) for V_P, and a = -0.41± 0.35 km/s and b =0.477 ±0.038 (km/s)/(g/cm^3) for V_S.

Hydrogen was found to have a relatively strong effect on the P-wave velocity but small on the S-wave velocity of *hcp* Fe alloys. The V_P and V_S of the present ^{57}Fe-enriched *hcp* $Fe_{0.88}Si_{0.12}H_{0.15}$ obtained in this study are compared with ^{57}Fe-enriched *hcp* $Fe_{0.85}Si_{0.15}$ (Lin et al., 2003) and *hcp* Fe (Murphy et al., 2013) reported in previous NIS measurements (Figure A6). Combining Birch's law and EoS for *hcp* $Fe0_{.88}Si_{0.12}H_{0.15}$, the velocity-pressure profiles were obtained. The profiles for *hcp* $Fe_{0.85}Si_{0.15}$ (Lin et al., 2003) and Fe (Murphy et al., 2013) are based on the previous NIS measurements. The V_P of *hcp* $Fe0_{.88}Si_{0.12}H_{0.15}$ is larger by ~4.5% and ~1.2% than those of *hcp* Fe and $Fe_{0.85}Si_{0.15}$, respectively, which corresponding to ~0.2% increase of V_P

by the addition of one atomic hydrogen into *hcp* Fe alloys. On the other hand, the effect of hydrogen on V_S can be much gentle relative to that on V_P because the V_S of the present hydride is almost the same as that of *hcp* $Fe0_{.85}Si_{0.15}$ (Lin et al., 2003). The present measurements indicate the effect of hydrogen on V_S can be much smaller than that on V_P.

4. Discussion

The slope in the V_P-ρ plot of the present *hcp* $Fe_{0.88}Si_{0.12}H_{0.15}$ is similar or slightly smaller by 10% than that of *hcp* $Fe_{0.85}Si_{0.15}$ (Lin et al., 2003) (Figure A7). Those of *fcc* FeH*x* (Thompson et al., 2018) and *dhcp* FeH*x* (Shibazaki et al., 2012) are lower by 1.7% and 12%, respectively, relative to that of *hcp* Fe (Murphy et al., 2013). The hydrogen concentrations of the nearly stoichiometric hydrides (x = ~1) in the previous studies are much higher than the present one (x = 0.15). The effect of hydrogen concentrations on the slope can be limited. Much large-reduction in the slope by hydrogen was expected based on the V_P-ρ data of *dhcp* FeH*x* by Mao et al. (2004), which can be due to slightly scattered data in their study.

The effect of hydrogen on the V_S-ρ slope of *hcp* Fe alloys can be more limited. The slope in the V_S-ρ of *hcp* $Fe_{0.88}Si_{0.12}H_{0.15}$ is almost identical to those of *hcp* $Fe_{0.85}Si_{0.15}$ and *hcp* Fe. On the other hand, the slopes for *dhcp* FeH*x* (Mao et al., 2004) and *fcc* FeH*x* (Thompson et al., 2018) are more gently, which are smaller by 26-45% than that of *hcp* $Fe_{0.88}Si_{0.12}H_{0.15}$. When assuming a linear relationship between the slope and hydrogen content based on the results on *dhcp* FeH*x*

and *fcc* FeH*x*, it is expected to reduce the slope of the present *hcp* $Fe_{0.88}Si_{0.12}H_{0.15}$ by 4-7%. Such a small difference is similar to the uncertainty of the present result for *hcp* $Fe_{0.88}Si_{0.12}H_{0.15}$, so that it can be difficult to observe in this study. Alternatively, the V_S can be more sensitive to the structure relative to that for the V_P. Theoretical calculations (Martorell et al., 2015) at inner core conditions exhibit that the V_S of Fe depends on structures between *fcc* and *hcp*, whereas the V_P is insensitive to the structural differences. Although the structure effect on V_S was observed only at high temperatures in the simulations, the differences of the V_S-ρ slope between *hcp* $Fe_{0.88}Si_{0.12}H_{0.15}$ and nearly stoichiometric *dhcp* and *fcc* hydrides could be caused by the structure effect.

The V_P of *hcp* $Fe_{0.88}Si_{0.12}H_{0.15}$ is larger by 4.2% at 9 g/cm^3 (near the middle pressure of the present experimental conditions) with respect to that of *hcp* $Fe_{0.85}Si_{0.15}$ (Figure A7), which corresponding to 28% increases by the addition of one atomic hydrogen in the formula unit (x = 1). The effect of hydrogen estimated from *hcp* $Fe_{0.88}Si_{0.12}H_{0.15}$ relative to *hcp* $Fe_{0.85}Si_{0.15}$ are located between the differences of 24% for *dhcp* FeH*x* (Mao et al., 2004) and 32% for *fcc* FeH*x* (Thompson et al., 2018) relative to *hcp* Fe. The relatively higher V_P for *dhcp* FeH*x* with the natural isotope Fe by Shibazaki et al. (2012) is largely due to the isotopic difference from ^{57}Fe used in NIS measurements. Because the V_P-ρ slope for *hcp* $Fe_{0.88}Si_{0.12}H_{0.15}$ is slightly lower than that of *hcp* $Fe_{0.85}Si_{0.15}$, the reduction effect of hydrogen on the V_P of *hcp* $Fe_{0.85}Si_{0.15}$ might be smaller at higher densities >11 g/cm^3. Recent IXS measurements on Fe-Si alloys (Antonangeli et al., 2018;

Mao et al., 2012), however, reported a more gentle slope compared with that by Lin et al. (2003) and rather a similar one to *hcp* Fe. When comparing the V_S of *hcp* $Fe_{0.88}Si_{0.12}H_{0.15}$ with that of *hcp* Fe (Murphy et al., 2013), the difference of V_P of *hcp* $Fe_{0.88}Si_{0.12}H_{0.15}$ is almost constant at 21–22% in the present density range and even much higher densities >11 g/cm^3.

The V_S of *hcp* $Fe_{0.88}Si_{0.12}H_{0.15}$ is almost the same as that of *hcp* $Fe_{0.85}Si_{0.15}$ (Lin et al., 2003) (Figure A7). This indicates that the hydrogen effect on V_S of *hcp* Fe-Si alloys can be negligible at a constant density. Contrary, the V_S of nearly stoichiometric *dhcp* and *fcc* FeH*x* (Mao et al., 2004; Thompson et al., 2018) exhibits significant difference of 21-23 % at 9 g/cm^3 relative to that of *hcp* Fe (Murphy et al., 2013), which cannot be explained simply by the differences of hydrogen concentration. As discussed early on the V_S-ρ slopes among the hydrides, the structural differences may cause these changes in the effect of hydrogen on the V_S of Fe. Theoretical calculations on *hcp* FeH*x* show that hydrogen increases both V_P and V_S by a similar ratio to the hydrogen content at a given pressure (Caracas, 2015). However, such an effect of hydrogen on V_S can be much smaller than the previous calculations.

Contrary to the density comparison of Fe-Si-H alloys with the seismological observations (Chapter 4), we cannot find any reasonable compositions to explain the sound velocities of the solid inner core. Both V_P and V_S of *hcp* Fe are estimated to be higher than those of the inner core. As shown earlier, both Si and H increase the V_P of *hcp* Fe. As a result, the V_P of *hcp* $Fe_{0.88}Si_{0.12}H_{0.15}$

is 5% larger than that of *hcp* Fe (Murphy et al., 2013) at ICB conditions, which is 7% larger than the inner core. The V_S of *hcp* $Fe_{0.88}Si_{0.12}H_{0.15}$ is slightly lower by 2.4% than that of *hcp* Fe. However, the V_S is much larger by 27% relative to the seismological observations. The lower V_S of *hcp* $Fe_{0.88}Si_{0.12}H_{0.15}$ relative to that of *hcp* Fe is contributed mainly by Si, so that the addition of more Si into Fe may reduce the V_S. However, the addition of Si can also increase the V_P and decrease the ρ of Fe, which cause the contradiction to those of the inner core. Therefore, the enhancement of Si relative to the present sample will not be realistic.

However, the temperature effect could lower Vs. In high temperatures, hydrogen atoms in *hcp* FeH*x* would behave like a fluid (Fukai and Sugimoto, 1985). Such fluid-like behavior of hydrogen could weaken the bonds between iron atoms, decrease the *G* and then V_S of Fe–H–X alloys, which would bring about a similar effect to "premelting" (Martorell et al., 2013). Furthermore, the V_S in high temperatures should be on a different Birch's plot, which was confirmed experimentally on pure Fe (Lin et al., 2005). Therefore, whether the fluid-like behavior of hydrogen reduces V_S at high temperatures should be tested. This is the remaining problem for confirming the hypothesis of hydrogen in the core.

Figures and tables

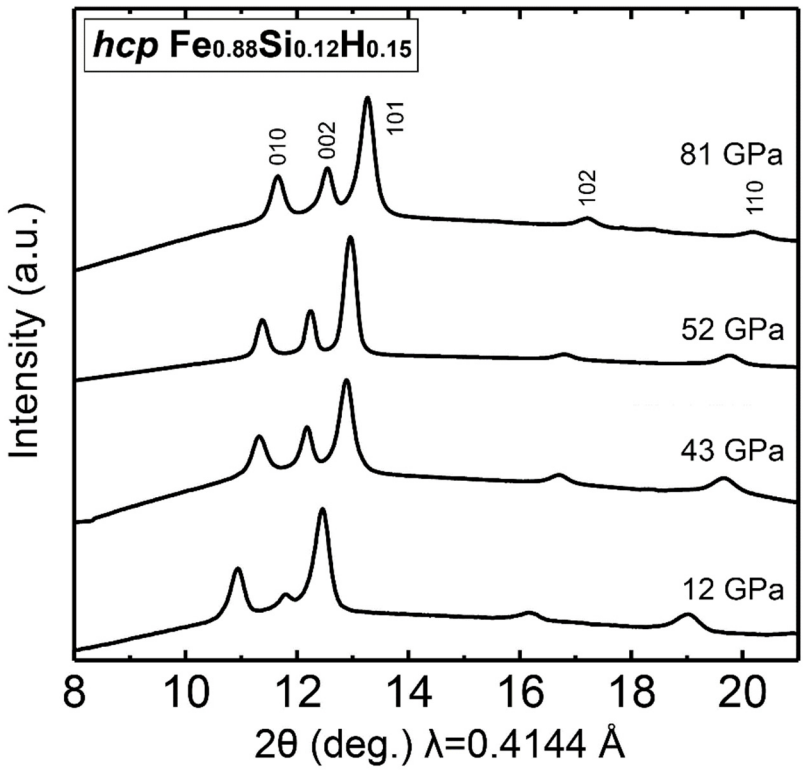

Figure A1. X-ray diffraction patterns of *hcp* $Fe_{0.88}Si_{0.12}H_x$

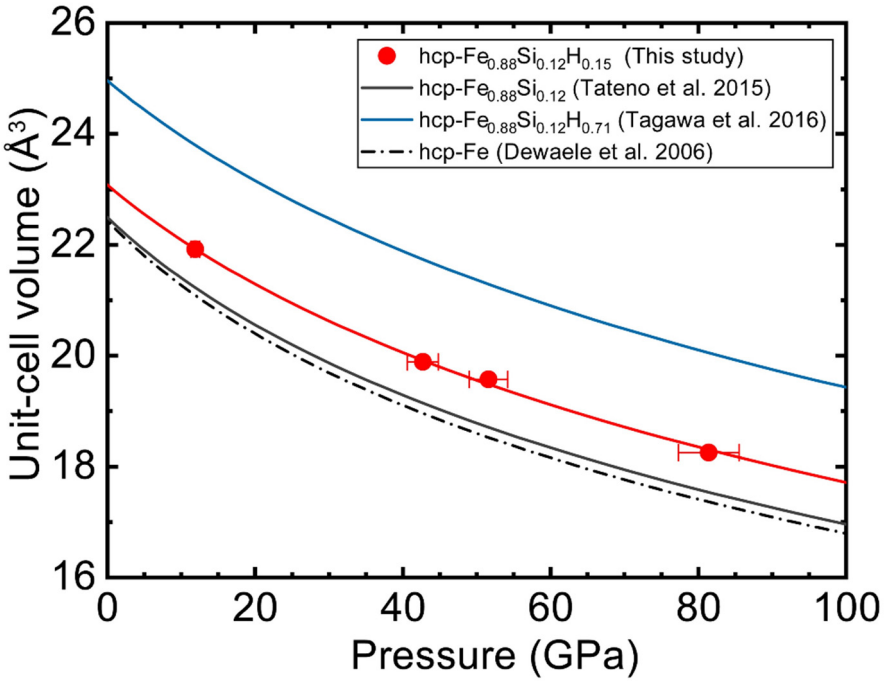

Figure A2. Compression of P-V data of *hcp* $Fe_{0.88}Si_{0.12}Hx$

The volume data of *hcp* $Fe_{0.88}Si_{0.12}Hx$ observed in this study are shown by red symbols. The red curve is the fitting result of the Vinet equation of state to the present data. The compression curves for hcp-Fe (broken black), $Fe_{0.88}Si_{0.12}$ (solid black) by Tateno et al. (2015) and *hcp* $Fe_{0.88}Si_{0.12}H_{0.71}$ (solid blue) in Chapter 4 are also shown for the comparison.

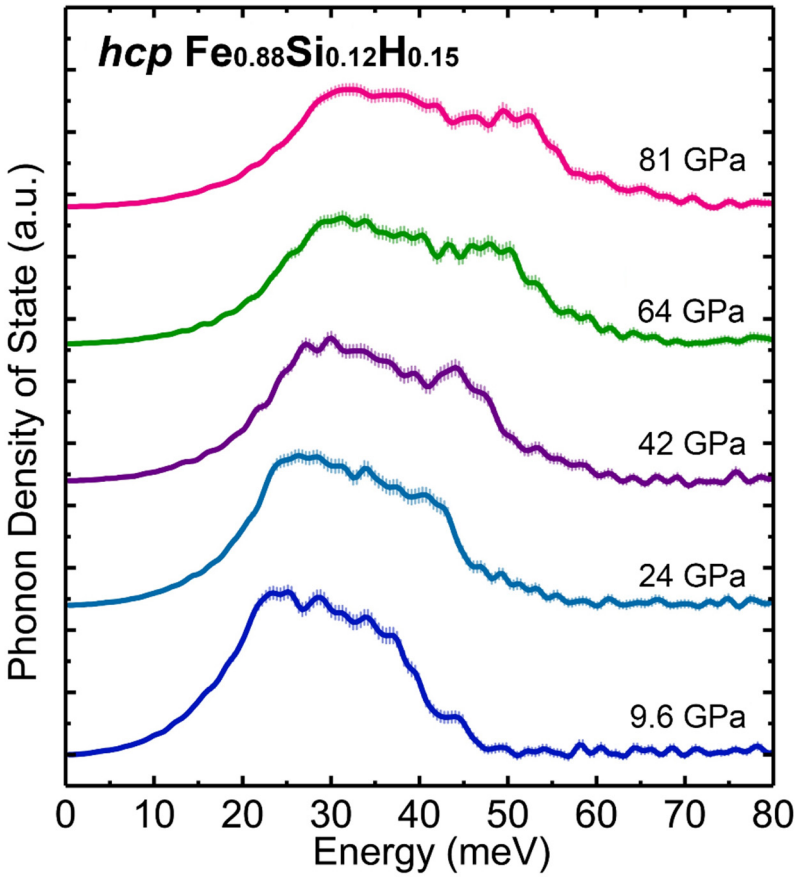

Figure A3. Partial phonon density of state of ^{57}Fe in hcp-$Fe_{0.88}Si_{0.12}H_x$ on elevating pressure
The phonon DOS (solid lines) were extracted from the NIS data obtained from 9.6 to 81 GPa. Vertical bars around the solid lines represent the uncertainty at each data point.

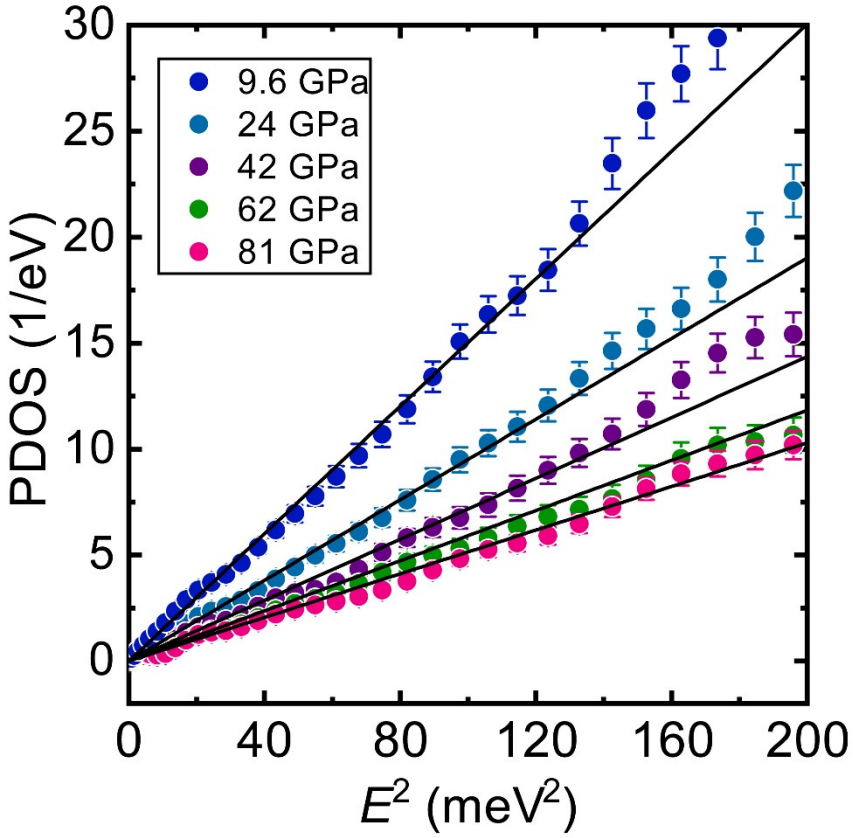

Figure A4. PDOS of *hcp* $Fe_{0.88}Si_{0.12}H_{0.15}$ as a function of the squared energy

Debye velocity at each pressure was obtained by a linear fit (solid line) to the PDOS-E^2 data in a low energy range. The used energy range was determined based on the χ^2 analysis in fitting with changing the energy ranges.

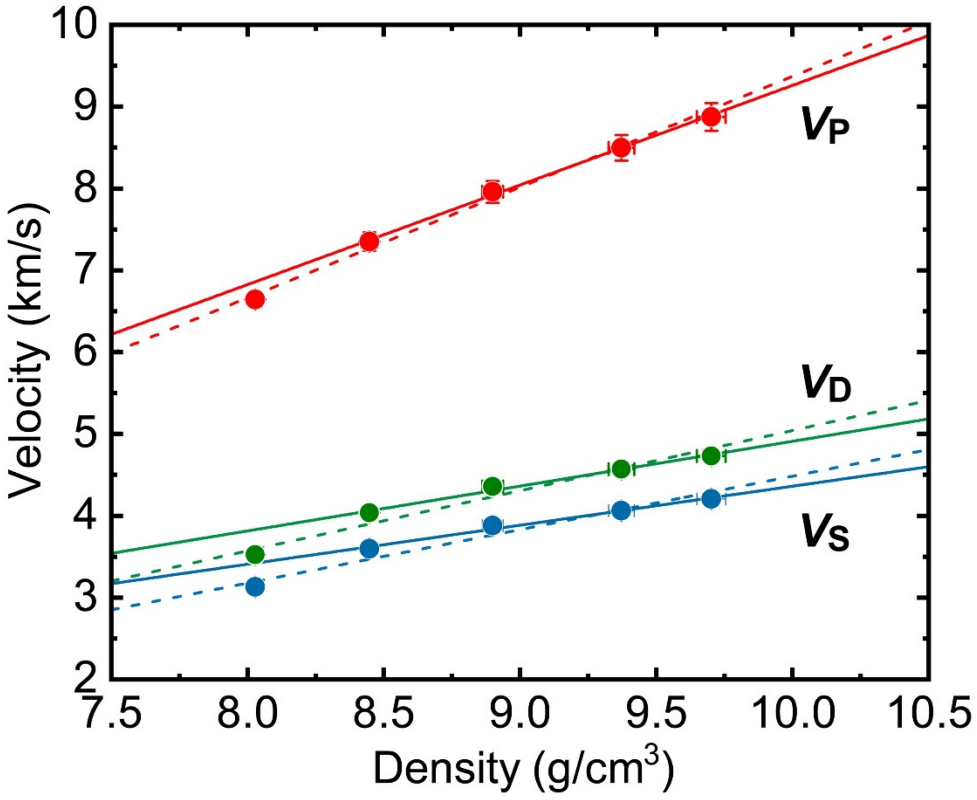

Figure A5. Velocity and density relation of *hcp* $Fe_{0.88}Si_{0.12}H_{0.15}$

Debye velocity (V_D), P-wave velocity (V_P), and S-wave velocity (V_S) are plotted as a function of density. The solid lines are the fitting results of the Birch's linear relation to the data above 20 GPa. For comparison, the fitting results with all data are also shown (broken lines).

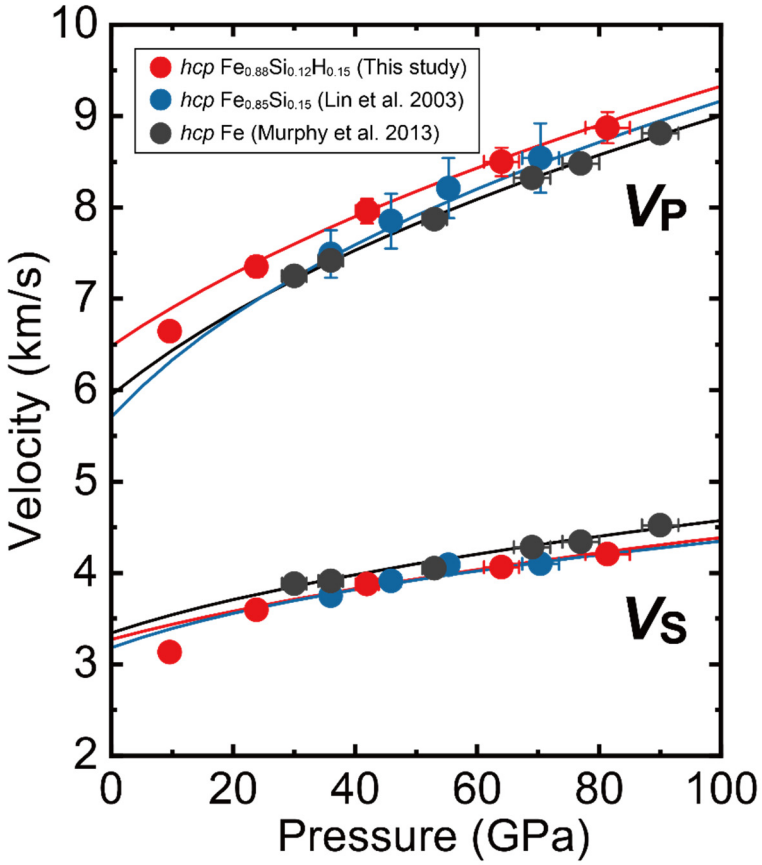

Figure A6. Sound velocities of *hcp* $Fe_{0.88}Si_{0.12}H_{0.15}$ as a function of pressure

P-wave velocity (V_P), and S-wave velocity (V_S) of *hcp* $Fe_{0.88}Si_{0.12}H_{0.15}$ (red) are plotted, which are compared with those of *hcp* $Fe_{0.85}Si_{0.15}$ (blue) and *hcp* Fe (black) reported in previous NIS measurements (Lin et al., 2003; Murphy et al., 2013). The solid lines represent the pressure effect on the V_P and V_S based on the velocity and density linear relations above 20 GPa and EoSs (see the detail in text).

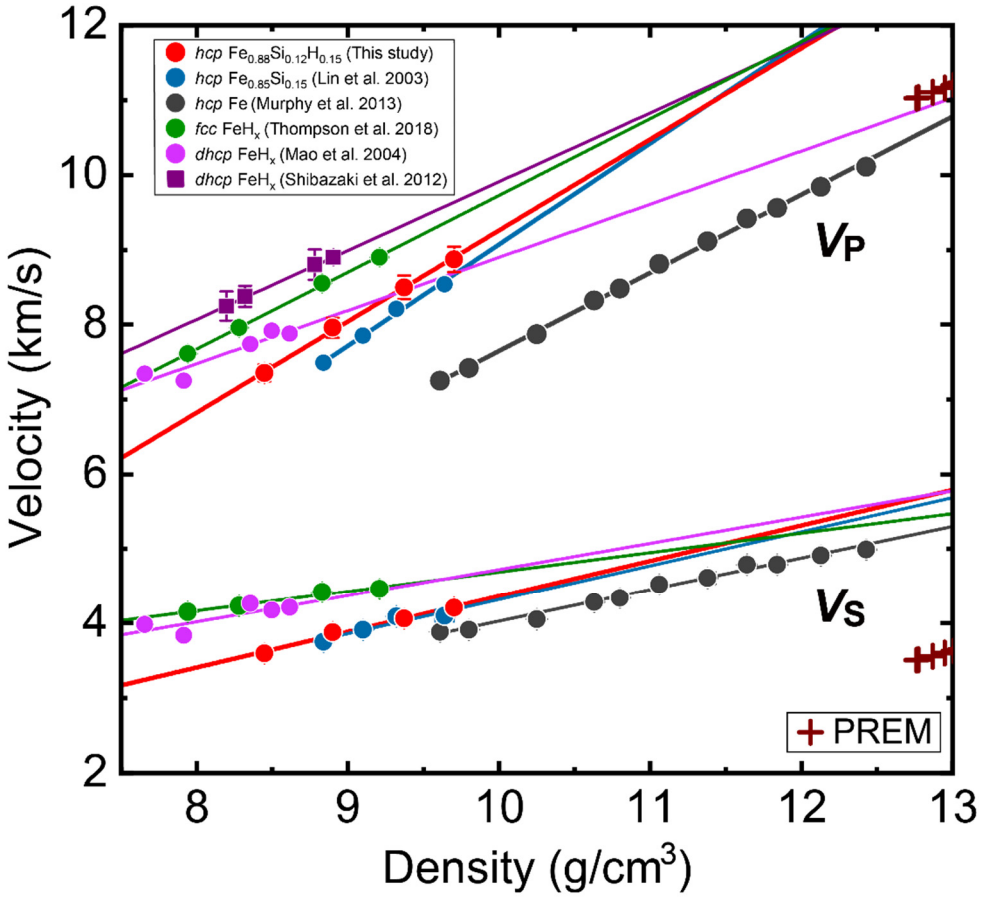

Figure A7. Birch's plots of *hcp* $Fe_{0.88}Si_{0.12}H_{0.15}$

The P-wave velocity (V_P) and S-wave velocity (V_S) of *hcp* $Fe_{0.88}Si_{0.12}H_{0.15}$ are plotted as a function of density. The solid lines are the fitting result of velocity and density data. For comparison, other ^{57}Fe alloys based on NIS measurements are plotted: *hcp* Fe (Murphy et al., 2013), *hcp* $Fe_{0.85}Si_{0.15}$ (Lin et al., 2003), *dhcp* FeH*x* (Mao et al. 204), and *fcc* FeH*x* (Thompson et al. 2018). The IXS measurements on *dhcp* FeH*x* (Shibazaki et al. 2012) are also shown. The plotted data of FeH*x* by the previous measurements are for the nearly stoichiometric composition x = ~1.0 and non-magnetic phase.

Table A1. Volume of *hcp* $Fe_{0.88}Si_{0.12}Hx$

Pressure (GPa)	Volume (Å^3)	*a* (Å)	*c* (Å)	*x*†
11.9(6)	21.92(26)	2.507(4)	4.028(11)	0.13(5)
42.7(21)	19.89(18)	2.427(3)	3.902(7)	0.17(4)
51.6(26)	19.57(19)	2.414(3)	3.881(8)	0.20(5)
81.4(41)	18.25(25)	2.360(4)	3.785(10)	0.23(6)

The value in bracket is uncertainty relative to the last digit.

†The hydrogen concentration was calculated based on the volume differences from *hcp* $Fe_{0.88}Si_{0.12}Hx$ (Tagawa et al., 2016) and the atomic volume of hydrogen (Fukai 1992) at each pressure.

Table A2. Sound velocity and elastic parameters of *hcp* $Fe_{0.88}Si_{0.12}Hx$

Pressure† (GPa)	V_D (km/s)	V_P (km/s)	V_S (km/s)	ρ‡ (g/cm^3)	K_S‡ (GPa)	G (GPa)
9.6(5)	3.525(17)	6.643(91)	3.132(16)	8.03(3)	249.3(10)	78.8(1)
23.8(12)	4.037(25)	7.352(112)	3.594(23)	8.45(3)	311.1(14)	109.1(2)
42.0(21)	4.357(30)	7.959(134)	3.878(28)	8.90(4)	385.3(18)	133.8(2)
64.0(32)	4.568(35)	8.498(156)	4.061(32)	9.38(5)	470.6(23)	154.6(3)
81.4(41)	4.730(28)	8.873(170)	4.204(26)	9.71(6)	535.3(27)	171.5(3)

The value in bracket is the uncertainty relative to the last digit.

†The pressure was determined by averaging pressures before and after NIS measurements.

‡The parameters at each pressure were calculated from the EoS obtained in this apendix.

Table A3. The Birch's law parameters

	V_P		V_S		Reference
	a (km/s)	b (km/s)/ (g/cm^3)	a (km/s)	b (km/s)/ (g/cm^3)	
hcp $Fe_{0.88}Si_{0.12}H_{0.15}$	-0.29(33)	1.21(4)	-0.41(35)	0.48(4)	This study
dhcp FeH*x*	1.80(129)	0.71(16)	1.20(125)	0.35(15)	Mao et al. (2004)
dhcp FeH*x*	0.71(30)	0.92(3)	-	-	Shibazaki et a. (2012) †
fcc FeH*x*	-0.54(15)	1.03(2)	2.07(22)	0.26(3)	Thompson et al. (2018)
hcp $Fe_{0.85}Si_{0.15}$	-4.45(77)	1.35(8)	-0.25(117)	0.46(13)	Lin et al. (2003)
hcp Fe	-2.80(15)	1.04(2)†	-0.22(17)	0.42(2) †	Murphy et al. (2013)

The value in brackets is the uncertainty relative to the last digit.

†IXS measurements with isotopically natural Fe samples.

References

Akahama, Y., Kawamura, H., 2004. High-pressure Raman spectroscopy of diamond anvils to 250 GPa: Method for pressure determination in the multimegabar pressure range. J. Appl. Phys. 96, 3748–3751. https://doi.org/10.1063/1.1778482

Antonangeli, D., Morard, G., Paolasini, L., Garbarino, G., Murphy, C.A., Edmund, E., Decremps, F., Fiquet, G., Bosak, A., Mezouar, M., Fei, Y., 2018. Sound velocities and density measurements of solid hcp-Fe and hcp-Fe–Si (9 wt.%) alloy at high pressure: Constraints on the Si abundance in the Earth's inner core. Earth Planet. Sci. Lett. 482, 446–453. https://doi.org/10.1016/j.epsl.2017.11.043

Antonov, V.E., Cornell, K., Fedotov, V.K., Kolesnikov, A.I., Ponyatovsky, E.G., Shiryaev, V.I., Wipf, H., 1998. Neutron diffraction investigation of the dhcp and hcp iron hydrides and deuterides. J. Alloys Compd. 264, 214–222. https://doi.org/10.1016/S0925-8388(97)00298-3

Birch, F., 1961. The velocity of compressional waves in rocks to 10 kilobars: Part2. J. Geophys. Res. 66, 2199–2224. https://doi.org/10.1029/JZ066i007p02199

Caracas, R., 2015. The influence of hydrogen on the seismic properties of solid iron. Geophys. Res. Lett. 42, 3780–3785. https://doi.org/10.1002/2015GL063478

Chen, B., Li, Z., Zhang, D., Liu, J., Hu, M.Y., Zhao, J., Bi, W., Alp, E.E., Xiao, Y., Chow, P., Li, J., 2014. Hidden carbon in Earth's inner core revealed by shear softening in dense Fe_7C_3. Proc. Natl. Acad. Sci. 111, 17755–17758. https://doi.org/10.1073/pnas.1411154111

Dewaele, A., Loubeyre, P., Occelli, F., Mezouar, M., Dorogokupets, P.I., Torrent, M., 2006. Quasihydrostatic Equation of State of Iron above 2 Mbar. Phys. Rev. Lett. 97, 215504. https://doi.org/10.1103/PhysRevLett.97.215504

Fukai, Y., 1992. Some Properties of the Fe-H System at High Pressures and Temperatures, and their Implications for the Earth's Core, in: Syono, Y., Manghnani, M.H. (Eds.), High-Pressure Research: Applications to Earth and Planetary Sciences. pp. 373–385. https://doi.org/10.1029/GM067p0373

Fukai, Y., Sugimoto, H., 1985. Diffusion of hydrogen in metals. Adv. Phys. 34, 263–326. https://doi.org/10.1080/00018738500101751

Hu, M.Y., Sturhahn, W., Toellner, T.S., Mannheim, P.D., E. Brown, D., Zhao, J., Alp, E.E., 2003. Measuring velocity of sound with nuclear resonant inelastic x-ray scattering. Phys. Rev. B 67, 094304. https://doi.org/10.1103/PhysRevB.67.094304

Li, Y., Vočadlo, L., Alfè, D., Brodholt, J., 2018. Mg partitioning between solid and liquid iron under the Earth's core conditions. Phys. Earth Planet. Inter. 274, 218–221. https://doi.org/10.1016/j.pepi.2017.12.003

Lin, J.-F., Struzhkin, V. V., Sturhahn, W., Huang, E., Zhao, J., Hu, M.Y., Alp, E.E., Mao, H., Boctor, N., Hemley, R.J., 2003. Sound velocities of iron-nickel and iron-silicon alloys at high pressures. Geophys. Res. Lett. 30, 2112. https://doi.org/10.1029/2003GL018405

Lin, J.-F., Sturhahn, W., Zhao, J., Shen, G., Mao, H., Hemley, R.J., 2005. Sound Velocities of Hot Dense Iron: Birch's Law Revisited. Science 308, 1892–1894. https://doi.org/10.1126/science.1111724

Mao, H.K., Xu, J., Struzhkin, V. V, Shu, J., Hemley, R.J., Sturhahn, W., Hu, M.Y., Alp, E.E., Vocadlo, L., Alfè, D., Price, G.D., Gillan, M.J., Schwoerer-Böhning, M., Häusermann, D., Eng, P., Shen, G., Giefers, H., Lübbers, R., Wortmann, G., 2001. Phonon Density of States of Iron up to 153 Gigapascals. Science 292, 914 LP – 916. https://doi.org/10.1126/science.1057670

Mao, W.L., Sturhahn, W., Heinz, D.L., Mao, H.K., Shu, J., Hemley, R.J., 2004. Nuclear resonant x-ray scattering of iron hydride at high pressure. Geophys. Res. Lett. 31, 3–6. https://doi.org/10.1029/2004GL020541

Mao, Z., Lin, J.-F., Liu, J., Alatas, A., Gao, L., Zhao, J., Mao, H.-K., 2012. Sound velocities of Fe and Fe-Si alloy in the Earth's core. Proc. Natl. Acad. Sci. 109, 10239–10244. https://doi.org/10.1073/pnas.1207086109

Martorell, B., Brodholt, J., Wood, I.G., Vočadlo, L., 2015. The elastic properties and stability of *fcc*-Fe and *fcc*-FeNi alloys at inner-core conditions. Geophys. J. Int. 202, 94–101. https://doi.org/10.1093/gji/ggv128

Martorell, B., Vocadlo, L., Brodholt, J., Wood, I.G., 2013. Strong premelting effect in the elastic properties of *hcp*-Fe under inner-core conditions. Science 342, 466–468. https://doi.org/10.1126/science.1243651

Murphy, C.A., Jackson, J.M., Sturhahn, W., 2013. Experimental constraints on the thermodynamics and sound velocities of *hcp*-Fe to core pressures. J. Geophys. Res. Solid Earth 118, 1999–2016. https://doi.org/10.1002/jgrb.50166

Ohishi, Y., Hirao, N., Sata, N., Hirose, K., Takata, M., 2008. Highly intense monochromatic X-ray diffraction facility for high-pressure research at SPring-8. High Press. Res. 28, 163–173. https://doi.org/10.1080/08957950802208910

Seto, Y., Nishio-Hamane, D., Nagai, T., Sata, N., 2010. Development of a Software Suite on X-ray Diffraction Experiments. Rev. High Press. Sci. Technol. 20, 269–276. https://doi.org/10.4131/jshpreview.20.269

Shibazaki, Y., Ohtani, E., Fukui, H., Sakai, T., Kamada, S., Ishikawa, D., Tsutsui, S., Baron, A.Q.R., Nishitani, N., Hirao, N., Takemura, K., 2012. Sound velocity measurements in dhcp-FeH up to 70 GPa with inelastic X-ray scattering: Implications for the composition of the Earth's core. Earth Planet. Sci. Lett. 313–314, 79–85.

https://doi.org/10.1016/j.epsl.2011.11.002

Sturhahn, W., 2000. CONUSS and PHOENIX: Evaluation of nuclear resonant scattering data. Hyperfine Interact. 125, 149–172. https://doi.org/10.1023/A:1012681503686

Tagawa, S., Ohta, K., Hirose, K., Kato, C., Ohishi, Y., 2016. Compression of Fe-Si-H alloys to core pressures. Geophys. Res. Lett. 43, 3686–3692. https://doi.org/10.1002/2016GL068848

Tateno, S., Kuwayama, Y., Hirose, K., Ohishi, Y., 2015. The structure of Fe–Si alloy in Earth's inner core. Earth Planet. Sci. Lett. 418, 11–19. https://doi.org/10.1016/j.epsl.2015.02.008

Thompson, E.C., Davis, A.H., Bi, W., Zhao, J., Alp, E.E., Zhang, D., Greenberg, E., Prakapenka, V.B., Campbell, A.J., 2018. High-Pressure Geophysical Properties of *Fcc* Phase FeH*x*. Geochemistry, Geophys. Geosystems 19, 305–314. https://doi.org/10.1002/2017GC007168

Vinet, P., Ferrante, J., Rose, J.H., Smith, J.R., 1987. Compressibility of solids. J. Geophys. Res. 92, 9319. https://doi.org/10.1029/jb092ib09p09319

Yoda, Y., Zhang, X., Kikuta, S., 2007. High-Resolution Monochromators for Nuclear Resonant Scattering Developed at BL09XU, SPring-8, in: AIP Conference Proceedings. AIP, pp. 926–929. https://doi.org/10.1063/1.2436213

Acknowledgments on this chapter

I would like to thank Dr. Yoichi Nakajima for his help through the present NIS experiments and data analysis. I also thank Dr. Takahiro Matsuoka for hydrogen loading, Dr. Takaya Mitsui and Dr. Yoshitaka Yoda for their help in NIS measurements, and Dr. Naohisa Hirao for the XRD measurements. The NIS measurements were performed at SPring-8 (proposal no. 2016B1460, 2017A1394).